National Laser Users' Facility and External Users' Programs

Under the facility governance plan implemented in FY08 to formalize the scheduling of the Omega Laser Facility as an NNSA User Facility, Omega Facility shots are allocated by campaign. The majority (65%) of the FY10 target shots were allocated to the National Ignition Campaign (NIC) conducted by integrated teams from the national laboratories and LLE and to the high-energy-density campaigns conducted by teams led by scientists from the national laboratories.

In FY10, 30% of the facility shots were allocated to basic science experiments. Half of these were dedicated to university basic science under the National Laser Users' Facility (NLUF) Program, and the remaining shots were allotted to the Laboratory Basic Science (LBS) Program, comprising peer-reviewed basic science experiments conducted by the national laboratories and LLE/FSC.

The Omega Facility is also being used for several campaigns by teams from the Commissariat à l'énergie atomique (CEA) of France and the Atomic Weapons Establishment (AWE) of the United Kingdom. These programs are conducted on the facility on the basis of special agreements put in place by the DOE/NNSA and the participating institutions.

The facility users during this year included 11 collaborative teams participating in the NLUF Program; 12 teams led by LLNL and LLE scientists participating in the LBS Program; many collaborative teams from the national laboratories conducting experiments for the NIC; investigators from LLNL and LANL conducting experiments for high-energy-density physics programs; and scientists and engineers from CEA and AWE.

In this section, we briefly review all the external user activity on OMEGA during FY10.

FY10 NLUF Program

In FY10, DOE issued a solicitation for NLUF grants for the period of FY11–FY12. A total of 15 proposals were submitted to DOE for the NLUF FY11–12 program. An independent DOE Technical Evaluation Panel comprised of Dr. Damien Hicks (LLNL), Prof. John K. McIver (University of Idaho), Dr. Gregory Rochau (SNL), Prof. Sharon Stephenson (Gettysburg College), Dr. Alan Wooton (University of Texas), Dr. Jonathan Workman (LANL), and Dr. John Soures (Committee Chair, non-voting) reviewed the proposals on 18 August 2010 and recommended that 11 proposals receive DOE funding and 31 days of shot time on OMEGA in each of FY11 and FY12. Table 124.V lists the successful NLUF proposals.

FY10 was the second of a two-year period of performance for the NLUF projects approved for the FY09–FY10 funding and OMEGA shots. Eleven NLUF projects were allotted Omega Facility shot time and conducted a total of 197 target shots on the facility. This work is summarized in this section.

Systematic Study of Fast-Electron Generation and Transport

Principal Investigator: F. N. Beg (University of California, San Diego)

Co-investigators: T. Yabuuchi, H. Sawada, and M. S. Wei (University of California, San Diego); R. B Stephens (General Atomics); S. P. Regan, K. Anderson, C. Stoeckl, W. Theobald, and R. Betti (LLE); and P. K. Patel, A. J. Mackinnon, H. S. McLean, S. C. Wilks, and M. H. Key (LLNL)

Understanding fast-electron generation and transport in the cone tip and warm dense plasma is very important for the success of the cone-guided fast ignition. We have performed two experiments in FY10 on OMEGA EP regarding this important topic. The goal of the first experiment was to characterize a plasma to be used as the transport medium in the second experiment, using the x-ray line absorption spectroscopy. The goal of the second experiment was to study the fast-electron transport in the characterized plasma. In both experiments, the warm dense plasma was created by using a shock to heat a foam target. The foam target package consisted of 200-mg/cm^3 CH foam doped with aluminum inside a solid plastic container. The shock was created by irradiating a plastic foil in front of the foam with a long-pulse laser (1.2 kJ/3.5 ns in UV) as shown

in Fig. 124.78. A two-dimensional *DRACO* simulation shows that the foam plasma had a peak temperature (density) of 30 to 50 eV (110 to 180 mg/cc) at about 7 to 8 ns.

A laser-irradiated samarium dot target was used as the x-ray point source for the absorption spectroscopy. The x rays (1.4 to 1.6 keV) with a smooth, broad spectrum penetrated the foam

Table 124.V: Approved FY11 and FY12 NLUF proposals.

| Principal Investigator	Affiliation	Project Title
F. Beg	University of California, San Diego	Systematic Study of Fast-Electron Transport in Imploded Plasmas
R. P. Drake	University of Michigan	Experimental Astrophysics on the OMEGA Laser
T. Duffy	Princeton University	Ramp Compression for Studying Equations of State, Phase Transitions, and Kinetics on OMEGA
R. Falcone	University of California, Berkeley	Detailed *In-Situ* Diagnostics of High-Z Shocks
P. Hartigan	Rice University	Clumpy Environments and Interacting Shock Waves: Realistic Laboratory Analogs of Astrophysical Flows
R. Jeanloz	University of California, Berkeley	Recreating Planetary Core Conditions on OMEGA
K. Krushelnick	University of Michigan	Intense Laser Interactions with Low-Density Plasma Using OMEGA EP
R. Mancini	University of Nevada, Reno	Investigation of Hydrodynamic Stability and Shock Dynamics in OMEGA Direct-Drive Implosions Using Spectrally Resolved Imaging
R. D. Petrasso	Massachusetts Institute of Technology	Charged-Particle Probing of Inertial Confinement Fusion Implosions and High-Energy-Density Plasmas
A. Spitkovsky	Princeton University	Collisionless Shocks Laboratory High-Energy-Density Plasmas
R. Stephens	General Atomics	Investigation of Laser-to-Electron Energy Coupling Dependence on Laser-Pulse Duration and Material Composition
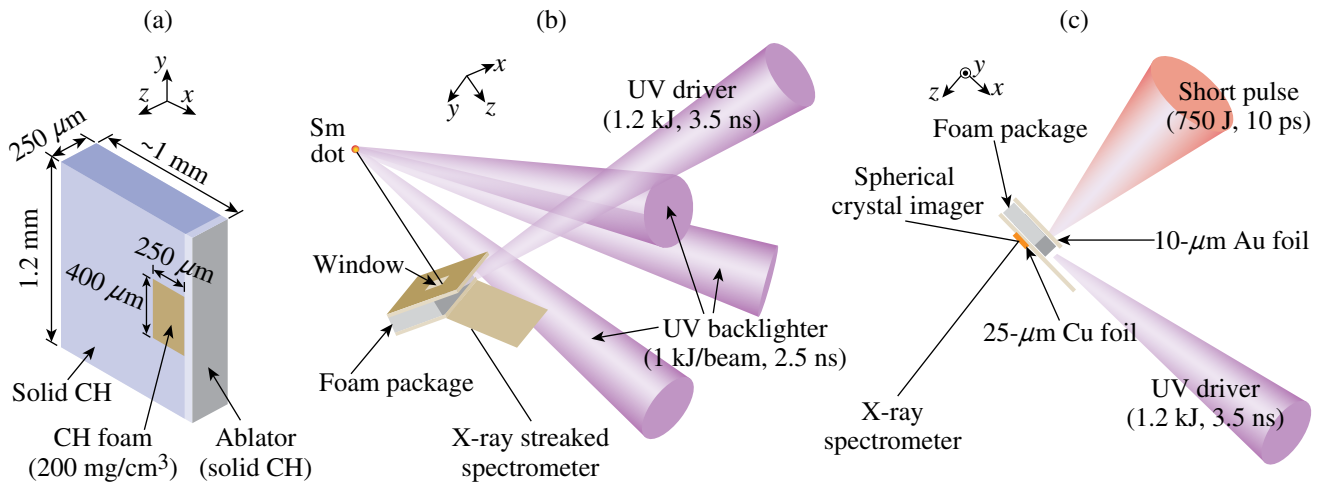
Figure 124.78
(a) Schematic of the foam package target. Au foils coated with plastic on both sides were used for both experiments as seen in the experimental setup for (b) plasma characterization and (c) fast-electron transport. The foils on the target-side faces had a hole to transmit backlighter x rays for the characterization experiments. The holes were covered with Au and Cu foils in the transport experiment.

plasma through small windows on the target walls and were absorbed by aluminum atoms doped in the foam target. The line-absorption features in the spectra depend on the density and the temperature of the plasma. Figure 124.79 shows a temporal evolution of the absorbed spectra recorded with an x-ray streaked spectrometer. Preliminary analysis of the temperature of the foam using an atomic physics code *FLYCHK* indicates that the plasma temperature was about 30 eV at 7 ns after the start of the long-pulse–laser irradiation. The presence of the lower-charge-state (i.e., O-like and F-like) features later in time indicates a clear trend of the plasma cooling in time.
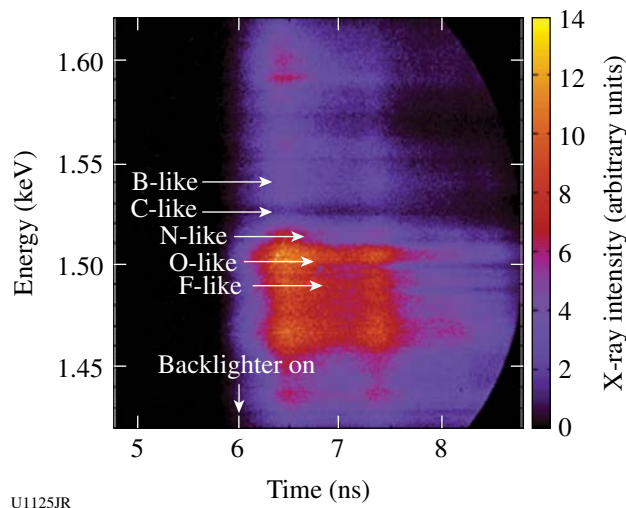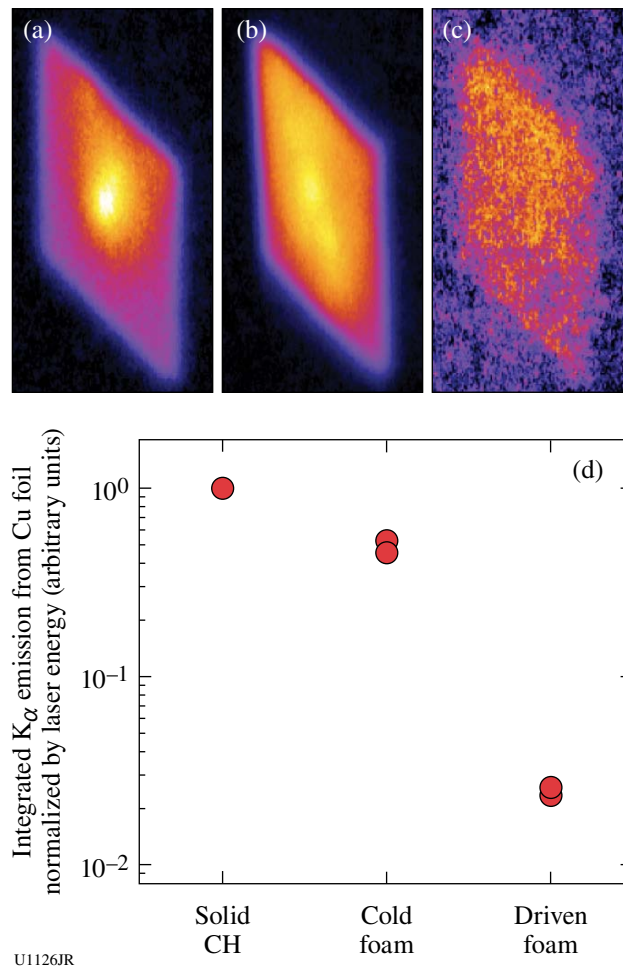

Figure 124.79
Streaked x-ray spectrum observed with Al-doped CH foam target driven by a 1.2-kJ, 3.5-ns UV long-pulse laser. Several Al absorption lines can be seen as indicated by arrows.

An OMEGA EP short-pulse laser irradiated the driven foam target at 7 ns in the transport study. The windows on the sides of the package targets were covered with Au (10-μm) and Cu (25-μm) foils. The Au foil served as the laser–plasma interaction layer, and the Cu foil served as a fluorescence layer of K_α x rays emitted by the binary collisions of fast electrons and the Cu atoms. The K_α x rays were monitored with an x-ray spectrometer and a newly developed spherical crystal imager. The transport medium was varied from the laser-driven foam plasma to undriven foam and a solid plastic, which had the same areal density as the undriven foam. As shown in Fig 124.80, a small spot of K_α x rays was observed with cold targets; however, no clear structure was found in the case where the foam plasma was the transport medium, which indicates a large divergence of the electron beam. In addition, a reduction of the K_α x-ray yield by a factor of 20 was measured when the target was driven. The physical mechanisms contributing to a large divergence angle

and low transport efficiency with the driven-foam target will be studied with hybrid particle-in-cell (PIC) codes.

Figure 124.80
Cu K_α images observed with a spherical crystal imager when the transport medium was (a) 50 μm of solid CH, (b) 250 μm of cold foam, and (c) 360 μm of driven foam. (d) Integrated K_α x-ray yield measured with the x-ray spectrometer for three cases.

Experimental Astrophysics on the OMEGA Laser

Principal Investigator: R. P. Drake (University of Michigan)
Co-investigators: D. Arnett (University of Arizona); T. Plewa (Florida State University); J. Glimm, D. Swesty, X. Li, and A. Calder (State University of New York–Stony Brook); I. Sokolov, J. Holloway, K. Powell, and C. Kuranz (University of Michigan); J. P. Knauer and T. R. Boehly (LLE); and B. Remington, H. Robey, F. Hansen, A. Miles, S. Glenzer, and H.-S. Park (LLNL)

The OMEGA laser can create systems with very high energy densities that are relevant to astrophysical phenomena.

This is possible because OMEGA can deposit large amounts of energy into areas measuring square millimeters, generating pressures of greater than 10 Mbars (~10-million atmospheres). In some astrophysical systems, radiation can play a dominant role in the hydrodynamic behavior of the system. This occurs, for example, in radiative shocks in which the shocked matter is so hot that it radiates away most of its energy. This project has explored two types of radiative shocks—a driven radiative shock and a radiative reverse shock. These types of shocks can be found in supernova remnants, where a fast-moving shock encounters a low-density gas, and cataclysmic variables, where a supersonic plasma flow is impeded by a dense accretion disk.

In March 2010, a campaign was continued using the OMEGA laser to create a driven radiative shock in a xenon-filled shock tube. Ten OMEGA laser beams irradiated a Be disk for 1 ns. The beams deposited a total energy of ~3.8 kJ, giving an average irradiance of ~7×10^{14} W/cm^2 and generating an ablation pressure of ~46 Mbars in the disk. The Be acts as a piston to drive a shock in 1.1 atm of Xe with speeds in excess of 100 km/s. This velocity exceeds the threshold where radiative effects play an important role in the dynamics of the experiment. The cooling by escaping radiation creates a collapsed dense layer of xenon, which is preceded in the tube by a radiation-heated precursor region and followed by a downstream layer of expanding Be.

The most-recent efforts to diagnose a driven radiative shock employed the streaked x-ray radiography and x-ray Thomson scattering (XRTS) diagnostic techniques simultaneously to differentiate measurements from the different regions of the shock system. For each region, x-ray Thomson scattering may provide information on electron temperature and ionization state, while streaked radiography yields shock velocity and acceleration. Example streak camera and XRTS data are shown in Figs. 124.81 and 124.82. Figure 124.81 shows a streaked x-ray radiograph indicating the distance of the shocked layer from the drive disk versus time. The fiducial wire is seen in the lower part of the image, and the sloped line moving from the left to the upper right indicates the motion of the shocked Xe layer. Figure 124.82 is a plot of intensity versus energy obtained using the XRTS technique. For this experiment, a Zn source with He$_\alpha$ emission near 9 keV was used to probe the dense, shocked Xe layer. The incident signal is represented by the black curve, and scattered light from free and loosely bound electrons is represented by the blue curve.

A second type of radiative shock that this project has explored is a radiative reverse shock. The first experimental

attempt at creating this type of shock took place in August 2010. In this experiment, ten OMEGA laser beams irradiated a plastic-coated tin disk for 1 ns. The beams deposited a total
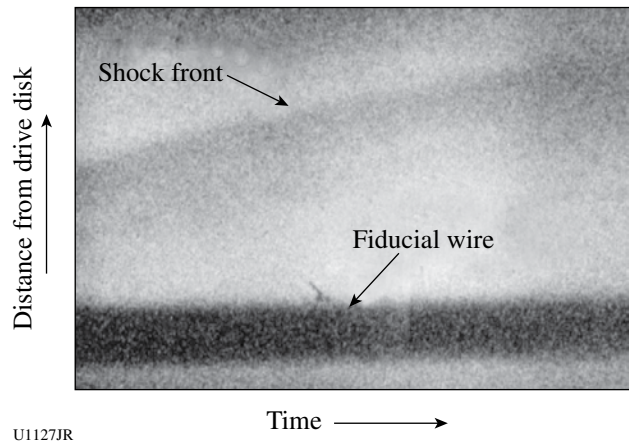

U1127JR

Figure 124.81
A streaked x-ray radiograph of a dense Xe layer, which provides a measure of shock velocity and acceleration. The shock is moving to the upper right in this image. An opaque wire was used to calibrate the spatial scale and determine the position of the shock at the time of imaging, while streak camera timing fiducials (not shown) calibrate the temporal scale.
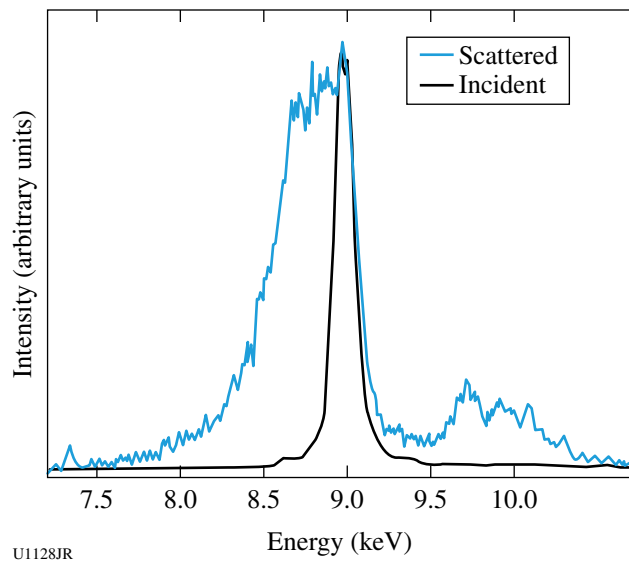

U1128JR

Figure 124.82
Incident and scattered spectra frmo March 2010 OMEGA experiments. A zinc source with He$_\alpha$ emission near 9 keV is used to interrogate the dense, shock-compressed Xe layer (black curve). Inelastic collisions with free and loosely bound electrons red-shift the input signal, generating the Compton feature seen below 9 keV (blue curve, normalized to match input curve's peak intensity).

energy of ~4.5 kJ, giving an average irradiance of ~10^{15} W/cm^2. This creates a fast (greater than ~100 km/s) tin plasma flow through a millimeter-scale shock tube that is at vacuum. This supersonic plasma flow was impeded by a 100-μm Al "wall," which would create a reverse shock. This shock was imaged using x-ray radiography, and self-emission from the radiative shock was recorded using a streaked optical pyrometer (SOP).

Figure 124.83 is an x-ray radiograph of a radiative reverse shock. The Al wall is labeled in the image, and the Sn plasma flow originates about 4 mm from the wall from the lower-left direction. Figure 124.84 shows data from the SOP, which captured about 100 ns of data. The directions of space and time are labeled on the image and the approximate location of the Al wall is also labeled. When the supersonic plasma flow collides with the Al, a reverse shock forms, but a strong transmitted shock is created in the Al; both are indicated in Fig. 124.84.
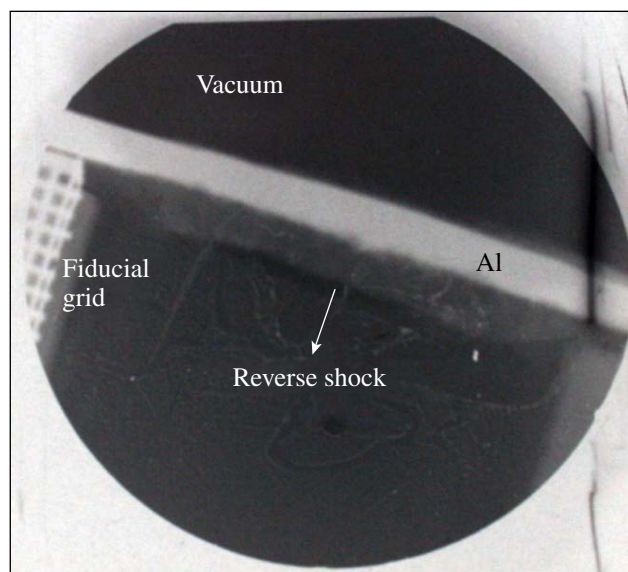

U1129JR

Figure 124.83
An x-ray radiograph of a radiative reverse shock. The Al wall is labeled in the image, and the Sn plasma flow originates about 4 mm from the wall from the lower left direction. The radiative reverse shock is moving away from the wall to the lower left.

This experiment was modeled using the *CRASH* code. The *CRASH* code is a multidimensional physics code that has been developed at the University of Michigan's Center for Radiative Shock Hydrodynamics. The density plots shown in Fig. 124.85 are simulation results from the *CRASH* code, and the laser-energy deposition was modeled using the

2-D *HYADES* code and then used to initialize the *CRASH* simulation. Figure 124.85 shows the direction of the incoming plasma flow (to the right); the Al wall is the dense obstacle in this case. The radiative reverse shock is a thin, dense layer that is moving to the left of the Al.
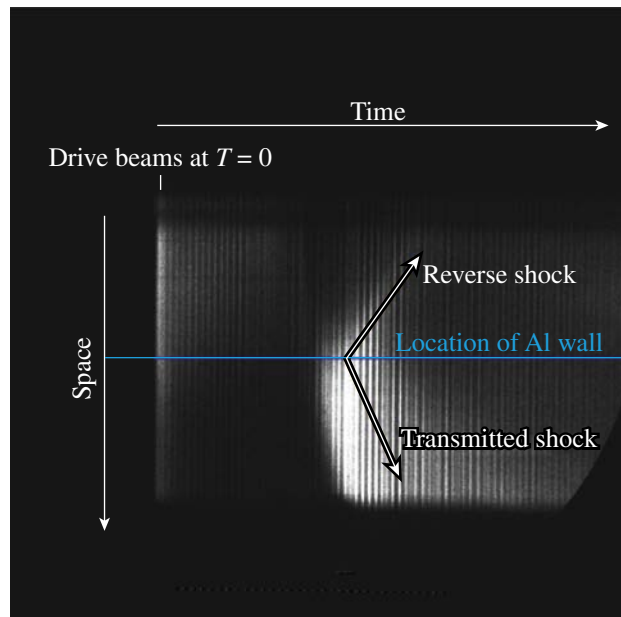
U1130JR

Figure 124.84
Thermal emission data over 100 ns from a streaked optical pyrometer of a radiative reverse shock. The approximate temporal location of the initial laser pulse is labeled as well as the approximate spatial location of the Al wall. Emission from reverse shock shows the shock moving away from the Al wall.
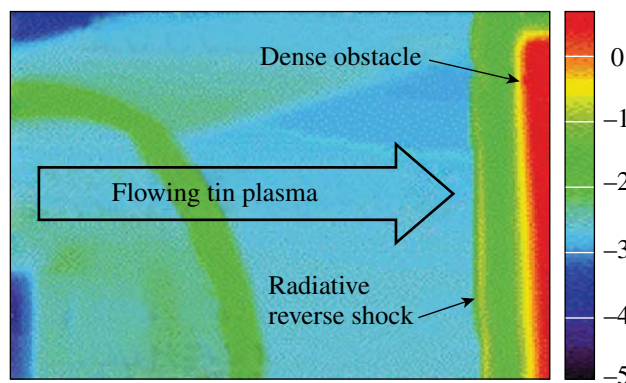
U1131JR

Figure 124.85
Results from a *CRASH* simulation of a radiative reverse shock system. The Sn plasma flow is moving to the right and collides with the dense Al. This creates a thin, dense radiative reverse shock moving to the left.

Detailed In-Situ *Diagnostics of Multiple Shocks*

Principal Investigator: R. W. Falcone (University of California, Berkeley)

Co-investigators: T. Ma, T. Doeppner, O. L. Landen, and S. H. Glenzer (LLNL); and H. J. Lee (SLAC Stanford Linear Accelerator Laboratory)

X-ray Thomson scattering was used to directly provide the temperature and density of shock-compressed matter.[1] Accurate characterization of dense states of matter is vital for understanding high-energy-density experiments, as well as the validation of equation of state (EOS) and plasma model assumptions. In this experiment, 250-μm Al and Be foils were shock compressed in a counter-propagating geometry using 12 drive beams with a total energy of 6 kJ at 351 nm in a 3-ns pulse. SG4 distributed phase plates were used to achieve a smooth 800-μm focal spot, yielding a total drive intensity of $\sim 2 \times 10^{14}$ W/cm^2 on each side of the foil sample.

The shocked samples were probed at 140° scattering angles and varying delay times by Zn K$_\alpha$ x rays, at 8.6 keV (in the case of the Be foil), or Mo He$_\alpha$ x rays at 18.9 keV (in the case of the shocked Al foil). For both samples, the noncollective scattering regime was accessed, where $\alpha = 0.3$, $k = 8.2$ Å^{-1}, and $\alpha = 0.1$, $k = 17.1$ Å^{-1} for the Be and the Al, respectively. The prominent Compton feature with elastic peak responding to Mo He$_\alpha$ in Fig. 124.86(b) demonstrates the feasibility as a backlighter for probing Al, the highest-Z material probed to date. The increase in the strength of the Compton feature with time as seen in Fig. 124.86(c) shows that the electron density changes with shock propagation.[2] The Compton feature at each time of 2.37 ns, 2.85 ns, and 3.83 ns presents the response of compressed state before, during, and
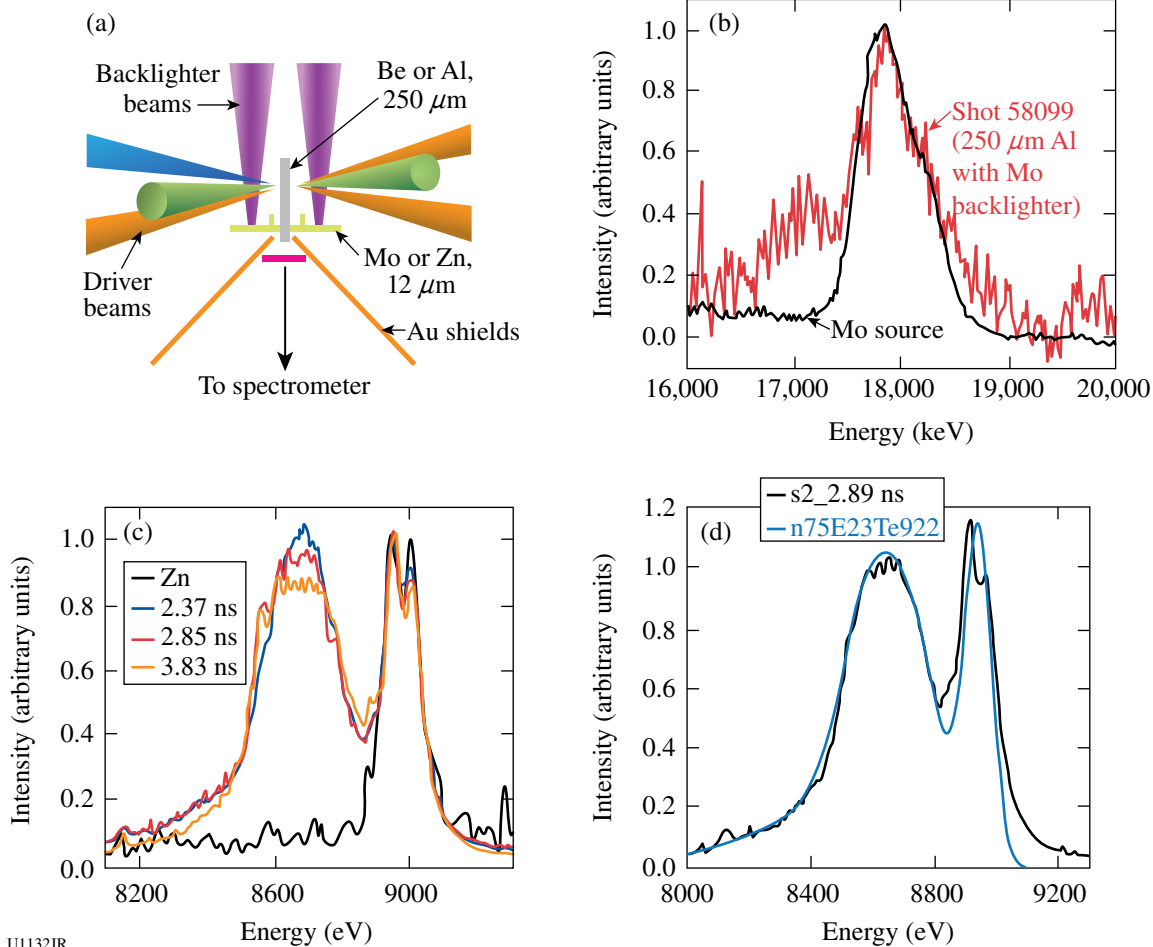

U1132JR

Figure 124.86
(a) Experimental configuration; (b) Mo He$_\alpha$ backlighter and scattering spectrum in compressed Al; (c) Zn K$_\alpha$ backlighter and scattering spectrum on shock-compressed Be at 2.37, 2.85, and 3.83 ns; and (d) scattering data for compressed Be and fit at 2.89 ns.

after the collision of counter-propagating shocks. A theoretical fit to the spectra at 2.89 ns in Fig. 124.86(d) allows one to infer the temperature, electron density, and ionization state. Analysis is ongoing to develop a more complete picture of the density and temperature of shock-compressed matter by counter-propagating shocks, which will address the radiation–hydrodynamic models.

OMEGA EP–Generated X-Ray Source for High-Resolution 100- to 200-keV Point-Projection Radiography
Principle Investigator: U. Feldman (Artep Inc.)

The first-year goal of this project was to design and construct a ten-inch manipulator (TIM)–compatible OMEGA EP transmission crystal spectrometer (TCS) capable of measuring the size of the target region from which energetic (20- to 100-keV) photons produced by fast electrons are being emitted. The recording media, which could be located at distances of 20, 40, and 60 in. from target center, were designed to be image plates. During the first part of 2009, the TCS was designed and constructed (Fig. 124.87), and on 26–27 August it recorded spectra from a number of OMEGA EP shots. The recorded spectral lines indicated that, although the OMEGA EP beams were tightly focused (30 to 40 μm), the diameter of the area from which the hard x rays were emitted (a measure of the spread of the hot electrons) was 350 to 400 μm.

Our goal for the second year was to replace the image plate at the 60-in. location, which has pixel sizes of 100 μm or larger, with an electronic detector with pixel sizes of the order of ~25 μm. In early July 2010, the TCS was delivered to LLE, where it was mechanically and electronically checked by the LLE technical staff and Artep team members. On 15 September, the TCS was installed in the OMEGA EP chamber and recorded spectra from several specially designed targets.

The September experiments provided high-quality x-ray spectra on the TCS image-plate (IP) channels. Sample spectra from IP positions A [on the Rowland circle (RC)—focusing] and B (500 mm off the RC—source size broadened) are shown on Fig. 124.88. With careful analysis, the x-ray source size can be determined from the source-size–broadened spectrum (IP B).
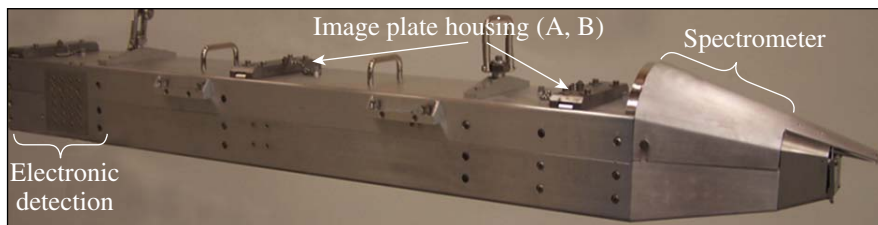
Validating Inelastic X-Ray Scattering from H and H/He Warm Dense Matter with Shock-Velocity Measurements: Toward the Equation of State of Jupiter's Core
Principal Investigator: S. P. Regan (LLE)
Co-investigators: T. R. Boehly and P. B. Radha (LLE); and G. Gregori (Oxford)

The objective of this experiment is to measure the equation of state (P, ρ, n_e, T_e, Z) of direct-drive, shock-heated and compressed, planar cryogenic H and H/He mixtures using spectrally resolved x-ray scattering (i.e., inelastic x-ray scattering) and shock-velocity measurements on the OMEGA Laser System. The dynamics at the shock front and the plasma conditions in the bulk of the shocked material will be probed simultaneously with complementary diagnostics: the electron density (n_e) will be inferred from collective inelastic x-ray scattering (i.e., scattering from electron-plasma waves or plasmons);[3] the electron temperature (T_e) and average ionization (Z) will be inferred from the noncollective x-ray scattering (i.e., scattering from individual electrons);[1,4] and the pressure (P) and mass density (ρ) will be inferred from the velocity interferometer system for any reflector (VISAR) diagnostic.[5] Equation-of-state (EOS) measurements typically diagnose the shock velocity (U_s) using the VISAR diagnostic and infer the particle velocity (U_p) by an impedance-matching analysis.[6] The quantities U_s and U_p are related to P and ρ through the Rankine–Hugoniot relations.[7–9] The ablation pressure inferred from the VISAR observation is critical for the EOS measurement. On the first LBS project shot day in FY10, the U_s in liquid D_2 irradiated for 6 ns with an intensity around 10^{13} W/cm^2 was measured with VISAR. The result is shown in Fig. 124.89 with the laser irradiation starting at $t = 0$ ns. Ionization of the CH ablator blocks the VISAR laser signal from the reflective, advancing shock front for the first 1.5 ns. The shock velocity in the time interval between 4 and 6 ns, when x-ray scattering measurements are typically performed, is 18 μm/ns. Using the U_s–U_p relation for shocked D_2 reported by Hicks *et al.*,[6] a pressure of 0.4 Mbar and four-fold compression were inferred. Figure 124.90 presents measurements of the noncollective inelastic x-ray scattering from a liquid-deuterium target irradiated with a similar laser drive on the second

Image plate housing (A, B)
Spectrometer
Electronic detection
U1133JR

Figure 124.87
The transmission crystal spectrometer (TCS) with an electronic detector.

shot day of the experiment. Analysis is in progress to infer the shocked conditions from the VISAR and inelastic x-ray scattering measurements. The warm dense matter created in these experiments with laser-ablation–driven shock waves had plasma conditions comparable to those predicted in planetary interiors (i.e., dense, Fermi-degenerate matter). While Jupiter is mostly made of hydrogen, with only a fraction of He (<25%) and a few metals,[10–16] the concentrations of other giant planets in the solar system are significantly enriched with C, O, and N. These form the so-called "ices" that are typical of the giant planets, such as Uranus and Neptune, and possibly extrasolar planets, such as GJ436b.[17–19]

Development of a Platform for Laser-Ramp Compression of Planetary Materials on OMEGA

Principal Investigators: Y. M. Gupta (Washington State University) and T. S. Duffy (Princeton University)
Co-investigators: J. Montoya, J. Wang, and G. Finkelstein (Princeton University); R. F. Smith, J. H. Eggert, P. M. Celliers, D. Braun, and M. Bastea (LLNL); and T. R. Boehly (LLE)

This experiment was allocated 1.5 shot days on OMEGA in FY10 to develop a high-pressure, low-temperature ramp-compression drive, which permits one to explore new regions of thermodynamic space of particular relevance to material
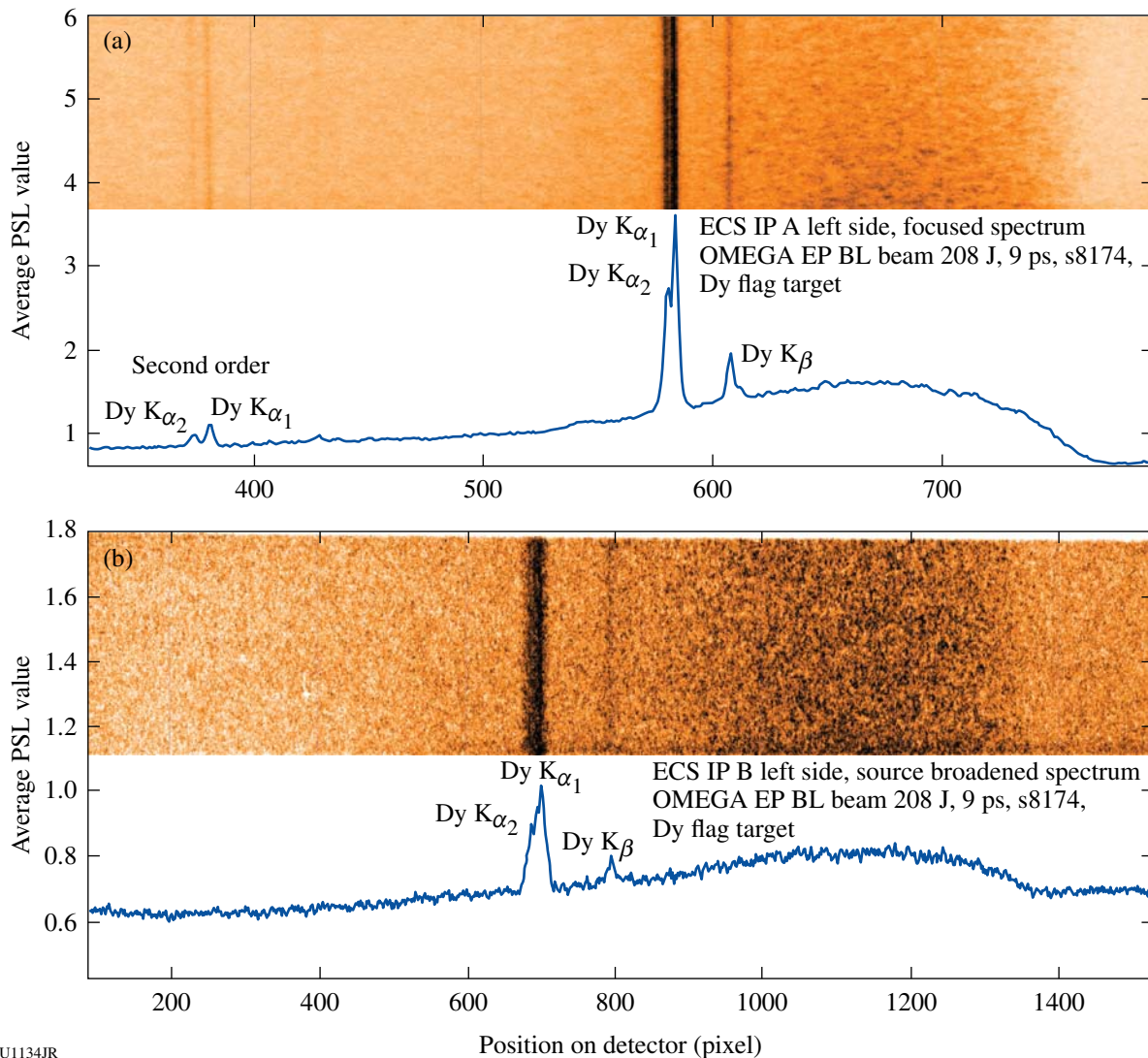

U1134JR

Figure 124.88
Sample spectra of the TCS taken on OMEGA EP from campaign PPRad-EP-10. Spectral images and column averages showing characteristic Dy K lines ($K_{\alpha 1}$: 45.99 keV). (a) Lines in first and second order on IP A on the focusing Rowland circle and (b) IP B providing source size broadening of the spectral lines at a 500-mm distance from the focusing Rowland circle position.
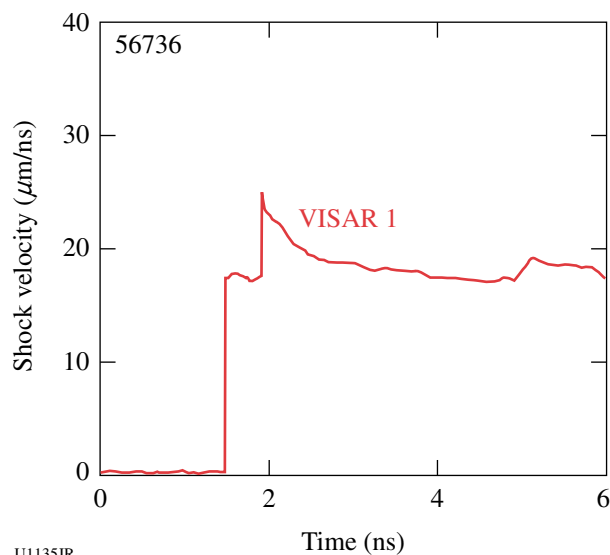
Figure 124.89

Shock-velocity measurement taken on OMEGA shot 56736 with VISAR of a liquid-D_2 target irradiated for 6 ns with an intensity around 10^{13} W/cm^2 starting at $t = 0$ ns. Ionization of the CH ablator interrupts the VISAR laser signal for the first 1.5 ns. The average shock velocity in the time interval when x-ray scattering measurements are performed (4 ns $< t <$ 6 ns) is 18 μm/ns.
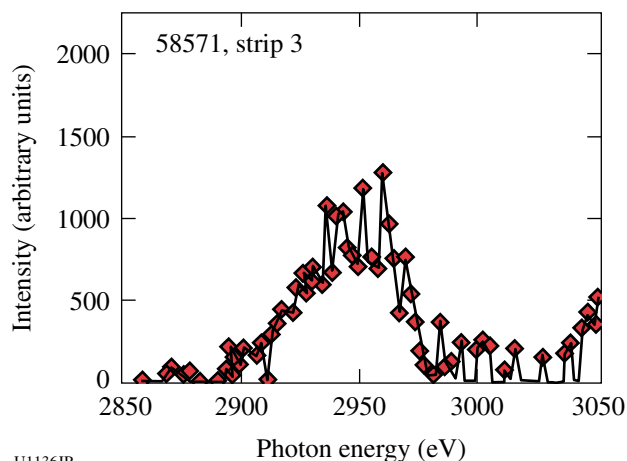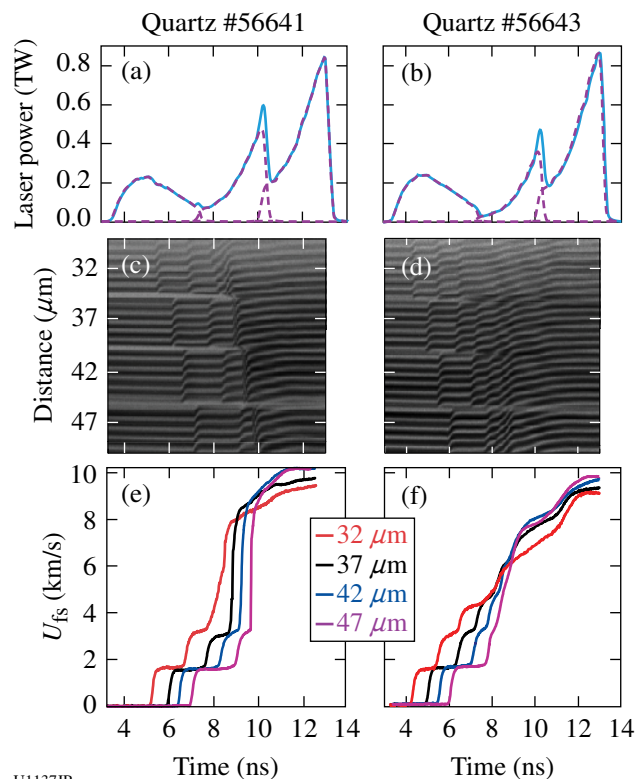

Figure 124.90

Inelastic x-ray scattering measurement taken on OMEGA shot 58571 of a liquid-D_2 target irradiated for 6 ns with an intensity around 10^{13} W/cm^2 starting at $t = 0$ ns. Observation was recorded at $t = 6$ ns. Analysis to infer shocked conditions in liquid D_2 is in progress.

conditions found in planetary interiors. Ramp compression achieves high compression at relatively modest temperatures and can be used to extract quasi-isentropic equation-of-state data, study solid–solid phase transitions, and compress materials in the solid state to higher pressures than can be achieved with diamond-anvil-cell (DAC) or shock-wave methods. An experimental platform for ramp loading of quartz (SiO$_2$) and

iron (Fe) has been established and tested in experiments at the Omega Laser Facility. Target packages consist of stepped samples and a diamond ablator attached to a Au halfraum. Composite laser pulses are used to drive a ramp-compression wave into the sample. The target and laser-ramp designs have been tested and optimized by combining experiments with computer simulations using a hydrodynamics code. A spatially planar ($\Delta t/t = 0.9\%$) ramp wave drive has been achieved in both SiO$_2$ and Fe stepped samples to peak stress around 250 GPa and 400 GPa, respectively, over nanosecond time scales.

Figure 124.91 shows the input laser profile, VISAR streak camera records, and corresponding free-surface velocity histories for two typical quartz experiments. The extracted free-surface velocity histories in Figs. 124.91(e,f) show a very structured breakout with a series of ramped "plateaus" consistent with drops in the bulk sound speed caused by the onset of

Figure 124.91

(a) and (b) Laser pulse for two representative quartz shots (56641 and 56643). The dashed lines show the individual pulses and the solid line is the composition pulse shape. (c) and (d) Line VISAR streak camera images (1.971 km/s per fringe) from ramp-compressed multi-stepped quartz targets (56641 and 56643) corresponding to (a) and (b), respectively. In (c) and (d), different step thicknesses are indicated. (e) and (f) Extracted free-surface velocity profiles from (c) and (d), respectively.

elastic-plastic deformation or a polymorphic phase transformation. The input laser profile was designed to generate an initial steady shock in quartz followed by subsequent ramp compression. An unusual feature of these profiles is the convergence of wave-arrival times for multiple steps in the 7- to 9-ns range (Fig. 124.91). It is believed that this feature is an artifact of the complicated wave interactions between free-surface reflections that combined with the onset of a phase transformation. In future experiments, the use of a lithium fluoride (LiF) window may suppress the effects of interactions. Figure 124.92 shows a sequence of measured pulses and the corresponding wave profiles for the first target step in Fe samples for several differ-

ent shots. By changing the time delay between the two pulses, it was possible to decrease the amplitude of the second shock and achieve a more ramp-like compression. However, it was not possible to completely eliminate the second shock (shots 58591 to 58593). Keeping the same delay, but increasing the power in the second pulse strongly increased the amplitude of the second shock (shot 58594). Figure 124.93 shows preliminary pressure-density curves for Fe and SiO_2 calculated with standard Lagrangian sound speed analysis. The complexity of the wave interactions caused some discrepancies among different shots. Further work will focus on the development of new analytical tools to analyze ramp-compression data for
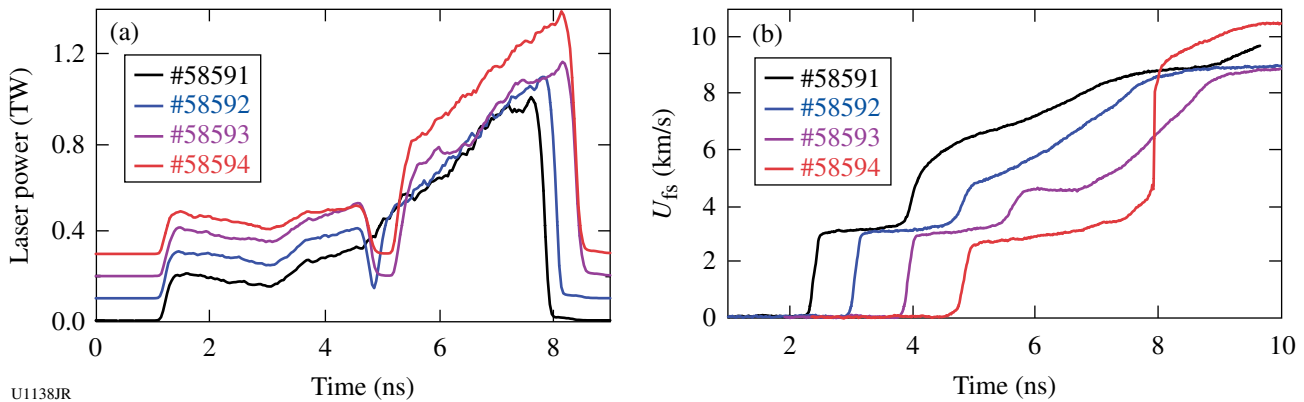

Figure 124.92

(a) Composite laser pulse shapes from a series of shots on Fe targets along with free-surface velocity profiles for the first step corresponding to each laser drive. (b) Shots 58591 to 58593 correspond to delays between the pulses of 3.5 ns, 3.65 ns, and 3.88 ns. For shot 58594, the delay was maintained the same (3.88 ns), but the power was increased. In (a), the traces are offset in amplitude (by 0.1 TW) for clarity, and the traces are offset temporally in (b).
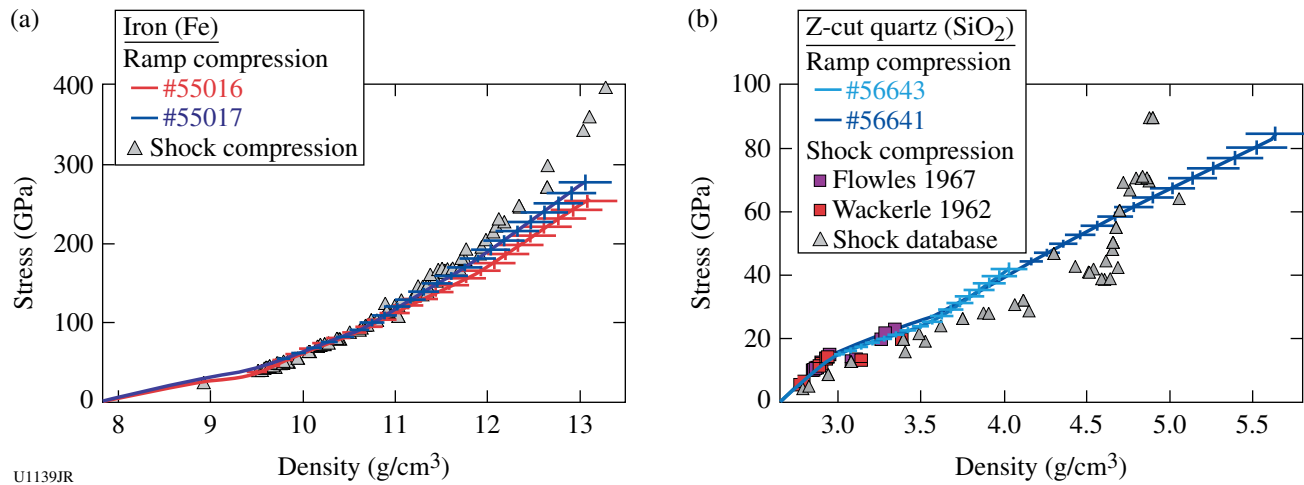

Figure 124.93

Preliminary pressure-density curves for Fe and SiO_2 calculated with standard iterative–characteristic Lagrangian sound speed analysis developed by Rothman. (a) Data are shown for two separate shots taken during an NLUF shot day on 23 July 2009. Also shown are previous data taken from shock experiments. (b) Data are shown for two different shots taken during an NLUF shot day on 20 January 2010, and shock data are shown from previous studies.

materials undergoing time-dependent compression, including treating the initial shock and phase transformation.

Laboratory Experiments of Supersonic Astrophysical Flows Interacting with Clumpy Environments

Principal Investigator: P. Hartigan (Rice University)
Co-investigators: J. Palmer (Rice University); J. Foster and P. Rosen (AWE); B. Wilde and M. Douglas (LANL); A. Frank (University of Rochester); and B. E. Blue and F. Hansen (General Atomics)

A primary goal of the NLUF program is to study how strong shock waves propagate through clumpy media such as those encountered by astrophysical jets as they interact with their nascent molecular clouds. In the current program, an experimental design was developed that allows one to observe a strong shock as it sweeps past a collection of obstacles in its path. The laboratory work complements new astrophysical images from the Hubble Space Telescope (HST) that were taken as part of a previous NLUF program.

Samples of some of the shots and numerical simulations of the experiments from the last year appear in Fig. 124.94. The target consists of cylindrical foam into which are embedded anywhere from a few to several dozen sapphire spheres. A database is being accumulated that will answer the question of how the packing fraction and clump size within the obstacle affect the propagation speed and coherence of the strong shock wave that is driven through the foam. Numerical support is provided by the *RAGE* code (see Fig. 124.94). The experiments provide important tests of the code in a complex regime that is inherently 3-D and includes multiple shocks and mixing of post-shock material. The experiments reveal dynamical changes that occur when one sphere lies in the wake of another, and they expand on previous work with two spheres, where it was learned how a planar shock creates vorticity as it interacts with the spheres.

This ongoing NLUF work is producing a series of publications in the primary refereed journals of the field, and numerous contributed and invited talks have been given at recent conferences. In 2009, this OMEGA collaboration published a large paper in the Astrophysical Journal,[20] and another paper was just accepted into Physics of Plasmas related to Mach stem work.[21] This latter paper is now motivating a new line of research that the group plans to pursue in the next two years. Another large Astrophysical Journal paper nearing completion concerns motions within shocked jets; a paper on the vorticity between two shocked spheres is in preparation; and our current set of shot data will produce a thorough study of shocked
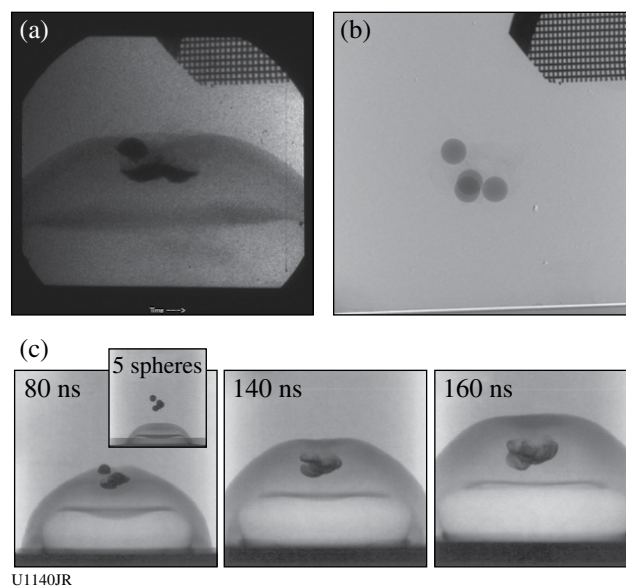

Figure 124.94
(a) Shot data (taken at 100 ns) and (b) pre-shot radiograph of a target containing four spheres. The shock wave moves upward and has just overtaken the spheres, flattening and distorting them. (c) Time-sequence numerical simulation (from *RAGE*) of a target with five spheres. A filamentary structure develops as bow shocks around each sphere interact and shadow one another. This filamentary structure resembles features we observe in the working surfaces of astrophysical jets.

clump phenomena. Student participation includes two recent Ph.D.'s (one of whom will be taking up a position at a national lab) and an M.S. thesis in its final stage.

Measurements of the Equation of State of H_2/He Mixtures Under Deep Planetary Conditions

Principal Investigator: R. Jeanloz (University of California, Berkeley)
Co-investigators: P. Loubeyre (CEA); J. H. Eggert, D. G. Hicks, P. Celliers, and G. W. Collins (LLNL); and T. R. Boehly (LLE)

Using the Omega Laser Facility, this project is demonstrating that laboratory experiments can provide crucial data to model the interior structure of the planets. Specifically, measuring the equation of state of planetary constituents is complementary to space missions for understanding the interiors and evolution of giant fluid planets. The immediate goal of these experiments is to measure the equation of state of hydrogen and helium warm dense fluids, and to quantify the miscibility gap in hydrogen/helium mixtures. The experiment is based on the generation of a laser shock in a precompressed sample. The precompressed target offers two new opportunities over the usual cryogenic targets: mixtures of H_2/He can be studied, whereas they phase-separate in a cryogenic target; the initial density of the mixture

can be significantly increased. Measurements on He, H_2, and H_2/He samples have been performed up to precompressions of 1.5 GPa. The Hugoniot data on helium have been published.[7,22] The Hugoniot data on H_2 and D_2 have been recently measured, and their analysis is being finalized for publication (Fig. 124.95).
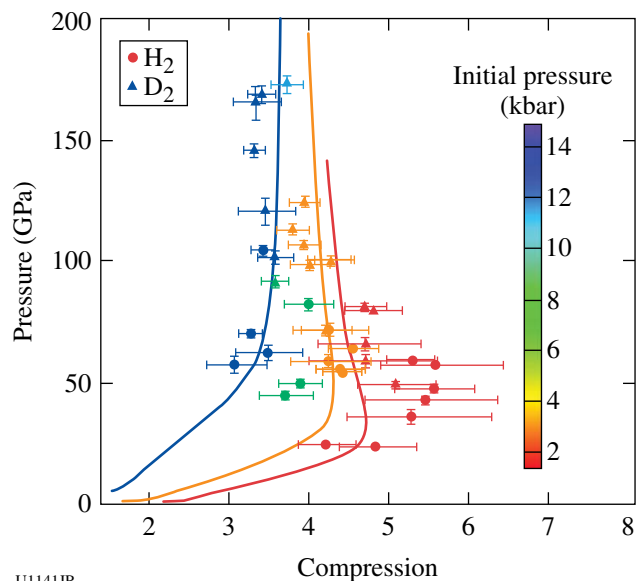

U1141JR

Figure 124.95
Summary of Hugoniot measurements collected at Omega on H_2 (dots) and D_2 (triangles), with the color scale indicating the initial pressure of the sample. The agreement between D_2 and H_2 measurements validates the impedance-matching construction that we used based on quartz with a Grüneisen equation of state of molten SiO_2. The full lines represent *ab-initio* calculations for comparable Hugoniots.

Last year, a special effort was made to extend the precompression on H_2/He mixtures to cover the thermodynamic domain where phase separation of the mixture is predicted to occur in the interiors of Jupiter and Saturn. To reach this domain, a precompression of more than 4 GPa is needed, and this has been achieved by a new design of diamond window with lateral support (Fig. 124.96). A typical diameter of the H_2/He sample is 300 μm, and, as a result of this new design, 6 kJ have been effectively coupled to the target.

The shock state is monitored through the back diamond using in-line imaging VISAR, along with streaked optical pyrometry (SOP) for temperature. Quartz is the reference material used as a standard for impedance-matching determination of pressure and density and relative measurements of reflectivity and temperature.

Data for H_2/He mixtures have been obtained along three Hugoniots corresponding, respectively, to a precompression of 0.4 GPa, 2 GPa, and 4 GPa (Fig. 124.97). The data have been
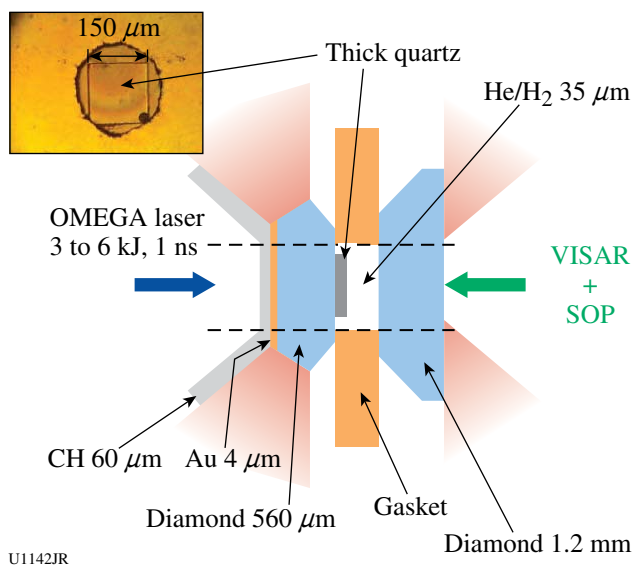

U1142JR

Figure 124.96
Experimental layout: schematic cross section of a precompressed target at 4 GPa. The inset (upper left) shows a picture of the sample before the shot.
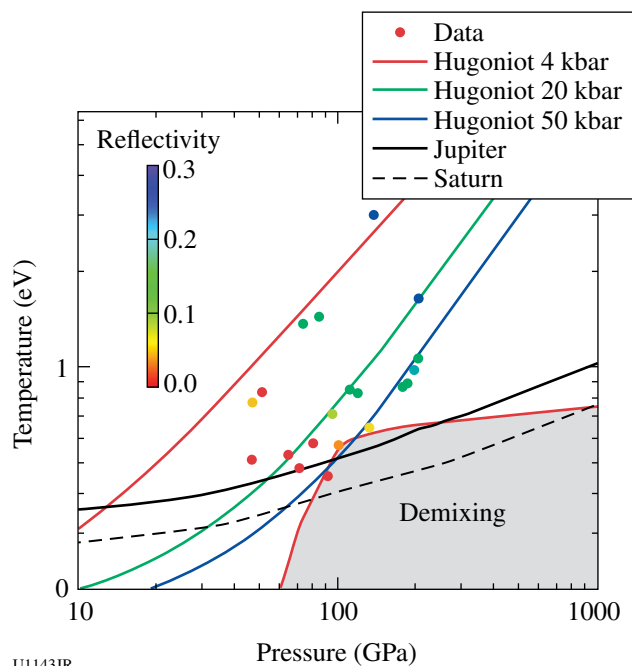

U1143JR

Figure 124.97
Hugoniot measurements on precompressed H_2/He mixtures collected along three paths, corresponding to precompressions of 0.4, 2, and 4 GPa at ambient temperature. The color scale gives the observed reflectivity. The phase-separation domain, calculated by *ab-initio* calculations, is given by the light red–colored domain. Isentropes for the interiors of Jupiter and Saturn are indicated by solid and dashed black lines, respectively.

collected under conditions for which H_2 is electrically conducting (metallic fluid) but He is not. The order-of-magnitude range of precompressions significantly shifts the Hugoniot points to a higher density and cooler temperature. Therefore, the measured Hugoniot of fluid H_2/He precompressed to 4 GPa crosses the Jupiter adiabat. The signature of phase separation—a jump in reflectivity along the Hugoniot—is not observed here. These data are just at the limit of the domain at which phase separation has been predicted by theoretical calculations.[23] It appears that the calculations may be overestimating phase separation; therefore, there is no phase separation within Jupiter.

Three-Dimensional Studies of Low-Adiabat Direct-Drive Implosions on OMEGA

Principal Investigators: R. C. Mancini (University of Nevada, Reno) and R. Tommasini (LLNL)
Co-investigators: J. A. Delettrez and S. P. Regan (LLE); V. A. Smalyuk (LLNL); and L. A. Welser-Sherrill (LANL)

Determining the spatial structure of implosion core temperature conditions is important for inertial confinement fusion experiments. The emphasis of this NLUF research is to establish the direct-drive multi-monochromatic imager's (DDMMI) instrument capabilities and to develop a quantitative method for spectrally resolved image data analysis with the goal of studying the 3-D spatial structure of implosion cores in low-adiabat OMEGA direct-drive implosions. In this connec-

tion, the team has demonstrated that processing the spectrally resolved image data recorded with DDMMI produces several types of images or spectra, namely (1) broadband images, (2) narrowband images, (3) spatially integrated spectra, and (4) spatially resolved spectra. Figure 124.98 shows gated, spectrally resolved images from an argon-doped implosion core recorded by DDMMI in OMEGA shot 49956. The red dots indicate the location of the image centers.

Being able to obtain spatially resolved spectra from the spectrally resolved image data recorded with DDMMI is important because the problem of extracting the 3-D spatial structure of the implosion core can be cast in terms of analyzing a series of spatially resolved spectra recorded simultaneously along three quasi-orthogonal lines of sight (LOS's). Electron-temperature and density spatial information is encoded in the intensity and broadening changes observed in the spectra. This type of 3-D analysis for the reconstruction of spatial structure is called a *polychromatic tomography* since, unlike the tomography techniques commonly used in medicine, we work with a limited number of LOS's but we benefit from having multiple chords and multiple wavelengths associated with each LOS.

To implement the idea of polychromatic tomography, we perform searches in parameter space driven by a Pareto genetic algorithm (PGA), for the temperature and density spatial distributions that yield the best simultaneous and
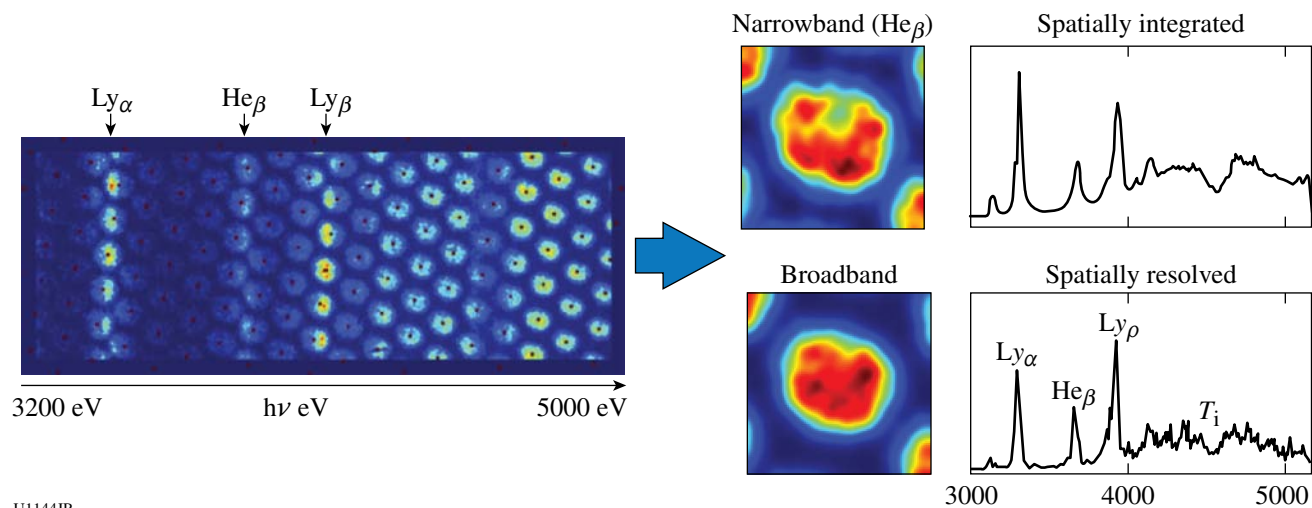
Figure 124.98
Gated, spectrally resolved images of the implosion core recorded by the DDMMI instrument in OMEGA shot 49956, and broad- and narrowband core images and spatially integrated and a sample of spatially resolved spectra extracted from these data. The line emission spectral features are due to the Ar tracer added to the D_2-gas fill of the core. At high photon energies, line absorption caused by a Ti tracer located in the shell is also observed. Color coding is adjusted for the visualization of each image.

self-consistent fits to all spatially resolved spectra recorded along the three quasi-orthogonal LOS's. The PGA combines a genetic algorithm with the Pareto domination technique of multi-objective optimization. This implementation of poly-chromatic tomography is an example of multi-objective data analysis, where the key question is what can be extracted by analyzing simultaneously and self-consistently multiple pieces of data that cannot be extracted by analyzing each piece of data on an individual basis? In previous and cur-rent NLUF research, several applications of multi-objective data analysis to x-ray spectroscopy of implosion cores have been developed. It should be noted that this method is unbi-ased since each PGA run with the same data starts from a randomly initialized first generation of populations (i.e., solution candidates), and the same data set can be analyzed multiple times starting from different first generations in an effort to check the uniqueness of the solution. Moreover, the result obtained with the PGA is subsequently fed to a Levenberg–Maquardt nonlinear least-squares minimization method that quickly improves the search by performing a "fine-tuning" step to find the optimal solution. Before apply-ing this analysis method to actual data, the technique was extensively tested with a series of synthetic data test cases. Polychromatic tomography of data from several OMEGA implosion experiments has been performed, and work is in progress to compare this data with 2-D and 3-D hydrody-namic simulations.

Response of BCC Metals to Ultrahigh Strain Rate Compression

Principal Investigator: M. Meyers (University of California, San Diego)
Co-investigators: B. Maddox, H. S. Park, B. Remington, S. Pollaine, and S. Hau-Riege (LLNL); and J. Wark (Oxford)

The goal of this campaign was to recover isentropically compressed Ta samples of various microstructures, from single crystal to nanocrystal, and to measure the loading profile using Al/LiF targets and the TIM5 ASBO (active shock breakout) on the OMEGA laser. The experimental setup is shown in Figure 124.99 and consisted of two targets simultaneously driven using a set of six beams each, one target aligned along the H3–H18 axis and the other along the H7–H14 axis. The configuration shown in Fig. 124.99 shows a VISAR witness target on H7–H14 and the Ta recovery sample on H3–H18. The VISAR witness targets were 1-mm-thick LiF coated with 10 μm of aluminum and mounted on a 10-mm-diam washer. The LiF was surrounded by a 3-mm-long Au cylinder that shielded the LiF from unconverted light. The recovery targets
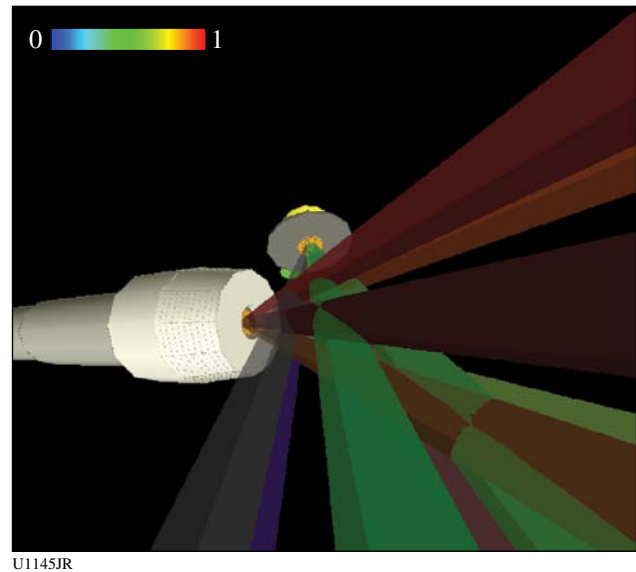

U1145JR

Figure 124.99
Experimental setup for BCCMet-10A showing the Ta recovery target along the H3–H18 axis and the VISAR witness target along the H7–H14 axis. The VISAR target was replaced with another recovery target after the first four shots.

consisted of a 5.5-cm-long stainless-steel recovery tube filled with 50 mg/cc of aerogel for soft recovery of laser-driven samples. The Ta target package was mounted at the end of the recovery tube and consisted of a 20-μm-thick polycarbonate ablator backed by a 180-μm BrCH (2%) reservoir. This abla-tor/reservoir was separated from the sample to be studied by a 300-μm-thick washer. The isentropic drive was created by the unloading of the BrCH reservoir across this gap. The VISAR target was replaced by a second Ta recovery target after the first four shots. A total of 12 successful shots were completed, resulting in 20 recovered samples, and four successful drive measurements were obtained. The recovered targets are cur-rently being analyzed using contact profilometry, scanning electron microscopy, transmission electron microscopy, and x-ray diffraction.

Proton Radiography of Direct- and Indirect-Drive ICF Experiments and HEDP Plasmas

Principal Investigators: R. D. Petrasso and C. K. Li (Massa-chusetts Institute of Technology)
Co-investigators: F. H. Séguin and J. A. Frenje (MIT); J. P. Knauer (LLE); and J. R. Rygg (LLNL).

During the present and previous NLUF programs, the MIT-developed method of monoenergetic, charged-particle radiogra-phy[24] has been used in new types of studies of electromagnetic fields and plasmas in high-energy-density physics (HEDP) and

in inertial confinement fusion (ICF) physics. These projects, undertaken at the Omega Laser Facility,[25] were performed because of their importance to the future of ICF, HEDP, and the physics of fields generated by laser–plasma interactions. Topics studied include the imaging, identification, and measurement of electric and magnetic fields in laser-generated plasmas; reconnection of megagauss magnetic fields in high-β plasmas; self-generated electromagnetic fields in ICF implosions; the dynamics of ICF capsule implosions; and electromagnetic fields in laser-driven hohlraums. This work has resulted in nine publications in Science[26,27] and Physical Review Letters,[28–34] plus seven other papers, eleven invited talks, and many contributed talks at conferences. The experiments have successfully addressed basic physics issues and those issues directly relevant to the future success of ignition experiments at the National Ignition Facility (NIF). These NLUF experiments also provided unique research opportunities for the seven MIT graduate students in HEDP and will result in major parts of their theses.

As described in the 2010 Science article,[27] the first observations and measurements of indirect-drive ICF implosions and self-generated fields using monoenergetic proton radiography were conducted during this project.[24] The experimental setup and data are shown in Fig. 124.100. The hohlraums were of OMEGA scale-1.5 size with a 30-μm-thick Au wall, 100% laser entrance hole (LEH), 2.4-mm diameter, and 3.8-mm length. Each hohlraum was driven by 30 laser beams forming four irradiation rings with a total laser energy ~11 kJ in a 1-ns square pulse. The individual laser beams had full spatial and temporal smoothing. The radiographs, made with 15-MeV D^{3}He protons, covered a typical indirect-drive ICF implosion sequence. The images are displayed to show proton fluence versus position, providing time-dependent information about field distributions, capsule compression, and hohlraum plasma conditions. A striking feature in these images is a five-pronged, asterisk-like pattern surrounding the imploding capsule—a consequence of the laser-beam positions on the hohlraum wall. It was shown that the asterisk spokes were formed between two expanding plasma bubbles that were generated by "nearest neighbor" laser-beam pairs, while the periodic patterns (narrow fingers) between these spokes were associated with the remaining laser-beam distributions. Plasma flow, supersonic jets, and self-generated B fields were observed; the areal density (ρR) and implosion symmetry were determined; and different implosion phases were sampled. The views of the spatial structure and temporal evolution of both the drive and implosion properties provide essential insight into, and modeling validation of, x-ray–driven implosions.
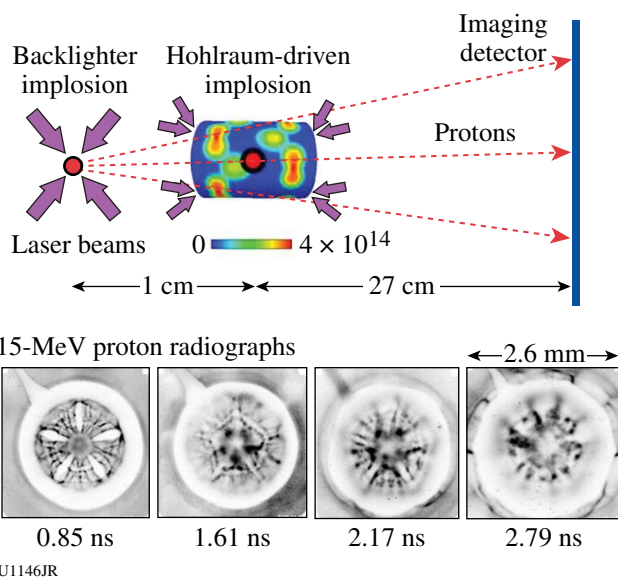

Figure 124.100
A recent experiment at the Omega Laser Facility used fusion to study fusion. A laser-driven ICF capsule produced monoenergetic 3- and 15-MeV protons through fusion reactions, and the protons were used to make radiographs of another ICF capsule imploded by x rays generated by the interaction of 30 laser beams with the inner wall of a Au hohlraum. The colors inside the hohlraum wall indicate laser intensity in units of watts per cm^2. In the 15-MeV radiographs shown here (recorded at different times during the laser drive), the capsule is in the center, the Au hohlraum is the light-colored outer ring, and the patterns between capsule and hohlraum are due to electromagnetic fields and plasma jets. Within each image, darker means higher proton fluence. This work is discussed in Ref. 27.

### Intense Laser Interactions with Low-Density Plasmas Using OMEGA EP

Principal Investigators: L. Willingale, A. Maksimchuk, and K. Krushelnick (University of Michigan)
Co-investigators: P. M. Nilson, R. S. Craxton, C. Stoeckl, and T. C. Sangster (LLE); J. Cobble (LANL); and P. Norreys and R. Scott (RAL)

Propagation of high-power, short-duration laser pulses through underdense plasma is of interest to research areas such as understanding laser beam self-focusing, channel and blast wave formation, filamentation, soliton production, electron and ion acceleration, and x-ray generation. The formation of a channel through an underdense plasma by a 740-J, 8-ps (90-TW) laser pulse focused to a peak vacuum intensity of around 2.8×10^{19} W/cm^2 was investigated using proton probing. These parameters are relevant to conditions required for the hole-boring fast-ignition scheme.[35] The CH plasma–plume underdense target was created by a UV beam (2.5 ns, 1160 J in an 800-μm-diam focal spot). Two-dimensional *SAGE* modeling indicated that this produced a 650-μm-wide Gaussian density profile with

a peak density of 5.3×10^{19} cm^{-3} along the laser propagation axis. The proton beam was generated using the second short-pulse beam interacting with a 50-μm-thick copper target.

Figure 124.101 shows the interaction at an early time when the laser was still propagating through the plasma; the proton probe images illustrate the expansion of the channel, filamentation, and channel-wall modulations. The time at which the leading edge of the pulse arrived at focus and reached half-maximum intensity is defined as t_0. Self-correction of the filaments into a single channel is seen from the single-shot sequence on the right side of Fig. 124.101. Bubble-like structures, which develop at later times, are illustrated in Fig. 124.102 by the proton probe images from shots with different relative beam timings. Two-dimensional particle-in-cell simulations are being performed to identify the origin of the channel-wall modulations and bubble structures.
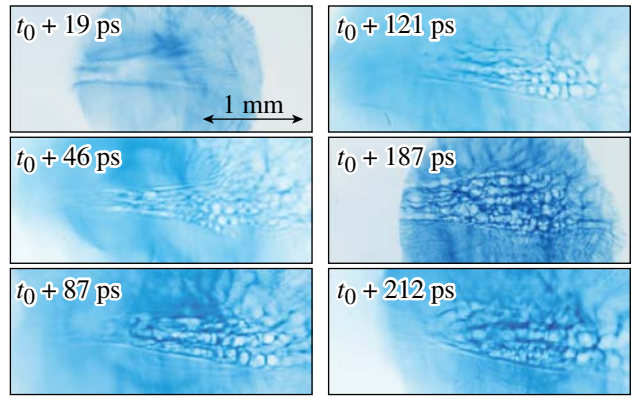
U1123JR

Figure 124.102
Proton probe image sequence from shots with different relative beam timings, which show the temporal evolution of the channel and the formation of bubble-like structures.
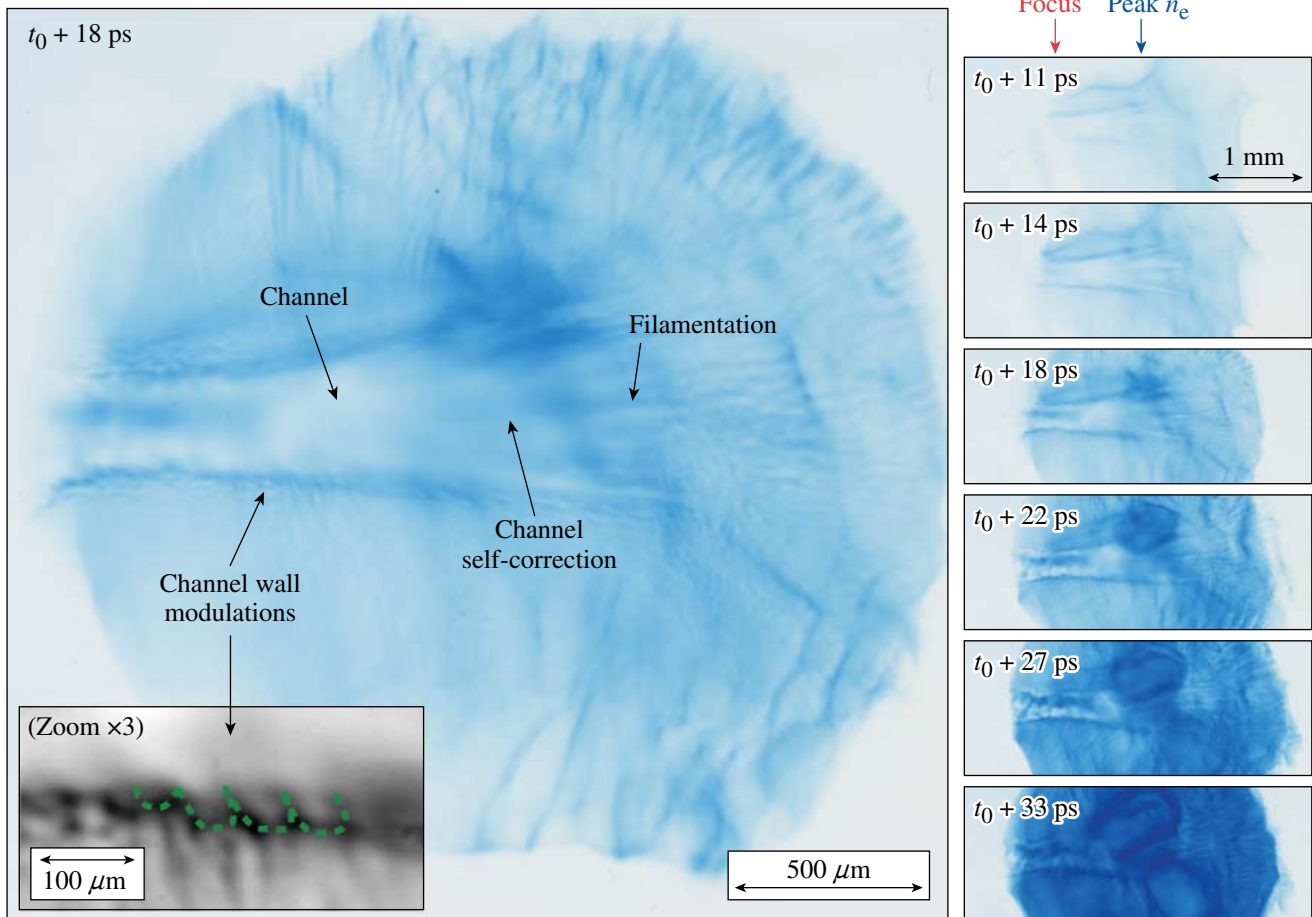
U1122JR

Figure 124.101
Proton probe images of the laser pulse propagating through the plasma from left to right. The time sequence is shown on the right-hand side and shows channel-wall modulations, filamentation, and channel self-correction.

FY10 Laboratory Basic Science Programs

In FY10, LLE issued a solicitation for LBS proposals to be conducted in FY11. A total of 23 proposals were submitted. An independent review committee comprised of Prof. Farhat Beg (University of California, San Diego), Dr. Robert Heeter (LLNL), Prof. Karl Krushelnick (University of Michigan), Dr. Carolyn Kuranz (University of Michigan), Dr. Nicholas Lanier (LANL), Prof. Roberto Mancini (University of Nevada, Reno), Dr. Rick Olson (SNL), Prof. Stephen Padalino (State University of New York–Geneseo), Dr. Wolf Seka (LLE), and Dr. John Soures (Committee Chair, non-voting) reviewed the proposals and recommended that 16 proposals receive 29 shot days on the Omega Laser Facility in FY11. Table 124.VI lists the successful LBS proposals.

Eleven LBS projects were allotted Omega Facility shot time and conducted a total of 303 target shots on the facility in FY10. This work is summarized in this section.

Producing Pair Plasma and Gamma-Ray Burst Using OMEGA EP
Principal Investigator: H. Chen (LLNL)

In August 2010, an LLNL/LLE/NRL team performed an LBS experiment on the OMEGA EP Laser System to study positron production in high-intensity–laser interactions with high-Z targets. This experiment was a follow-up to that in April 2009 where a record number of positrons were produced using the 1-kJ, 10-ps OMEGA EP backlighter interacting with a 1-mm-thick Au target.[36] The 2010 experiment had two main objectives; to examine the positron acceleration and to measure the high-energy gamma radiation. The results are shown in Figs. 124.103 and 124.104 for the positron energy spectra and gamma spectra, respectively. Quasi-monoenergetic positrons with energies peaked at ~25 MeV, the highest positron energy from lasers, were observed. This is nearly 7 MeV higher than that observed in previous OMEGA EP experiments. It is attributed to more-efficient acceleration using laser normal incidence on the same target. The experiments were the first time that high-energy (up to 1 MeV) gamma radiation was observed in laser–solid interaction using a single-hit charge-coupled–device (CCD) detector. This information is important to understanding the physics of laser–plasma interaction that produced electron–positron pairs. The misalignment of the diagnostic and the misfocusing of the laser beam caused by the debris shield made it impossible to observe the electron–positron annihilation feature.

Positron research extends over diverse fields from particle physics and astrophysics to medical applications. These appli-
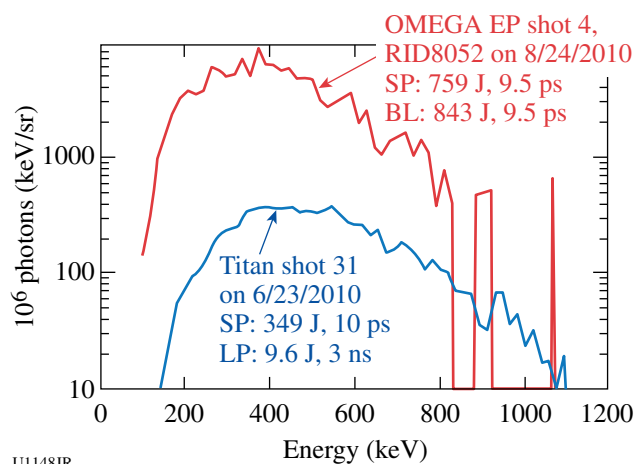
Table 124.VI: Approved FY11 LBS proposals.

Principal Investigator	Institution	Project Title
H. Chen	LLNL	Exploring Pair Plasma and its Applications Using OMEGA EP
S. X. Hu	LLE	Charged-Particle Stopping Power in Warm Dense Plasmas
R. Betti	LLE/FSC	Shock-Ignition Experiments on OMEGA
I. V. Igumenshchev	LLE	Investigation of Self-Generated Electromagnetic Fields in Directly Driven ICF Implosions Using Proton Radiography
D. Hicks	LLNL	Multi-Megabar Ramp Compression: Studies Using X-Ray Absorption Fine Structure
R. A. Kritcher	LLNL	Capsule Adiabat Measurements with X-Ray Thomson Scattering
P. Patel	LLNL	Electron Source Characterization for Cone-Guided Fast Ignition
S. P. Regan	LLE	Diagnosing P, ρ, n_e, T_e, Z of H/He, CH_4, and NH_3 Warm Dense Matter
G. Fiksel	LLE	Laser-Driven Magnetic-Flux Compression Experiments on OMEGA
V. A. Smalyuk	LLNL	Measurement of Ablative Rayleigh–Taylor Instability in Deeply Nonlinear Regime
R. Smith	LLNL	Measurement of Nucleation and Growth of the Fe α-to-ε Phase Transformation
B. Maddox	LLNL	Ultrahigh Pressure Lattice Dynamics in High-Z Materials
H. Park	LLNL	Astrophysical Collisionless Shock Generation in Laser-Driven Experiments
O. Hurricane	LLNL	Measurements of Linear, Nonlinear, and Turbulent-Mixing Regimes in Kelvin–Helmholtz Instability in the Subsonic Regime
C. Stoeckl	LLE	Fast-Electron Transport in Solid-Density Matter
J. M. McNaney	LLNL	Short-Pulse-Laser–Based Neutron Resonance Spectrometry
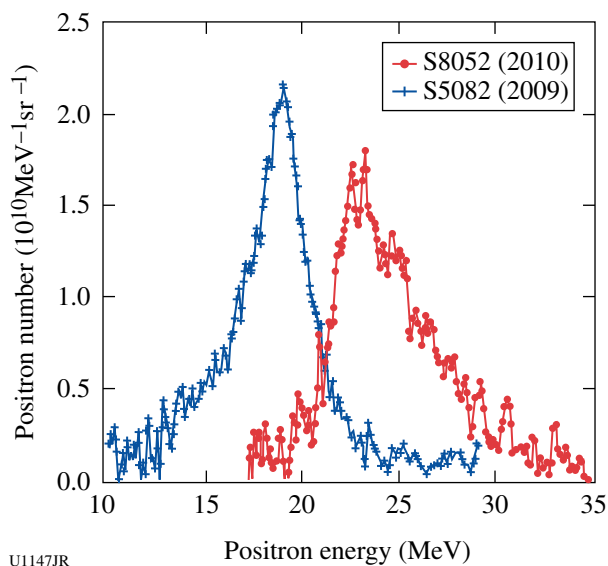
Figure 124.103
Positron spectrum measured on the OMEGA EP laser.

Figure 124.104
High-energy gamma spectrum measured by the NRL single-hit CCD detector.

cations often require the production of large numbers of positrons on a short time scale, which have been difficult to supply. The new OMEGA EP results could significantly affect the quest for a laser-produced positron source for research in these fields.

Measurements of the Viscosity of Shock-Compressed Fluids: Studies of Water and Silica (Viscosity-10A)
Principal Investigator: P. M. Celliers (LLNL)

The Viscosity-10A campaign was carried out as part of the LBS program. The goal was to demonstrate a method for determining the viscosity of a high-pressure fluid created by the propagation of a strong shock front through an initially transparent sample. In this campaign the sample under study was liquid silica (SiO_2), produced by propagating a shock through samples of either alpha-quartz or fused SiO_2. The viscosity of high-pressure liquid SiO_2 has obvious geophysical relevance, and measurements in the Mbar domain are not possible with conventional methods. The measurement technique is based on observing the evolution of a spectrum of perturbations imposed on a multi-Mbar shock front passing through the sample material. The viscosity of the liquid state just behind the shock front is expected to influence the decay rate of the perturbations as the shock front propagates, and detailed measurements of the perturbation state can be compared with calculations to assess the viscosity. The measurement technique employed the OMEGA high-resolution velocimeter (OHRV) to observe the velocity perturbations directly on the surface of the reflecting shock front. The shocks were driven using a hohlraum coupled to a 50-μm polystyrene ablator followed by the sample. The perturbation spectrum was generated by an etched array of shallow pits, a few microns deep and 10 μm in diameter, that were created on the sample surface at the interface with the ablator. As the shock passed through this interface, the perturbations created a pattern of expanding ripples riding on top of the shock front, which were detected and measured quantitatively by the OHRV (Fig. 124.105). During the campaign,
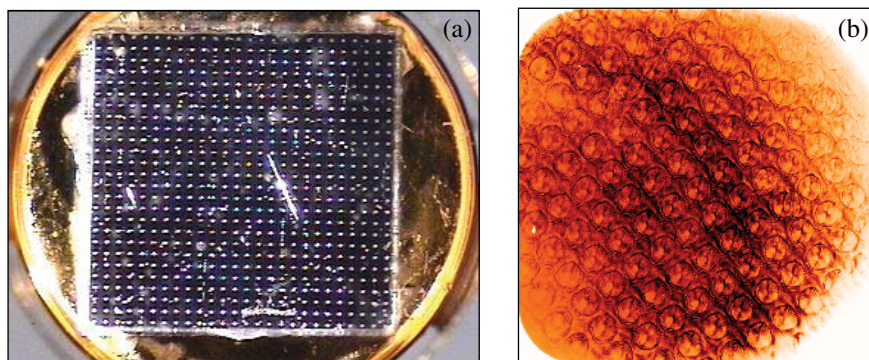
Figure 124.105
(a) Example of a fused-SiO_2 viscosity target sample with the etched array of pits clearly visible in the metrology photograph; the hohlraum is behind the sample. (b) Raw intensity record from one of the channels of the OHRV for the same target probed at 2.6 ns following the passage of a shock through the perturbed interface, showing the probe light reflected directly from the shock front and revealing the pattern of expanding ripples created by the array of etched pits.

we carried out three drive-characterization experiments using ASBO/SOP to characterize the shock velocity. These were followed by eight perturbation experiments probing 3-Mbar and 6-Mbar shocks in the SiO$_2$ samples. High-quality data were recorded on all shots.

Optical Properties of LiF

Principal Investigator: D. E. Frantanduono (LLE)
Co-investigators: M. A. Barrios, T. R. Boehly, and D. D. Meyerhofer (LLE); and D. G. Hicks, J. H. Eggert, R. Smith, and P. M. Celliers (LLNL)

Direct laser ablation was used to ramp-compress lithium fluoride (LiF) to 800 GPa. LiF was observed to remain transparent over this pressure range; this is the highest-pressure insulator ever observed. The refractive index of ramp-compressed LiF was measured up to 800 GPa and observed to increase linearly with compressed density over this range. These highest-pressure measurements of refractive index to date were used to infer the pressure-induced band-gap closure of compressed LiF. An effective single-oscillator model of this behavior shows that the optical gap closes monotonically with increasing density.

Extrapolation of these results suggests that metallization of LiF should occur at pressures of 4200 GPa. If true, LiF will prove to be a valuable window for extremely high pressure, ramp-compression experiments.

Ion-Acoustic Wave Instability from Laser-Driven Return Currents

Principal Investigators: D. H. Froula, S. X. Hu, and J. F. Myatt (LLE)
Co-investigators: J. S. Ross, L. Divol, and S. H. Glenzer (LLNL)

Thomson-scattering measurements of the amplitude and frequency of ion-acoustic waves show an instability when ion-wave damping is reduced. Experimental results from the OMEGA laser used simultaneous measurements of the electron-plasma wave and ion-acoustic wave features to characterize the plasma (T_e, T_i, Z, n_e) and to directly probe the amplitude of the ion-acoustic waves (Fig. 124.106). The ion Landau damping was varied by changing the target material: CH, V, Ag, and Au. For plasma conditions where the ion Landau damping was large $\left(ZT_e/T_i = 10\right)$, the amplitude of the ion-acoustic waves was stable. Reducing the ion Landau damping $\left(ZT_e/T_i = 30\right)$ increased the amplitude of the ion wave, but the electron Landau damping was sufficient to maintain stability. The ion-acoustic waves became unstable when the ion Landau damping was weak $\left(ZT_e/T_i = 70\right)$. As the waves grew to wave-
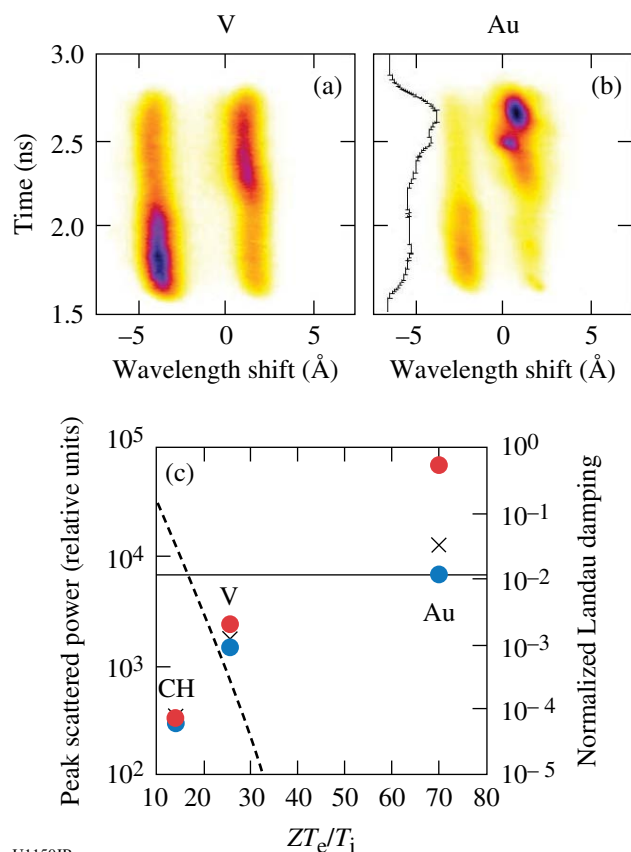
Figure 124.106
(a) The Thomson-scattering spectrum provides a measurement of the electron temperature, density, charge state, and, from the asymmetry in the scattered power between the ion-acoustic features, the relative drift between the electrons and ions driven by the heat-flux–driven return current. (b) As the ion damping was reduced, the system became dominated by the electron Landau damping, which became Landau growth in the weakly damped systems.

breaking amplitudes, their frequency shifted and turbulence was expected. These results confirm the speculation that heat-flux–driven ion-acoustic fluctuations exist in laser-produced plasmas, which was previously invoked to increase the collision rate and account for anomalous absorption.[37]

X-Ray Absorption Fine Structure Measurements on Multishock Compressed Iron

Principal Investigators: Y. Ping and D. G. Hicks (LLNL)

X-ray absorption fine structure (XAFS) measurements were performed on iron that was multishock compressed to a few megabar. By dynamically compressing a few-micron-thick iron sample sandwiched between thin diamond anvils, near-constant pressure conditions were produced inside the iron, the bulk of the pressure evolution taking place in the adjacent, x-ray–transparent diamond anvils. A spherical, imploding

backlighter source was used to produce a smooth, broadband source of x rays for the absorption measurement. The VISAR was used to track the rear surface of the diamond from which the pressure inside the iron sample could be inferred. An example of an XAFS spectrum obtained at 3.5 Mbar is shown in Fig. 124.107. This was analyzed using the FEFF code[38] and found to give a compression in Fe of 1.6 and a temperature of 6000 K. Improved fits were found for a c/a ratio of 1.73, indicating that pressure, density, temperature, and c/a ratio could be obtained from a single shot.

Capsule Adiabat Measurements with X-Ray Thomson Scattering

Principal Investigators: A. Kritcher, T. Doeppner, O. L. Landen, and S. H. Glenzer (LLNL)

Experiments to characterize spherically imploded inertial fusion–type targets using x-ray Thomson scattering were recorded at the Omega Laser Facility in January and May of 2010 to study the properties of compressed ICF ablators. Measurement of the temperature and density allows one to infer the capsule adiabat—a measure of the plasma pressure normalized by the Fermi pressure—and can be used to test low-adiabat pulse-shaping methods. In these experiments the noncollective, or microscopic, particle behavior of imploding CH and Be shells was probed using a 9-keV Zn He$_\alpha$ x-ray source at scattering angles of 113° and 135°. Figure 124.108(a) shows a schematic of the experimental setup including time-resolved pinhole images of the imploding capsules. The capsules attached to Au half-cones were hemispherically driven using 36 drive beams. The Zn He$_\alpha$ probe was created by laser irradiation of a Zn foil positioned on the inside of the Au cone. Figures 124.108(b) and 124.108(c) show radiation–hydro-dynamic calculations of the mass density as a function of time and radius for the two pulse shapes used in these experiments.

Figure 124.109 shows scattering spectra from Be (+2) capsules driven with pulse shape LA2201 shown in Fig. 124.108(b), at 4.2 ns after the start of the drive beams and a scattering angle of 135°. The measured electron density and temperature determined from theoretical fitting to the experimental data was 14±3 eV and 1.1±0.15 × 10^{24}/cc, respectively. For these partially degenerate plasmas, the width of the inelastic Compton feature provided the electron-velocity distribution, which is a direct measure of the electron density. The electron temperature was determined from the semi-Gaussian shape of the Compton feature, independent of the choice of structure factor model. Sensitivity of theoretical fitting to the red wing of the Compton feature for varying electron temperatures is shown in Fig. 124.109. In this geometry, the larger scattering angle of 135° resulted in the Compton red wing shape depending less on the finite size of the source and scattering volume, enabling us to better determine the temperature and density. Also, with this new geometry we were able to use additional probe beams, which resulted in an increase in signal to noise. These experiments demonstrate the viability and investigate the error in using this diagnostic to study the properties of implosion targets at the National Ignition Facility.
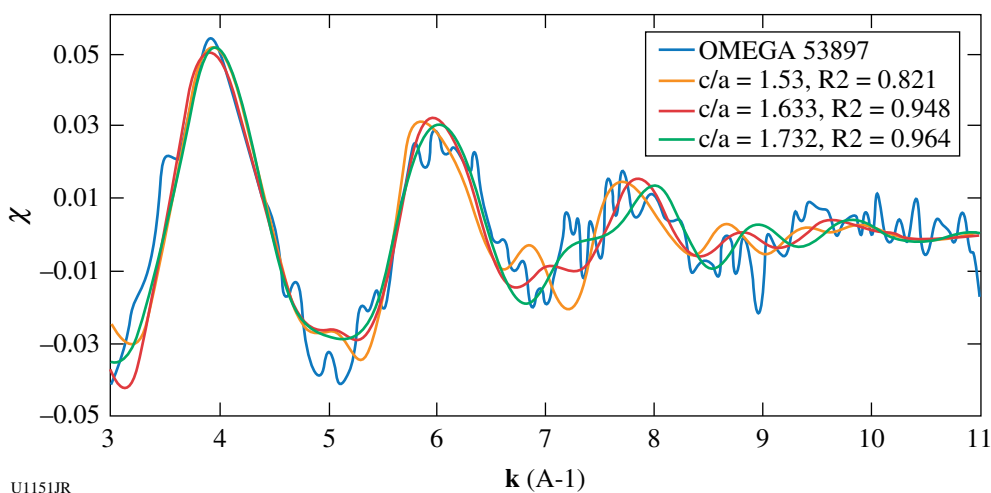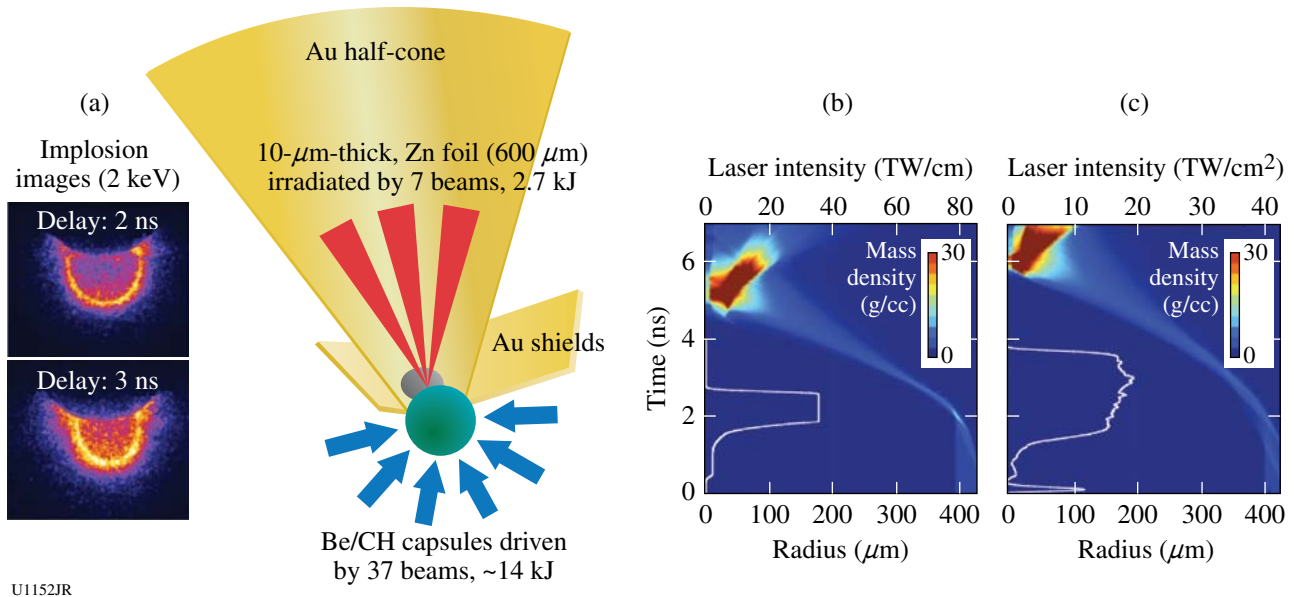

U1151JR

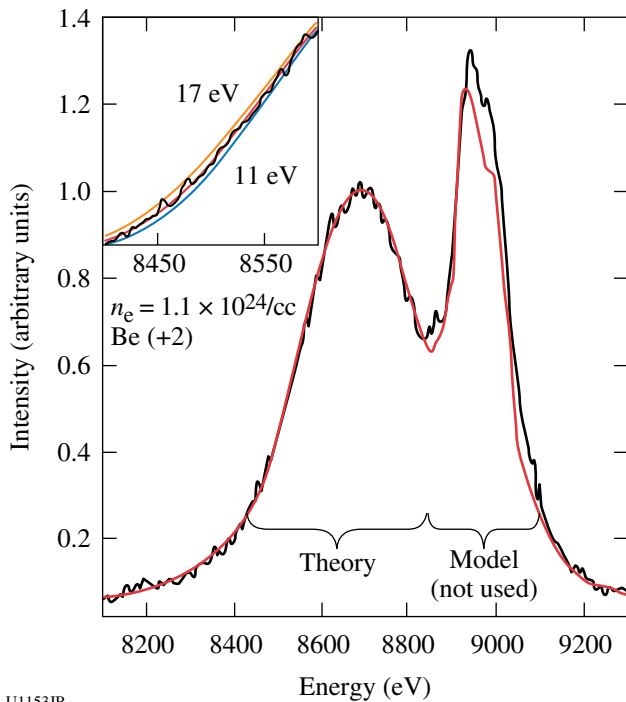Figure 124.107
XAFS spectrum of iron compressed at 3.5 Mbar. The residual, normalized x-ray absorption coefficient χ (dimensionless) plotted versus wave vector **k** (inverse angstroms) is fit to an hcp crystal configuration to determine the density, temperature, and c/a ratio.

U1152JR

Figure 124.108

(a) Schematic of the experimental setup. Here, Zn He$_\alpha$ x rays, produced via laser irradiation of a 10-μm-thick Zn foil, were scattered from imploding Be and CH capsules that were compressed using 36 additional shaped laser beams. The Zn foil was attached to gold half-cones with Au flaps that shielded the detector from the source x rays. Also shown (left) are time-resolved x-ray images of the implosion. (b) and (c) Radiation–hydrodynamic calculations of the mass density, plotted as a function of time and target thickness, where $t = 0$ denotes the start of the drive beams. Profiles of the drive-beam waveforms (white) are overlaid on the mass-density contour, listed as a function of time and laser intensity.

U1153JR

Figure 124.109

In-flight x-ray Thomson scattering data (4.2 ns) from laser-compressed Be cone-in-shell targets [see Fig. 124.108(b) for the drive-pulse shape]. Data include an elastically scattered Raleigh peak at ~9 keV and an inelastically scattered Compton feature at ~8.7 keV. Theoretical fits to the experimental data yielded an electron temperature and density of about 14 eV and 1.1×10^{24}/cc, respectively.

Study of High-Z Material Properties Under Compression Using High-Energy Backlighter Diffraction
Principal Investigators: B. Maddox and H. S. Park (LLNL)

This project was carried out as a series of four distinct series of shots on the OMEGA EP Laser System under the series name of DynDiff.

DynDiff-10A. This experimental campaign was designed to test two different diffraction schemes, Bragg (reflection) and Laue (transmissions), for diffraction off high-Z metals using x rays produced by laser-driven foil targets. Two new diagnostics were designed to accomplish this: For Bragg diffraction, the Bragg diffraction imager (BDI) consists of a large Hevimet housing and an Al arm that holds a Hevimet beam block close to the crystal target. The beam block prevents the x rays from the backlighter from reaching the detector while making it possible for diffracted x rays to pass. For Laue diffraction, the Laue diffraction imager (LDI) consists of the same Hevimet housing as the BDI, but with a collimator snout instead of an Al arm. This collimator snout creates a collimated x-ray beam that then diffracts off a crystal housed inside. Figure 124.110 shows a drawing of the BDI diagnostic. The inset shows the front snout that attaches to the main body to turn the BDI into the LDI. Targets for Bragg diffraction consisted of 600-μm-thick Mo (111) crystals mounted onto glass stalks. Targets for Laue dif-

fraction consisted of 5-μm-thick Ta mounted on a rotation stage inside the LDI. X rays were produced by irradiating a metal foil using either the short-pulse backlighter beam (for Bragg diffraction) or the long-pulse UV beams (for Laue diffraction). Figure 124.111 shows an image obtained using the BDI on a Mo (111) crystal using a 17.478-keV Mo K$_\alpha$ backlighter. Similar quality results were obtained using the LDI to measure Laue diffraction from Ta single crystals. These results were used in DynDiff-10B to attempt to measure Bragg diffraction from a shock-compressed Mo crystal.
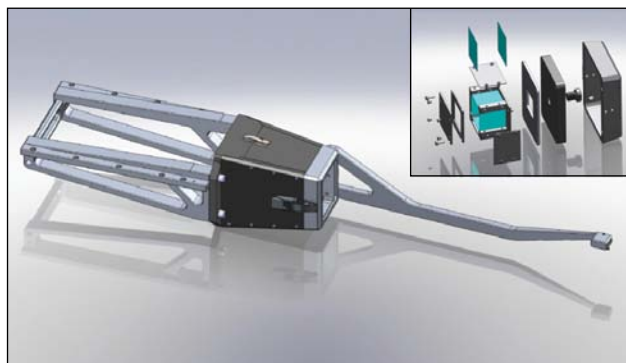
U1154JR

Figure 124.110
The Bragg diffraction imager (BDI). Inset shows the front nose assembly that turns the BDI into the Laue diffraction imager (LDI).
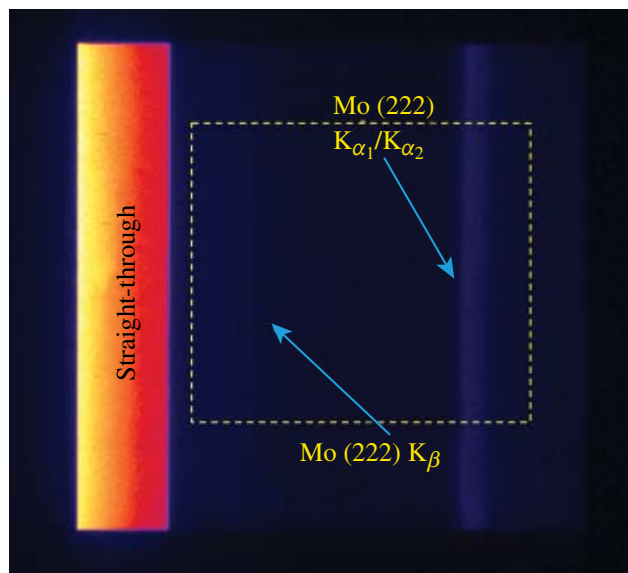
U1155JR

Figure 124.111
Diffraction image obtained using the BDI on a Mo (111) crystal using a 17.478-keV Mo backlighter.

DynDiff-10B. The goal of this campaign was to build on the success of DynDiff-10A to measure Bragg diffraction from a shock-compressed Mo (111) single crystal and to measure the drive characteristics of the OMEGA EP UV long-pulse beams using VISAR. The Mo crystal target consisted of a 600-μm-thick Mo (111) single crystal with a 20-μm parylene-n ablator and was mounted on a glass fiber stalk. The VISAR witness target was 1-mm-thick LiF coated with 10-μm-thick Al and mounted on a 7.5-mm-diam Al washer. The crystals and LiF targets were driven using a single long-pulse UV beam (Beam 4) using a 4-ns square pulse at an energy of 300 J and defocused to a 6-mm-diam spot. The x-ray backlighter target was a 250-μm-diam, 12-μm-thick Mo foil and was driven by the OMEGA EP short-pulse backlighter beam at 900 J in 100 ps with a 200-μm spot diameter. Good VISAR data were obtained; however, because of an alignment error of the BDI beam block, no driven diffraction was detected. It was concluded that the alignment tolerance was too tight and a new beam block needed to be designed that would allow for a greater alignment variance.

DynDiff-10C. The goal of this campaign was to measure Bragg diffraction of 17.478-keV Mo x rays off shock-compressed single-crystal Mo on OMEGA EP using a new, specially designed beam block and arm for the BDI that had a greater alignment tolerance than the original beam block. A secondary goal was to measure the shock-loading profile using Al/LiF targets and the TIM12 ASBO. A total of six target shots were conducted. The VISAR targets consisted of LiF (1 mm thick) coated with Al (10 μm thick) and a parylene-n ablator (20 μm thick), all mounted on a 7.5-mm-diam Al washer. Crystal targets consisted of a 6-mm-diam, 250-μm-thick Mo single crystal with a 20-μm-thick parylene-n ablator. Because of a target build error, no ASBO data were obtained during this campaign; however, the first driven Bragg diffraction using a petawatt-laser x-ray backlighter was observed. Figure 124.112 shows a diffraction image obtained using the BDI on a driven Mo (111) crystal along with a preliminary fit to the compressed diffraction pattern. The drive laser (UV beam 1) was set to 616 J in a 10-ns square pulse using a 5-mm-diam spot size and fired 7 ns before the backlighter beam. Although no ASBO data were obtained during this campaign, scaling from data obtained during the DynDiff-10B campaign suggests ~25-GPa peak pressure. The fit to the diffraction pattern shown in Fig. 124.112 gives a strain along the compression direction of ~5.8%. This technique was used during the DynDiff-10D campaign to measure the 3-D lattice relaxation time scale in bcc Mo by taking Bragg-diffraction snapshots, like the one shown in Fig. 124.110, at various times after the start of the laser drive.
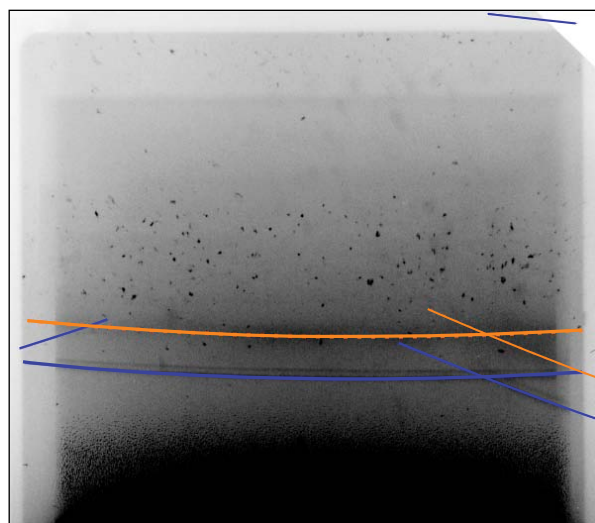
U1156JR

Figure 124.112
Diffraction pattern obtained using the BDI of a shock-loaded Mo (111) crystal and a 17.478-keV Mo backlighter. The solid blue and orange lines show fits to the undriven and driven portions of the lattice.

DynDiff-10D. This campaign was an extension of DynDiff-10C, and the goal was to use time-resolved Bragg diffraction to study the lattice dynamics of single-crystal bcc Mo. A total of five target shots were conducted: one VISAR shot to measure the laser drive and four successful diffraction shots at different times after initial compression. Targets were of the same design as those used in DynDiff-10C. The laser setup was also similar to that used during DynDiff-10C except for the introduction of a second UV drive beam (Beam 4) to enhance the drive uniformity across the crystal target. Figure 124.113 shows the
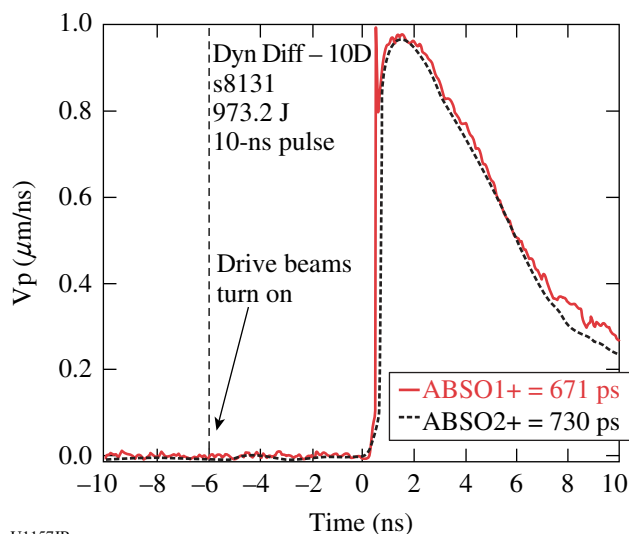
U1157JR

Figure 124.113
VISAR data obtained during the DynDiff-10D campaign.

VISAR data obtained. Using the shock-arrival time coupled with the Al thickness, the breakout time of the shock into the Mo crystals was calculated. Figure 124.114 shows a series of diffraction images taken at different times after the shock wave entered the crystal, starting with an undriven crystal. A compressed Mo (222) line is seen at a higher angle (left side of the images) that gradually shifts to lower compression. These data are currently being analyzed.
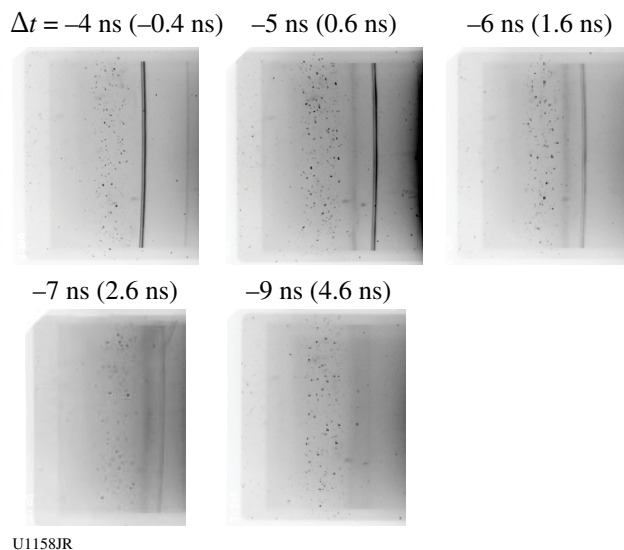
U1158JR

Figure 124.114
Diffraction plots as a function of time after compression for bcc Mo (111) showing a static (222) diffraction line and a compressed (222) line.

Relativistic Laser–Plasma Interaction
Principal Investigators: P. Patel (LLNL) and H. Sawada (University of California, San Diego)
Co-investigators: C. D. Chen, H. S. McLean, and M. H. Key (LLNL); T. Yabuchi and F. N. Beg (University of California, San Diego); R. B. Stephens and K. U. Akli (General Atomics); and W. Theobald, P. M. Nilson, and C. Stoeckl (LLE)

The objective of this campaign was to characterize fast electrons created by the high-energy OMEGA EP short-pulse laser interacting with planar and cone targets. The FY10 focus was on investigating two critical parameters: electron energy spectrum (T_{hot}) and conversion efficiency from laser to fast electrons (η). Experiments were performed using the OMEGA EP backlighter beam at 150 to 250 J in 1 ps and 1000 J in 10-ps–pulse duration. These laser parameters have been used in integrated fast-ignition (FI) experiments on OMEGA.[39] This study provided direct information about the electron source in integrated experiments.

Multilayer planar targets were used to measure up-to-750-keV bremsstrahlung emission to infer T_{hot} and η. A planar target is less sensitive to the beam-pointing stability, target positioning, and pre-pulse level compared to a cone. The target consisted of an ~1-mm-thick planar Al with a 25-μm-thick Cu layer buried at 100 μm from the front surface. To prevent electron refluxing caused by the sheath fields, 1-mm-thick CH was attached to the rear side. The x rays were measured with two bremsstrahlung x-ray spectrometers (BMXS's) at the rear side on the laser axis and 49° from the incoming laser axis. Figure 124.115 compares the measured signals on the stack of 15 imaging plates in the BMXS at 150 J in the 1-ps shot and 1000 J in the 10-ps shot. These raw data normalized by the laser energy indicate similar fast-electron spectra and conversion efficiencies at a laser intensity of ~5×10^{18} W/cm^2 at both 1 and 10 ps. The preliminary analysis using a Monte Carlo code ITS[40] shows that the total conversion efficiency is estimated to be 14% to 35% for the 1-ps shot and 13% to 37% for the 10-ps shot with an assumption of the classical ejection angle. For further analyses, a PIC simulation using simulated pre-plasma profile from a radiation–hydrodynamics code *HYDRA* will be performed to calculate the divergence of the electron beam. This electron source will be fed into a hybrid transport code calculating the bremsstrahlung emission to match the measurements. The inferred T_{hot} and η will be compared to the simulated results.

The study was extended to cone-wire targets, which are more relevant to integrated experiments. Cone-wire targets were used to study the electron production in the cone and transport through the cone tip to the wire, where transport is simplified to quasi 1-D geometry in the wire direction. Figure 124.116 shows the overview of the cone-wire experiment. The backlighter beam was focused onto the Au or Al cone tip to generate electrons. The electrons transported through the cone tip were coupled to the 1.5-mm-long (40-μm-diam) Cu wire attached to the cone tip. From the wire 8.05-keV K$_\alpha$ was measured with the absolutely calibrated DCHOPG spectrometer and a spherical crystal imager (SCI) for the imaging of the wire. A version of SCI was deployed for these experiments at the end of Q4. The inset of Fig. 124.116 shows the monochromatic image of the wire at 1000 J in a 10-ps shot (shot 8170). K$_\alpha$ yields were obtained as well as wire images at both 1- and 10-ps pulse durations. The falloff of the wire emission and the Cu K$_\alpha$ yield will be modeled with a hybrid transport code to infer the T_{hot} and coupling efficiency to the wire. The SCI will enable one to study another critical parameter in future experiments: the divergence of forward-going electrons.
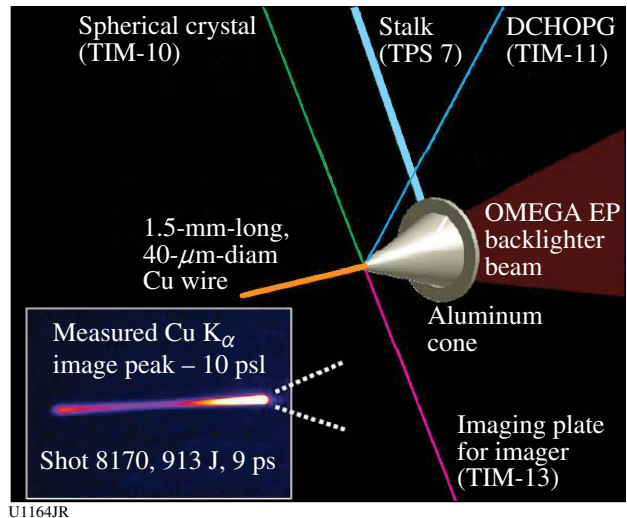
Figure 124.116
Experimental configuration of the cone-wire experiment. Inset: The measured monochromatic image of the Cu wire is shown for shot 8170.

Figure 124.115
Measured signals of front and rear bremsstrahlung spectrometers for 1-ps (shot 7694) and 10-ps (shot 7698) pulses.

Kinetic Behavior of Crystalline Iron Undergoing Multi-Mbar Compression and Release
Principal Investigators: R. Smith, Y. Ping, and D. G. Hicks (LLNL)

The kinetic behavior of iron during rapid compression and release was studied using x-ray absorption fine structure

(XAFS). A 4-μm iron sample, sandwiched between diamond layers, was multishock compressed up to 3.5 Mbar and then released (Fig. 124.117). The pressure history in the iron was tracked using a VISAR reflection from the rear diamond. By probing the XAFS spectrum of the iron on multiple shots before and after the peak of the compression wave, the rapid evolution of short-range atomic order in the crystal was examined. We observed that with increasing pressures, the spacing between XAFS peaks increased along with increased damping of the peaks at higher k. This indicates an increase in the density of the hcp phase from 1.65- to 1.8-fold compression and an increase in the temperature from 4000 to 10,000 K. These changes are undone on release of the wave. Detailed examinations are being made to determine whether the changes are fully reversible.
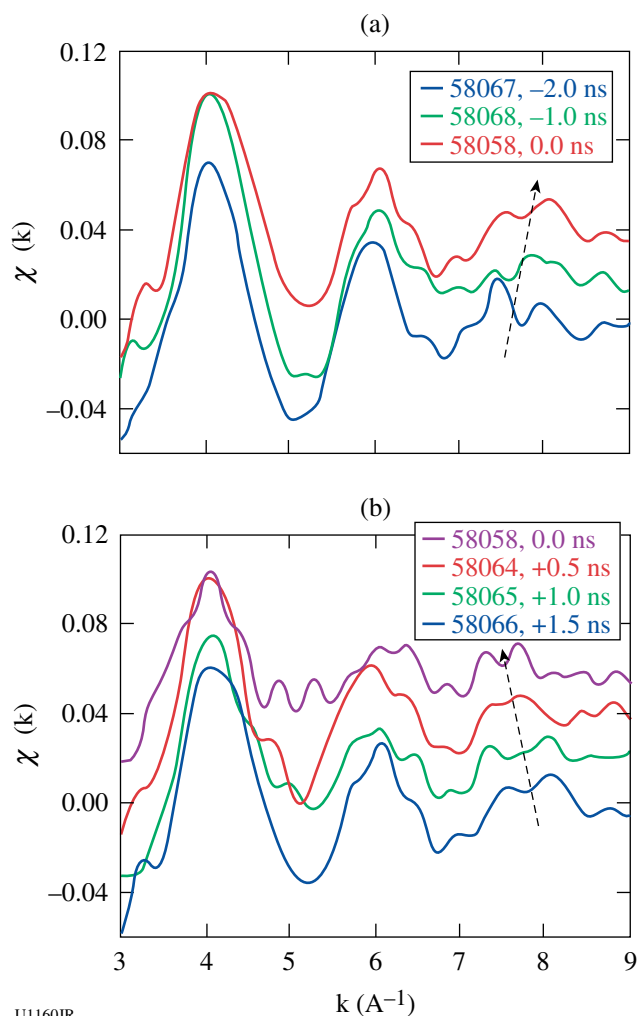
Figure 124.117
Changes in the Fe XAFS spectra observed on (a) compression and (b) release of a 3.5-Mbar pulse.

Integrated Shock-Ignition Experiments on OMEGA
Principal Investigator: R. Betti (LLE/FSC)
Co-investigators: W. Theobald, O. V. Gotchev, K. A. Anderson, and P.-Y. Chang (LLE)

Shock ignition is a two-step ICF scheme where ignition is achieved by launching a strong spherically convergent shock into the imploding capsule at the end of the compression. The laser intensities at the end of the pulse are $\sim 5 \times 10^{15}$ W/cm^2 and significantly higher than what is currently available with standard 60-beam implosions on OMEGA. A new experimental platform has been developed on OMEGA that uses 40 beams to compress D$_2$-filled plastic shells on a low adiabat and the remaining 20 beams to generate a strong shock. The 20 beams are delayed and tightly focused onto the imploding shell to reach intensities of up to $\sim 8 \times 10^{15}$ W/cm^2.

Initial 40-beam implosions had a strong $l = 2$ nonuniformity as shown in the two top pinhole-camera images in Fig. 124.118(a). The implosion was improved by repointing the 40 drive beams so that a more-uniform illumination was achieved. This is clearly seen in the two bottom x-ray pinhole-camera images shown in Fig. 124.118(b). The core brightness
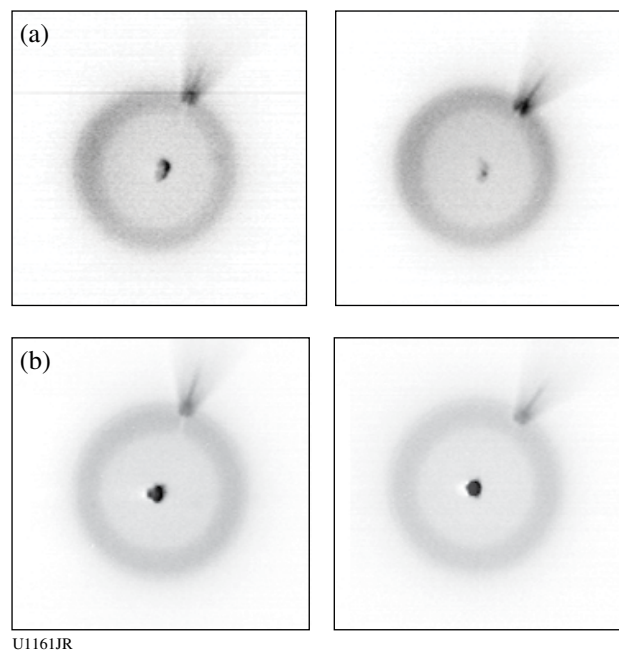

Figure 124.118
X-ray pinhole camera images from two different implosions. (a) Shot 52480, an implosion with 40 drive beams that were all pointed to the center of the capsule; (b) Shot 55737, an implosion where the 40 beams were repointed to achieve a more-uniform illumination. Two pinhole-camera images are shown for each shot.

increased and the shape of the core is more circular. By repointing the beams, the neutron yield increased by a factor of ~5 from $(2.6\pm1.1)\times10^8$ to $(1.5\pm0.2)\times10^9$. This shows that repointing significantly improved the symmetry of the implosion, reducing the calculated power imbalance from ~8% to ~3% root mean square.

Another objective of the campaign was to study the interaction of the 20 high-intensity beams. The neutron yield increased by a factor of 2 to $(3.3\pm0.2)\times10^9$ when the 20 beams were added to the optimized target. The plasma reflectivity was measured for various laser intensities from ~2 to 8×10^{15} W/cm². This was achieved through an intensity scan by shifting the focus of the 20 shock beams relative to the center of the shell. Figure 124.119 shows the measured fraction of (a) SBS and (b) SRS laser backscatter energy of one shock beam versus laser intensity. SBS increased moderately from 7% to 12% with intensity, while SRS increased by a factor of ~6 from 4% to 24% and dominated the backscattering at the highest intensity. The sum of SRS and SBS (c) increased from 10% to 36%.

The backscatter is highly directional. The simultaneously measured back-reflection through a neighboring drive-beam port was ~4%; it remained constant at all levels of intensities and was comparable to the measured backscatter for implosions without the 20 beams. About 10% of the high-intensity beam energy was converted into hot electrons with a temperature of 42 ± 5 keV, independent of laser intensity. The measurements indicate that SRS is the primary mechanism for generating the hot electrons with a relatively low temperature. No significant contribution from the two-plasmon-decay instability was observed. This would be beneficial for shock ignition since these electrons are stopped in a thin outer layer of the imploding target and might augment the strong hydrodynamic shock.

The reduction in driver energy caused by backscatter losses might be compensated by increasing the incident laser energy without the danger of preheating the target.

Integrated Core Heating for Fast Ignition
Principal Investigators: W. Theobald and C. Stoeckl (LLE)

This campaign had two primary objectives: First, the neutron-yield enhancement was measured from compressed deuterated plastic shells that were heated by fast electrons for various injection times of the short-pulse OMEGA EP laser. Second, the shock-breakout times in cone-in-shell targets were measured for the same compression condition as in the integrated fast-ignition shots for various cone-tip thicknesses.

Integrated fast-ignition experiments with hollow cone targets mounted into deuterated plastic shells were performed with 1 kJ of short-pulse energy and ~20 kJ of drive energy. The measured neutron yield as a function of the arrival time of the OMEGA EP pulse is shown in Fig. 124.120. The neutron yield peaks at a delay time of 3.65 ± 0.02 ns. The gray bar shows the yield without the OMEGA EP pulse. The measurement demonstrates an enhancement in neutron yield by more than a factor of 4 for a properly timed OMEGA EP beam. An additional yield of $(1.4\pm0.6)\times10^7$ was produced by the ultra-intense, short-pulse laser in a narrow time window of less than 100 ps. Data points in the peak were taken on several shot days, months apart, demonstrating high reproducibility of this experimental platform.

Integrated *DRACO + LSP* simulations were performed to estimate the coupling efficiency of fast electrons to the compressed core. The fraction of OMEGA EP laser energy that is coupled into the core is $3.5\pm1.0\%$. The coupling is lower
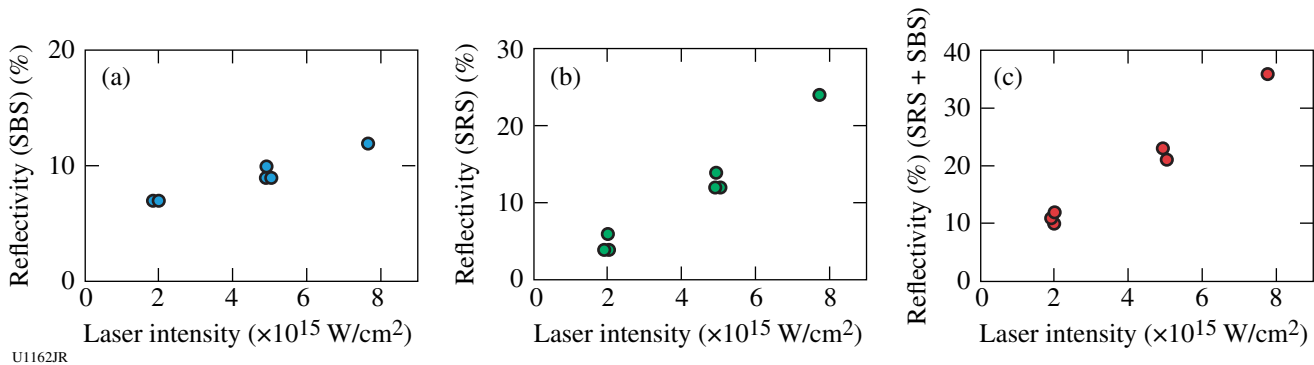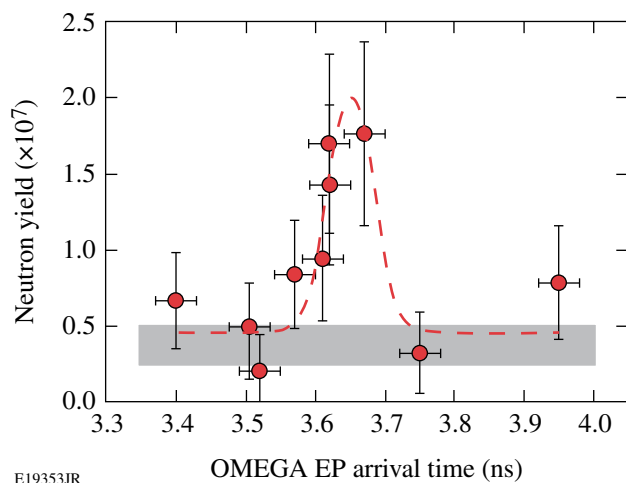
U1162JR

Figure 124.119
Measured backscattered light versus laser intensity for (a) SBS, (b) SRS, and (c) the sum of SBS and SRS.
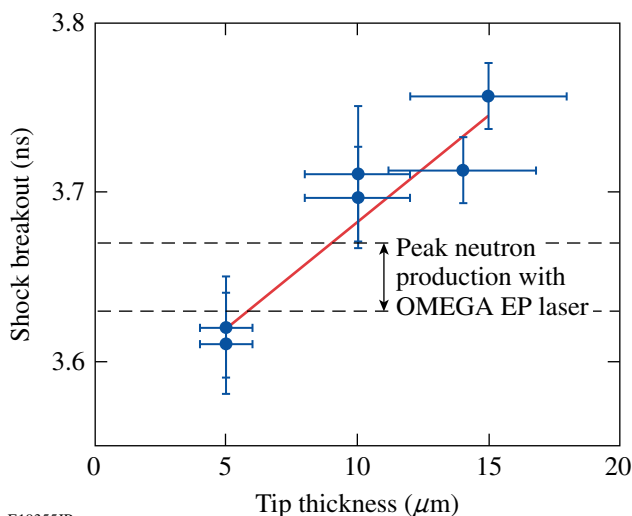
Figure 124.120
Measured neutron yield as a function of the arrival time of the short-pulse laser. The gray bar marks the yield without a heating beam. The dashed curve is a fit of a Gaussian profile to the integrated shot data.

compared to other experiments. A possible explanation is the formation of a pre-plasma in the cone. A pre-plasma in hollow cones has been shown in other experiments to strongly affect the ultra-intense laser–plasma interaction.

Shock-breakout measurements were performed by imploding cone-shell targets with various tip thicknesses without a short-pulse beam. VISAR and SOP diagnostics measured the time when optical emission appeared inside the cone. Figure 124.121 shows the time of shock breakout as a function

Figure 124.121
Measured breakout time of the shock inside the hollow Au cones. The shock breakout is later for thicker cone tips.

of tip thickness. With increasing tip thickness, the breakout is delayed. For thicknesses of 10 and 15 μm, the shock breakout time was at 3.70±0.03 ns and 3.74±0.03 ns, respectively. Shock breakout appeared 50 to 100 ps after the peak of neutron production, confirming that the cone tip was intact at the time when the OMEGA EP beam interacted with the target.

FY10 LLNL OMEGA Experimental Programs
In FY10, LLNL conducted several campaigns on the OMEGA and OMEGA EP Laser Systems, as well as campaigns that used the OMEGA and OMEGA EP beams jointly. Overall, LLNL led 376 target shots involving OMEGA and 107 target shots involving OMEGA EP. Approximately 50% of the total number of shots (212 OMEGA shots, 31 OMEGA EP shots) supported the National Ignition Campaign (NIC). The remainder were dedicated to experiments for high-energy-density (HED) physics (164 OMEGA shots, 64 OMEGA EP shots).

Objectives of the LLNL-led NIC campaigns at OMEGA included

- *Reactivation of the 4ω Thomson-scattering diagnostic*
- *Study of bremsstrahlung backlighters for Compton radiography of inertial confinement fusion (ICF) implosions*
- *High-resolution measurements of velocity nonuniformities created by microscopic perturbations in NIF ablator materials*
- *Equation-of-state measurements of Ge-doped CH*
- *Validation of the Compton-radiography diagnostic platform for ICF experiments*
- *Experiments to study the physical properties (thermal conductivity) of shocked-fusion fuels*
- *Characterization of hard x-ray sensitivity of MCP-based gated imagers*
- *Characterization of the plasma conditions at the laser entrance hole (LEH) of a gas-filled hohlraum using Thomson scattering*
- *Validation of the modeling of multibeam scattering occurring in NIC targets*
- *Measurement of the plasma conductivity by means of collective x-ray Thomson scattering*

The LLNL-led HED campaigns covered five main areas of research:

1. *Material dynamics and equation of state*
   a. *Quasi-isentropic compression experiments (ICE) for material properties such as strength, equation of state, phase, and phase-transition kinetics under high pressure*
   b. *Platform development using radiographic mea-*

surements of instability growth in tantalum to infer material strength using the joint OMEGA–OMEGA EP configuration

 c. *Properties of shocked CH and Si aerogel foams used in high-energy-density experiments*

 d. *The equation-of-state of a CO_2 mixture along the Hugoniot*

 e. *Initial experiments to develop an experimental platform to measure the melt and resolidification of tin*

2. *Opacity*

 a. *Opacity studies of high-temperature plasmas under LTE conditions*

 b. *Initial experiments to compare short- and long-pulse techniques to heat materials to high temperature for opacity data*

3. *Hydrodynamics*

 a. *Measurements of the Kelvin–Helmholtz instability in laser-driven shock tubes*

 b. *The hydrodynamic evolution of high-mach-number copper-foam jets*

4. *X-ray source applications*

 a. *Development of multi-keV x-ray sources for radiography and for the study of material response in samples*

5. *Diagnostic technique development*

 a. *Development of a target-mounted turning mirror for use with the VISAR diagnostic*

 b. *Demonstration of ultrafast temperature and density measurements with x-ray Thomson scattering from short-pulse-laser–heated matter*

 c. *Comparison of short- and long-pulse–generated x-ray backlighters*

 d. *Development of diffraction (white-light Laue and powder) to measure the structure of solids (Ta, Fe, Sn)*

1. National Ignition Campaign Experiments

4ω Thomson-Scattering Reactivation: The 4ω Thomson-scattering diagnostic was reactivated using a half-day of laser time on OMEGA. The diagnostic has been redesigned to measure the high- and low-frequency Thomson-scattered features. Figure 124.122 shows the first measurement of Thomson scattering from the electron-plasma wave resonance using a 4ω probe beam. The Thomson-scattering probe beam was aligned 400 μm off the surface of a vanadium foil target. The target was heated with a single 3ω beam, and the 4ω probe beam was delayed from the heater beam by 1 ns.

The wavelength of the Thomson-scattered electron feature shown in Fig. 124.122 can be used to measure both the electron temperature and density. The density is decreasing in time

because of the expansion of the blowoff plasma, which can be seen in the increasing wavelength of the blue-shifted electron feature.
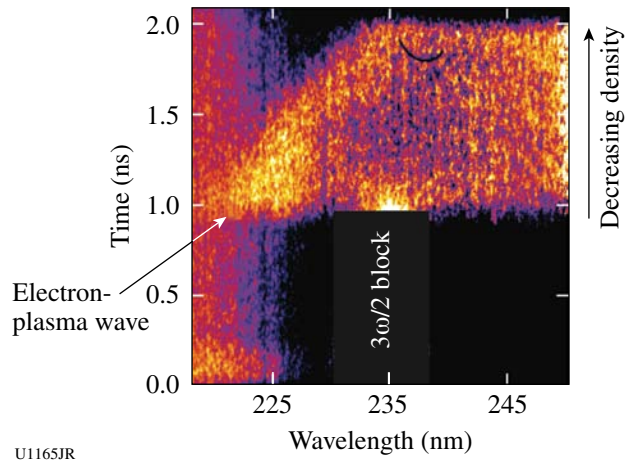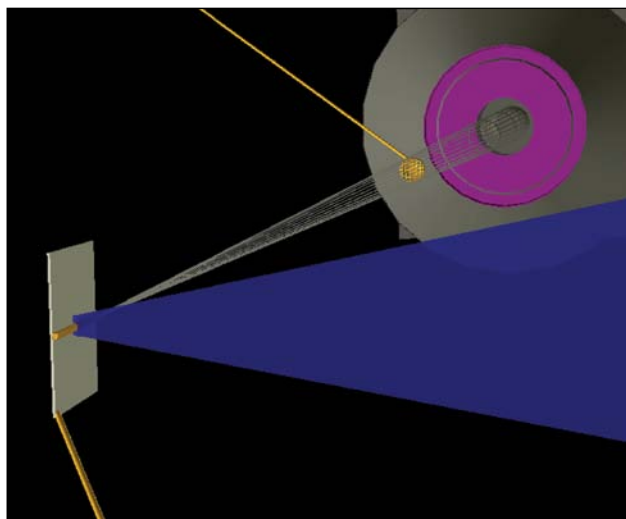

Figure 124.122
Thomson scattering from the electron-plasma wave resonance.

High-Resolution Bremsstrahlung Backlighters: The motivation of the bremsstrahlung backlighters campaign is to develop and characterize broadband x-ray sources emitting around and above 75 keV to be used in the Compton radiography of ICF targets. In FY09, Au microwire backlighters irradiated by 10-ps-long OMEGA EP pulses were characterized.

In FY10, Au microwire backlighters irradiated by 100-ps-long OMEGA EP pulses (1ω) and OMEGA pulses (3ω) were characterized with the primary goal of measuring the effect of longer laser pulse widths on backlighter source size.

As backlighters, 10-μm-diam, 300-μm-long Au wires were used on a CH substrate in a point-projection, end-on geometry. The bremsstrahlung radiation was generated by irradiating the Au wires with either the OMEGA EP short-pulse beam, delivering up to 1000 J in 100 ps (1ω), or six OMEGA short-pulse beams, delivering a total of 250 J in 100 ps (3ω).

Solid W spheres with diameters of 200 μm and 250 μm located 10 mm from the backlighters were used as radiography samples (Figs. 124.123 and 124.124). The Compton radiography snout was used to record the radiographs and measure the backlighter spectra. A combination of high- and low-Z filters was used inside the snout to restrict the backlit photon energies to above 75 keV. A Fuji BAS imaging plate, placed at 400 mm from the backlighter, was used as a detector. An analysis of the radiographs of the W sphere allows one to reconstruct

U1166JR

Figure 124.123
Geometry used in the OMEGA EP target chamber to obtain 2-D radiographs of W spheres at photon energies above 75 keV. The short-pulse beam drives an Au microwire on a low-Z substrate.
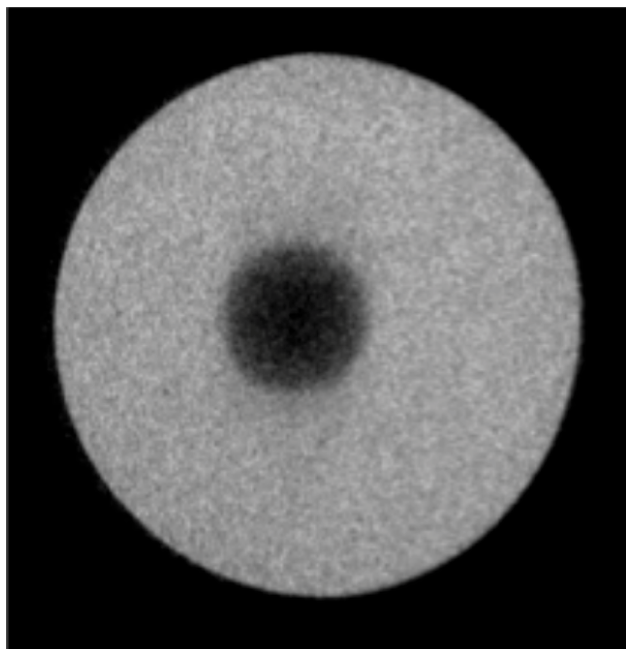

U1167JR

Figure 124.124
Point-projection radiograph of 200-μm-diam W sphere using 10-μm-diam Au microwire and six OMEGA beams (1ω, 40 J/beam/100 ps). The spatial resolution was ~10 μm.

the source size of the backlights. No significant difference was found between 10-ps and 100-ps OMEGA EP–produced x-ray backlighter (1ω) and 100-ps OMEGA-produced x-ray

backlighter (3ω). In all cases, source sizes between 10 μm and 12 μm were measured. For the experiments performed in the OMEGA EP target chamber, the ultrafast x-ray streak camera was deployed, which provided durations of the soft x-ray emission from the Au microwires of ~12 ps and 80 ps for backlighters produced by 10-ps and 100-ps OMEGA EP pulses, respectively. First results show that the hard x-ray conversion efficiency of the lower-intensity 3ω probe is 10 to 20× less than the 1ω probe, as expected (Fig. 124.125). These results pave the way for the implementation of Compton radiography on the NIF, using relatively long pulses and 3ω laser irradiation for the backlighters.
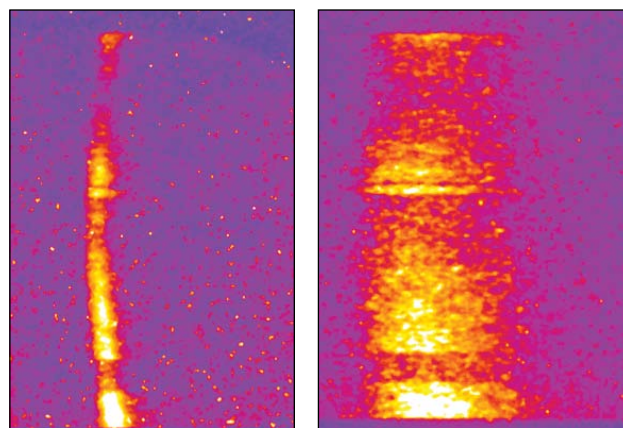
U1168JR

Figure 124.125
An analysis of the streaked images shows pulse durations of the soft x-ray emission from the Au microwires of 12 ps (FWHM), when irradiated by 1 kJ/10-ps (left), and 80 ps, when irradiated by 1 kJ/100-ps (right) OMEGA EP pulses.

High-Resolution Measurements of Velocity Nonuniformities Created by Microscopic Perturbations in NIF Ablator Materials: Two FY10 CapSeed campaigns took place in January and March. The primary goals of these campaigns were to produce a survey of clean CH samples, to complete the studies of Be ablator samples, and to continue the survey of diamond samples near the melt curve, including the first 2-D velocity measurements of shock fronts propagated through single-crystal diamond samples. An upgrade to the OHRV diagnostic incorporated vacuum boxes around the interferometers to improve the noise performance of the instrument. The experimental campaigns produced preliminary data on CH, although the data collection was impeded by a pair of previously unencountered problems. During the first campaign, inadequate antireflection coatings on many of the targets degraded the data quality to an extent that required that the measurements be repeated. On the second campaign, unconverted light affected the package

more than during previous campaigns, owing to a minor design change. Better quality control on the antireflection coatings solved the first problem, and a new shield design to mitigate the unconverted light issue has already been tested successfully (on a later non-CapSeed campaign). The study of the Be ablators was completed during these campaigns, with the new data confirming results that had been achieved previously. A highlight of the CapSeed-10B campaign was the observation that the shock front of an ~500-GPa shock front in a single-crystal diamond sample (below melt) was highly roughened (Fig. 124.126), equivalent to previous observations on poly-

U1169JR

Figure 124.126
Two-dimensional velocity fluctuations over a $100 \times 100 \ \mu m^2$ region of a ~500-GPa shock front traveling through a single-crystal diamond sample with $\langle 100 \rangle$ orientation.

crystalline diamond, suggesting, as a result, that the processes leading to the roughening are an intrinsic property of diamond.

Equation-of-State Measurements of Ge-doped CH: Knowledge of the EOS of NIF ablator materials is important for correctly predicting shock timing in an implosion. Plastic ablators in current NIF capsules are composed of layers of pure and Ge-doped $CH_{1.3}$. Recent shock Hugoniot measurements on both CH and CH_2 showed good agreement with models between 1 to 10 Mbar, providing confidence in the EOS for undoped plastic. In FY10, new shock Hugoniot measurements were performed on Ge-doped $CH_{1.3}$. Using impedance matching to a SiO_2 standard, the pressure and density of several samples doped with between 0.5 and 0.7 atm% Ge were measured. These data, supplemented by additional data from LLE shots, are shown in Fig. 124.127. From 1 to 6 Mbar, the data are in good agreement with LEOS 5315 (0.5% Ge) and LEOS 5315 (0.2% Ge)—models currently being used in simulations of NIF implosions—but are less compressible than these models at higher pressures (for comparison, two models for pure CH, *SESAME* 7592 and LEOS 5310 are shown). Although it is unclear why there is a tendency toward stiffer behavior above 6 Mbar, the agreement in the 2- to 3-Mbar range corresponding to NIF first shocks justifies the use of these EOS tables in current simulations.

Compton Radiography: The goal of the Compton radiography campaign is to build a novel diagnostic platform for ICF to characterize the shape and density of the fuel in ICF implosions. After the successful demonstration of Compton radiography of implosions in FY09, it was applied to three kinds of implosions in FY10.
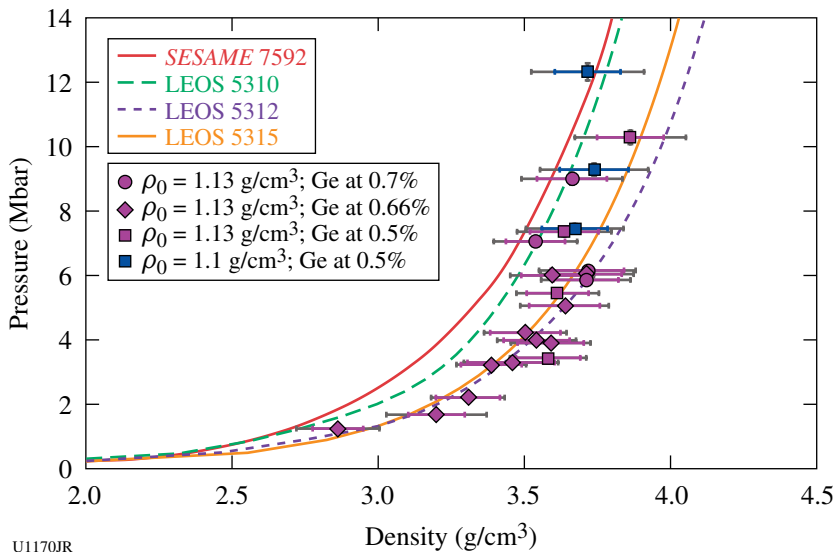

U1170JR

Figure 124.127
Summary of shock-Hugoniot measurements on Ge-doped $CH_{1.3}$.

In the first experiment, 60 beams of OMEGA were used to directly drive implosions of 40-μm-thick, 870-μm-diam CH capsules filled with 8 atm of D_2 gas, located at OMEGA's target chamber center. A 10-μm-diam, 300-μm-long Au wire was used as a backlighter in a point-projection, end-on geometry 10 mm from the CH shell. The backlighter was driven by the OMEGA EP short-pulse beam, delivering ~1 kJ at 10 ps in a 100-μm square spot size.

The time delay between the OMEGA EP short pulse and the OMEGA laser pulses was varied to bracket the peak compression time predicted by *LILAC* 1-D simulations. As an example, Fig. 124.128 shows a radiograph of the imploding CH shell, near peak compression, obtained at a photon energy of ~100 keV, where Compton effects dominate the fuel opacity. The radiograph, having about 10-ps and 10-μm temporal and spatial resolution, respectively, shows a limb-darkened shell of about 90-μm diameter.
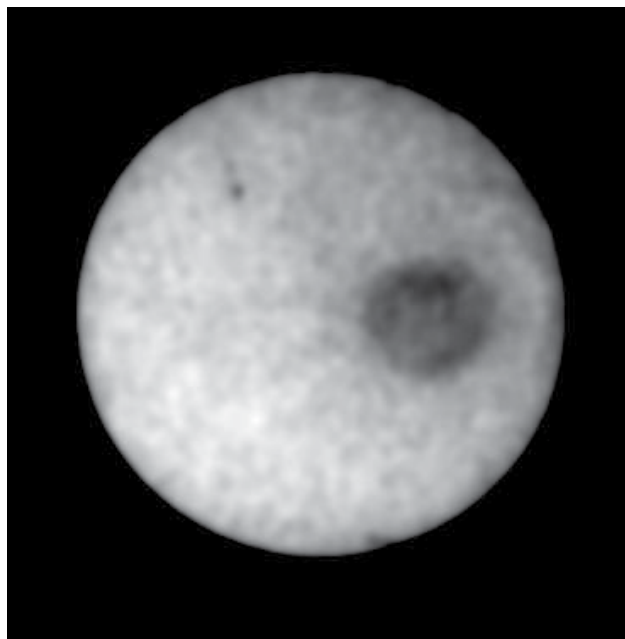
U1171JR

Figure 124.128
Compton radiograph of an 870-μm-diam CH capsule filled with 8 atm of D_2, near peak compression. The radiograph has been recorded at an effective photon energy $\langle h\nu \rangle \sim 100$ keV, where Compton effects dominate the fuel opacity. The radiograph shows an object about 90 μm in diameter inside the shadow of the Compton radiography snout collimator.

In a second experiment, at photon energies $\langle h\nu \rangle \sim 70$ keV, radiographs were successfully recorded of 54 OMEGA beam direct-drive implosions of cone-in empty CD shells and 60 OMEGA beam direct-drive implosions of empty CD shells,

without cones. Again, the Au microwire backlighters, with 10-ps and 10-μm temporal and spatial resolution, respectively, were driven by the OMEGA EP short-pulse beam, delivering ~750 J at 10 ps in a 100-μm square spot size. The radiographs of cone-in-shell implosions show the shell near peak compression, at a distance of 50 μm and with a diameter of about 50 μm. A third experiment was dedicated to recording Compton radiographs of cryogenic direct-drive implosions. This effort is a work in progress since the experimental setup imposes very tight tolerances on the alignment of the target and back-lighter and relies on an improvement of the cryogenic-target alignment system. The CompRad campaigns fully validated a novel diagnostic technique, Compton radiography, which will be extremely useful when implemented on NIF implosions.

Conductivity of D_2 and CH: The thermal-transport proper-ties of D_2 and CH at high densities have important implications for the stability of ICF implosions. The OMEGA laser was used to prepare off-Hugoniot states of these materials using multishock compression. Pressure, density, temperature, and optical properties of the compressed materials were determined by simultaneous VISAR and SOP measurements (Fig. 124.129). D_2 states up to 10 Mbar and 3 g/cc have been achieved at temperatures below 1 eV. CH states up to 8 Mbar and 4.5 g/cc have been achieved at temperatures near 3 eV. A Drude-like model was used to infer band-gap closure and electrical and thermal conductivities from the optical behavior at different states. Preliminary results indicate that D_2 thermal conductivity at such high-density, low-temperature states may be well below theoretical predictions.

Characterization of Hard X-Ray Sensitivity of MCP-Based Gated Imagers: An MCP-based gated x-ray imager is one of the most important diagnostics of the NIC. In FY09, the neutron-induced background of the MCP-based x-ray imagers with a CCD (Kodak KA-16801E) and a photographic-film readout (TMAX 3200) was characterized on OMEGA high-neutron-yield shots.[41] In FY10, a new MCP-based x-ray framing camera, radiation hardened gated x-ray imager (hGXI) was assembled, and its x-ray sensitivity was tested at the Omega Laser Facility.

To optimize experimental setup of NIF implosion experi-ments, it is crucial to know the absolute sensitivity of the gated x-ray imager for 10- to 20-keV x rays. To test x-ray sensitivity in this energy region, calibration experiments were performed on OMEGA.

A Au-coated spherical target (1.015-mm diameter) was irra-diated by 60 laser beams (UV, 500 J/beam, 1-ns square pulse).
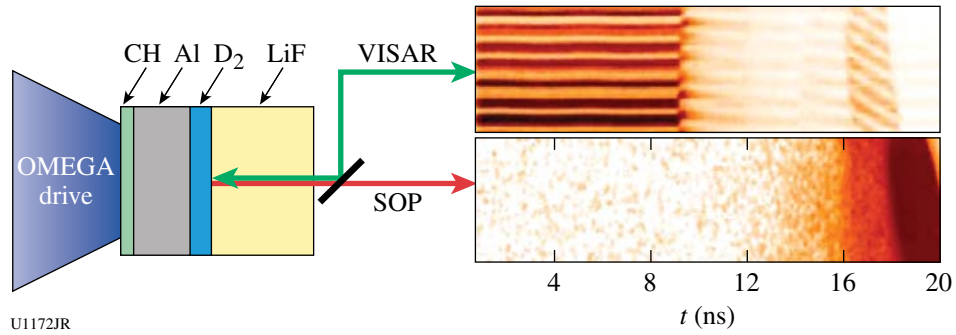
Figure 124.129

A sequence of three OMEGA laser–driven shocks was sent into a thin layer of liquid D_2 trapped between an Al pusher and a LiF window. For the states reached in this experiment, the LiF remained transparent, and the VISAR and SOP records tracked the velocity, reflectance, and optical emission of the D_2–LiF inter-face. A dramatic increase in the D_2 reflectance was observed upon the arrival of the third shock at this interface (at ~16 ns), corresponding to a large increase in the conductivity. The three shocks coalesce in the LiF at about 18 ns, increasing the LiF temperature and ending its transparency.

The laser intensity on the sphere was 1.2×10^{15} W/cm^2. Absolute x-ray emission spectrum was recorded by x-ray spectrometers (HENWAY and DCS). To compare relative sensitivities, three different gated x-ray imagers (hGXI, XRFC1, XRFC3) were located 1600 mm from the target chamber center. In front of the MCP, a 2.5-mm-thick–polyimide, 0.6-mm-thick–Al filter was used to cut off a low-energy component (<7 keV) and attenuate the x-ray fluence. Figure 124.130 shows estimated x-ray production on the target and spectrum through the filters. The estimated x-ray flux on the MCP is 2.5 to 5 kW/cm^2. Fig-ure 124.131 shows images obtained with this experiment. The signal intensity obtained by those cameras (hGXI: OD = 1.97, 193 merg/cm^2; XRFC1: 1250 ADU/pix; XRFC3: 1750 ADU/pix) was consistent with our numerical model. Those numbers will be used to benchmark the MCP model.

Plasma Characterization of the LEH Region of Gas-Filled Hohlraums: The objective of this campaign was to character-ize the plasma conditions at the laser entrance hole (LEH) of a gas-filled hohlraum using Thomson scattering. This region is of special interest for crossed-beam energy transfer, which is a process that can transfer a large percentage of laser energy between beam cones. The energy transfer is governed by the

electron temperature, plasma-flow velocity, and laser-beam wavelength. Thomson-scattering measurements from the ion feature were made for a series of hohlraums with LEH diam-eters of 800, 1000, and 1200 μm (Fig. 124.132).
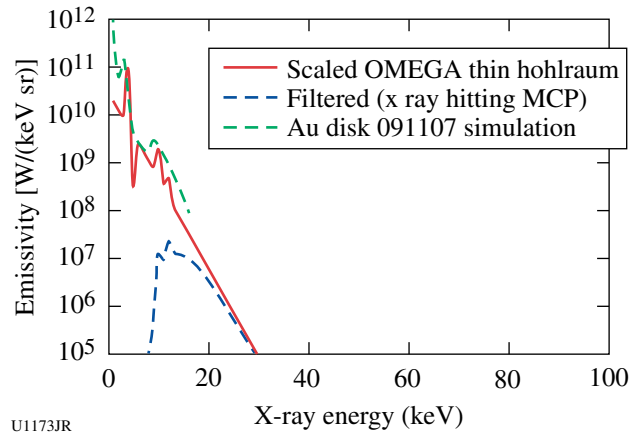
Figure 124.130

X-ray production and spectrum from the Au sphere. X-ray conversion effi-ciency was estimated by a radiation–hydrodynamic simulation and extrapolat-ing x-ray spectra of previous experiments.
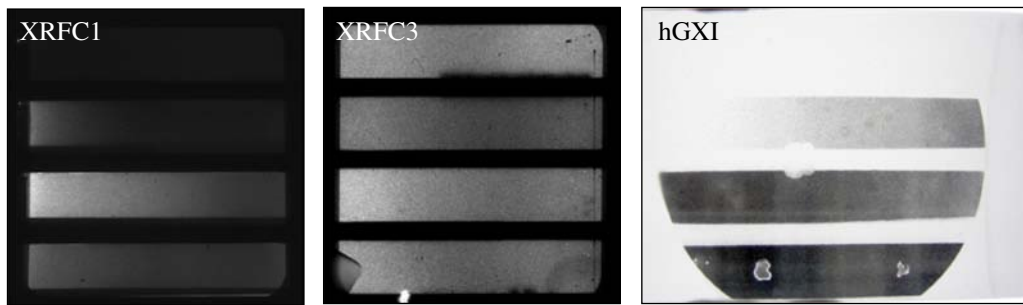
Figure 124.131

Images obtained on a flat-field-ing experiment from three dif-ferent x-ray imaging systems: XRFC1, XRFC3, and hGXI.
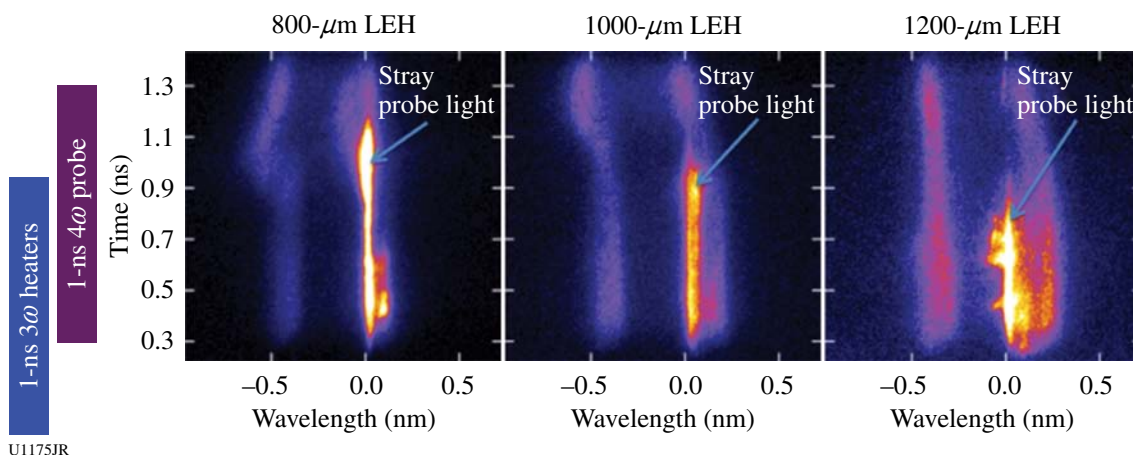
Figure 124.132
Thomson-scattering measurements of the LEH region of a gas-filled hohlraum.

The Thomson-scattering measurements are compared to hydrodynamic simulations using the code *HYDRA* in Fig. 124.133. The plasma-flow velocity is shown for three different locations along the simulation hohlraum axis. Large gradients in this region are predicted by the modeling. The measured electron temperature and flow velocity will be used to benchmark different heat-transport models.
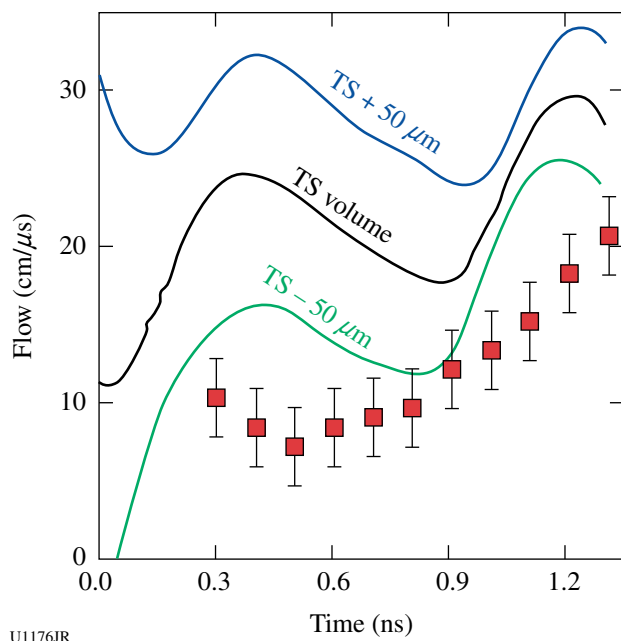

Figure 124.133
The experimental measurements (red squares) are compared to hydrodynamic simulations at different locations outside the LEH.

Validation of the Modeling of Multibeam Scattering Occurring in NIC Targets: A series of experiments was carried out to verify a critical component of the model of backscatter from the multiple NIC beams that indicates that backscatter from the interior of the hohlraum can be amplified by each of the crossing beams it encounters as it exits the laser entrance hole. The model predicts that even with a small gain exponent from each of several crossing beams, the overall gain exponent and amplification produced by all the beams can be quite significant with the additive gain exponents of linear waves. The OMEGA experiments used a 3-μm-thick CH foil target illuminated with 28 heater beams to produce plasma conditions similar to what are found in NIC ignition targets and the Mach-1 flow velocity that is necessary to produce resonant amplification of a seed with the same wavelength as the pumps, as shown in Fig. 124.134.

Experiments were performed in which the transmission of a seed beam (B46) was measured in the case of no pump beam and one and two crossing pump beams (B30, B50); the transmitted power in each case is shown in Fig. 124.135.

Note that a single pump beam produces enhanced transmission relative to the no-pump case near 1.4 ns, as expected from the simulations of the resonance conditions, and a second pump beam produces an even greater increase in the power at a somewhat later time. These results were obtained at three different seed intensities, and similar amplifications were found in each case, consistent with a linear ion-acoustic wave response. Further experiments were carried out to demonstrate the control of energy and power transfer by the relative align-
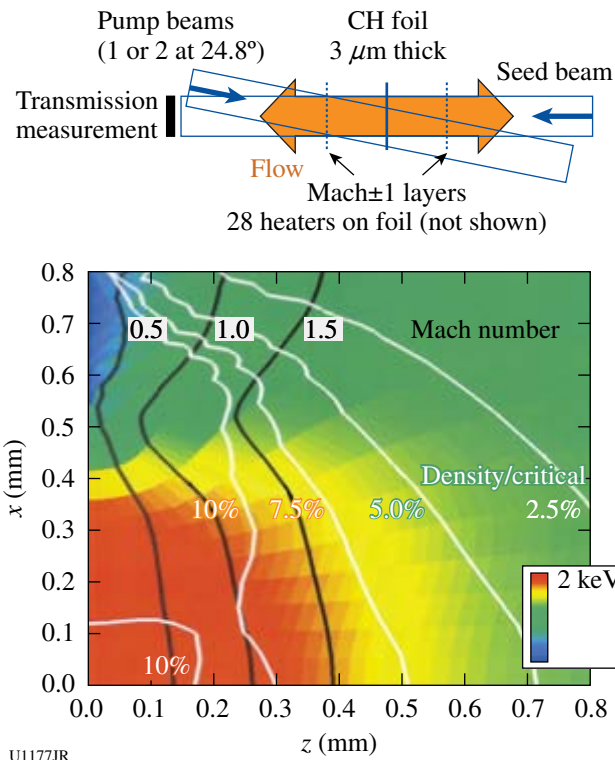
Figure 124.134
The experimental geometry of a foil target used to produce the plasma conditions and Mach-1 flow, shown at 1.4 ns, that is necessary for resonant amplification of a seed of 351-nm light representing the SBS backscatter produced in the interior of the NIC hohlraum.

ment of the polarization vectors of the pump and seed beam, as shown in Fig. 124.136.

To change the polarization, the half-wave plate, or polarization rotator, was installed in B50 and its polarization was rotated through 90° with respect to the seed-beam polarization. The experiments demonstrated greatest amplification when the polarizations were aligned, as determined from the energy-amplification factor measured in three experiments and shown in Fig. 124.136. The greatly reduced amplification when the polarization angle was near 90° demonstrates the importance of relative polarization in controlling this effect. This work has increased confidence in the modeling of multibeam scattering occurring in NIC targets.

Measurements of the Plasma Conductivity by Means of Collective X-Ray Thomson Scattering: The goal of this experiment was to measure the electron–ion collision frequency n_{ei} in isochorically heated Be from the broadening of plasmon signals measured with x-ray Thomson scattering.[42] The n_{ei} is directly related to the conductivity, which is an important
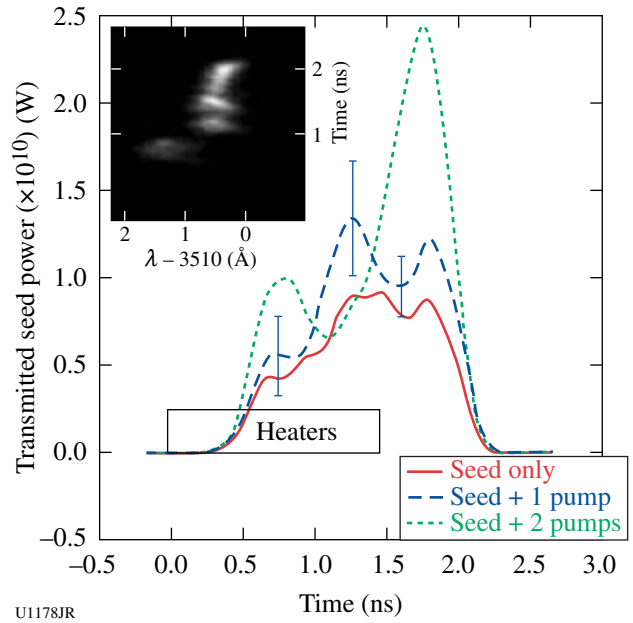
Figure 124.135
Streaked spectrum and transmitted power waveforms of the seed beam transiting the foil target plasma, for the cases of no amplifying pump and one and two amplifying pumps, showing enhancements in the seed power produced by energy transfer from the pumps to the seed beam.
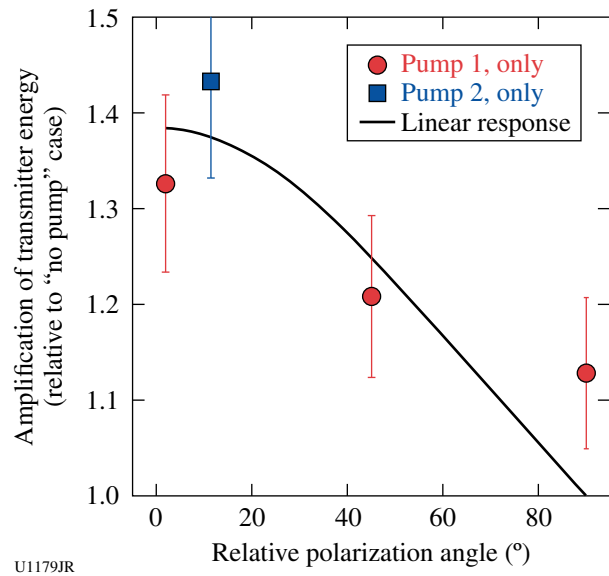
Figure 124.136
Energy-amplification factor produced by a single pump beam as a function of its polarization angle relative to the seed beam.

parameter to correctly model capsule implosions on the NIF; at the same time, it is known only with great uncertainty from theoretical predictions.

On this joint OMEGA–OMEGA EP shot day, the OMEGA EP beam (250 J in 10 ps) was used to isochorically heat a 200-μm Be cube to 35 eV, assuming 20% conversion efficiency into hot electrons ($T_{hot} \sim 200$ keV), as shown in Fig. 124.137(a). Since it is properly shielded, the Be's front surface, which gets much hotter, is not seen by the scattering experiment. The size of the gold shields was chosen such that plasma moving around the shield and still emitting line radiation would be imaged to the detector well separated from the scattering signal. This is important because gated detectors cannot be used in this short-pulse environment. Fourteen OMEGA beams at 3ω drive irradiated a 12-μm-thick Saran foil to create the Cl Ly$_\alpha$ probe line at 2.96 keV. A pulse width of 200 ps was chosen to achieve an adequate time resolution of the scattering experiment. Radiation–hydrodynamic simulations show that at temperatures of a few 10 eV, the Be cube does not disintegrate within the first 750 ps. The scattering angle was at 30° to ensure a large collectivity parameter $\alpha \sim 1.7$, necessary to observe plasmon broadening caused by collisions.

To measure the scattering spectrum, a new high-efficiency von-Hamos geometry Bragg crystal spectrometer was developed using a cylindrical curved HOPG crystal [see Fig. 124.137(b)]. The signal was recorded on image plates. The CLVH spectrometer was successfully fielded for the first time on this shot day. For cross-calibration, and as source monitors, the Cl K-shell emission was monitored with the GTS and XRS1 spectrometers, operated with image plates, and with SSCA on the OMEGA-only shots.

A total of nine shots were taken, including three joint shots at full energy, two OMEGA EP–only shots, and four OMEGA-only shots. On the low-energy qualification shot of the OMEGA EP beam, the emission from an Au-coated CH sphere was used to measure the timing between the OMEGA and OMEGA EP lasers and to establish a 400-ps delay of the OMEGA probe beams with respect to the OMEGA EP beam. During the day, conditions used to create the x-ray probe were varied. On most of the targets, the Saran foil had a 30-μm
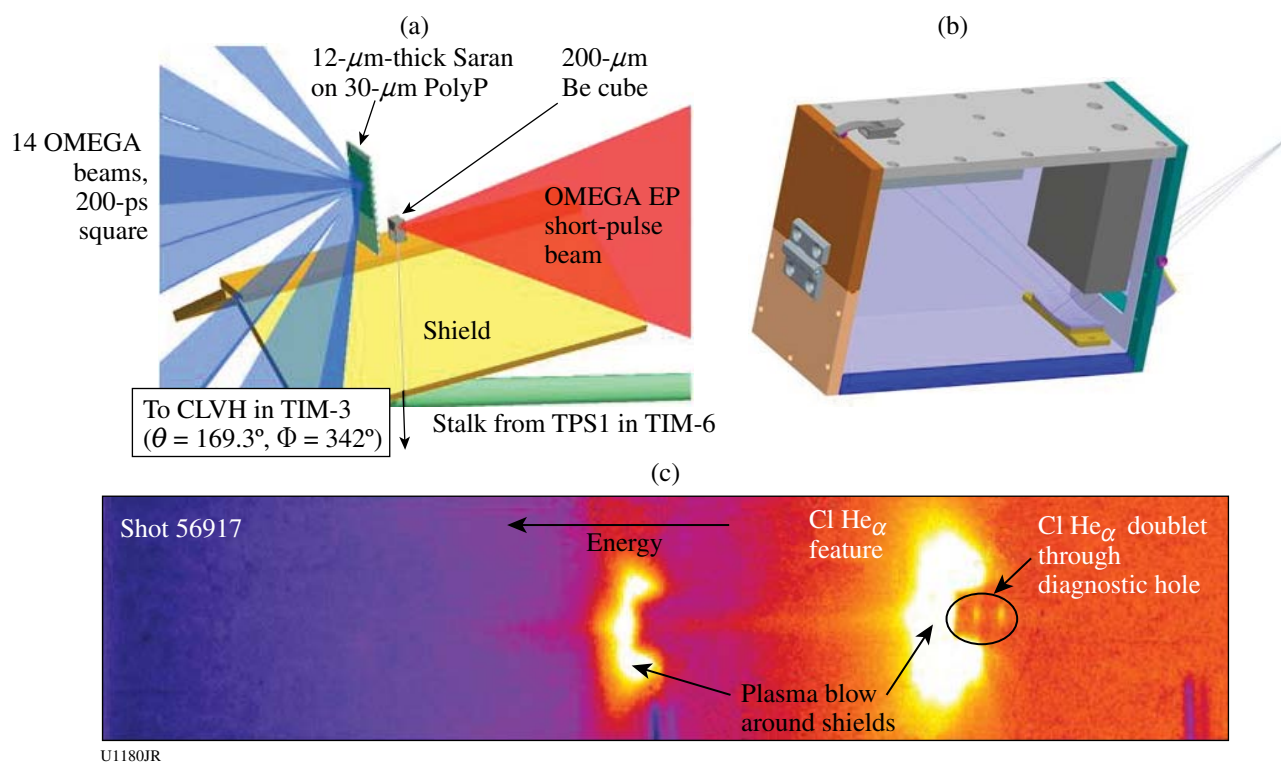

Figure 124.137
(a) Experimental setup to isochorically heat a 200-μm Be cube and characterize the plasma conditions with x-ray Thomson scattering using the Cl Ly$_\alpha$ line at 2.96 keV. (b) The CLVH spectrometer, utilizing a cylindrically curved HOPG crystal in von-Hamos geometry to achieve high detection efficiency, was developed for this campaign and successfully fielded for the first time. (c) Data from CLVH.

polypropylene backing to prevent Cl-containing plasma from moving into the line of sight of the CLVH spectrometer above the Be cube and obscuring the scattering signal. In combination with the low backlighter drive energy (~1 kJ in 0.2 ns compared to ~7.5 kJ in 1 ns for other XRTS platforms), it was not possible to observe a scattering signal. The strongest signal was obtained for a target that had no polypropylene backing, and the OMEGA pulse length was increased to 600 ps, as shown in Fig. 124.137(c).

The most prominent features are due to Cl He$_\alpha$ and Cl Ly$_\alpha$ emission from plasma that was moving around the shields. In the nondispersive axis the spectrometer was imaging with M = 1, and the extension of the shields of ~±3 mm from the center axis can clearly be seen. X-ray emission from the direction of the Be cube at TCC was imaged to the central axis. Clearly, a weak bremsstrahlung signal and the He$_\alpha$ doublet can be identified originating from that direction.

2. High-Energy-Density Experiments
Material Dynamics and Equation of State
Iron equation of state: Ramp compression of Fe to 300 GPa. The preliminary design for a ramp-compression experiment on Fe up to 300 GPa is shown in the upper right image in Fig. 124.138, along with the ramp laser pulse shape as calculated by a radiation–hydrodynamics code (lower right). The ramped laser pulse shape for the 36 beams focused onto the inner walls of the hohlraum results in a time dependence in the radiation temperature, and subsequently a ramp-compression wave is launched into the stepped Fe sample. The raw VISAR data and the extracted free-surface velocity U_{fs} versus time profiles for 25.5/21.9/38-μm-thick Fe samples are shown on the left in Fig. 124.138.

The $U_{fs}(t)$ profiles reveal a strong rate dependence associated with the $\alpha \longrightarrow \varepsilon$ structural phase transformation. The equilibrium pressure for this transformation as measured in
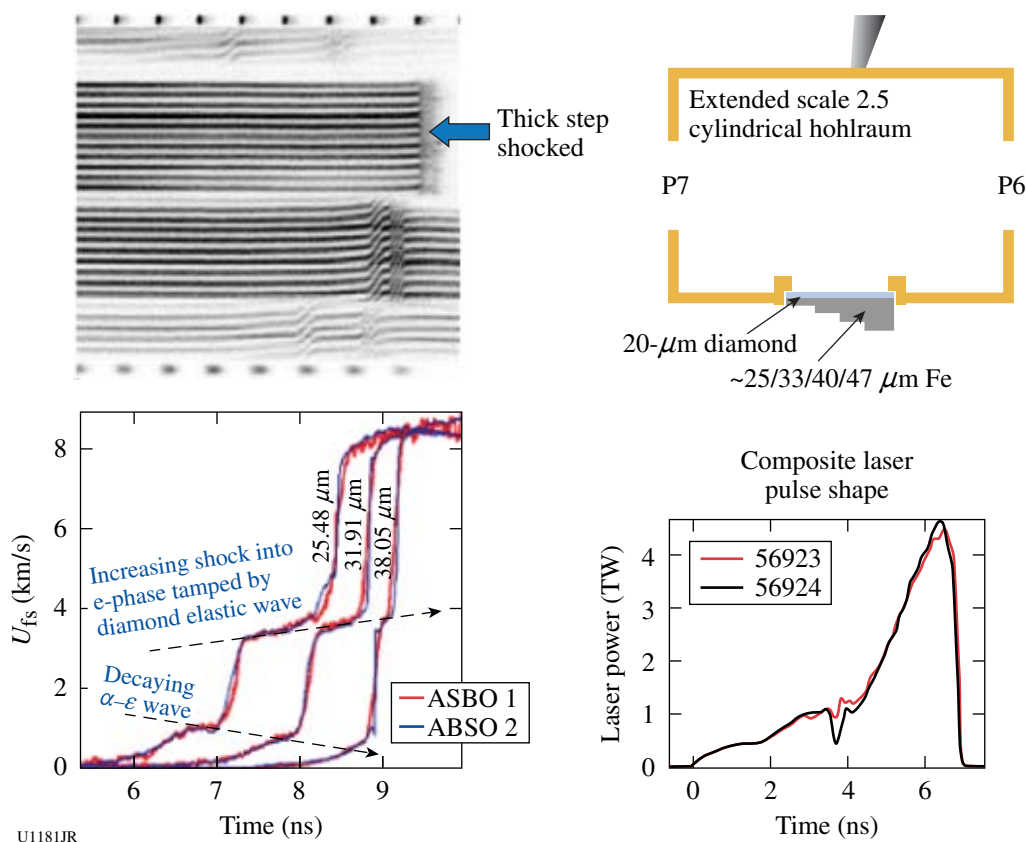
Figure 124.138
Preliminary attempts to ramp compress multistepped Fe samples to a peak stress of ~300 GPa were successful. However, strong time dependence was observed associated with compression across the $\alpha \to \varepsilon$ phase boundary.

shock-compression experiments with millimeter-thick samples is 13 GPa. The measured pressure, however, for the $\alpha \longrightarrow \varepsilon$ phase transformation in these experiments for thin samples and high strain rates is ~20 GPa. This strong time dependence compromises the extraction of stress-density data using the standard ramp-compression analysis techniques. To overcome this difficulty, subsequent experiments have been designed such that a steady initial ~70-GPa shock is launched into the stepped Fe sample followed by subsequent ramp compression to ~300 to 400 GPa. This initial shock compresses directly into the ε phase by overdriving the $\alpha \longrightarrow \varepsilon$ phase transformation and therefore avoids the complications associated with the kinetics of this transformation. With the high-pressure ramp-compression platform developed during this period, compression of solid Fe to peak stresses of 300 GPa was demonstrated, and strong time dependence in the structural phase transformations was observed.

Boron ablator for quasi-isentropic compression experiments. The purpose of this campaign was to demonstrate the performance of B as an ablator. By measuring the shock-break times of a stepped reservoir, the ablation pressure created by the ablator material was deduced. The data matched well with the LASNEX simulation with an ablation pressure of 52 Mbar, which will be sufficient to create up to 5-Mbar pressure for the quasi-isentropic drive for the material-strength Rayleigh–Taylor experiments on the NIF.

Tantalum Rayleigh–Taylor experiments. The goal of the ICETaRT experiments is to measure the dynamic properties of solid-state Ta under high pressures (>1 Mbar) and high strain rates (10^6 to 10^8 s^{-1}) using the Rayleigh–Taylor (RT) instability. Quasi-isentropic high-pressure conditions were achieved by using a unique plasma piston configuration where

the sample materials stay well below the melting temperature while they are plastically deformed under high pressure, as shown in Fig. 124.139. The growth of the RT instability was measured in V[43] and Ta, and these data were used to compare with predictions using different material strength models. The amount of growth was measured by face-on radiography using laser-driven x-ray backlighters. High-energy backlighter x rays of 20 to 50 keV generated by the OMEGA EP beam were used to probe high-Z materials such as Ta.

The experiment was conducted in the main OMEGA chamber in the joint OMEGA/OMEGA EP shot configuration. A series of successful radiographs were obtained from these experiments. Figure 124.140(a) shows one example of a face-on, 22-keV x-ray radiograph of a rippled sample target of Ta at 60 ns after the initial laser pulse. The driven ripples constitute the circular central part of the image, while the upper portion of the image contains calibration features (stepped filters and knife-edge resolution block) to aid in the extraction of the growth factor. The ripple amplitudes were derived from transmission contrast between the peak and valley of the ripple regions. The initial growth-factor measurements are compared to several strength models in Fig. 124.140(b), including the new Ta multiscale model, which starts with a quantum mechanical interatomic potential and is based on the motion and multiplication of dislocations,[44] and the Preston–Tonks–Wallace (PTW) strength model.[45]

Experiments later in the year addressed the effect that grain size (Hall–Petch effect) had on the strength under these high-pressure and high-strain-rate conditions. While there are many measurements of the Hall–Petch effect at ambient conditions, where strength varies as (grain size)$^{-1/2}$ (Ref. 46), no previous theory or experimental measurements under high-

OMEGA EP

μ-flag backlighter

22-keV X rays
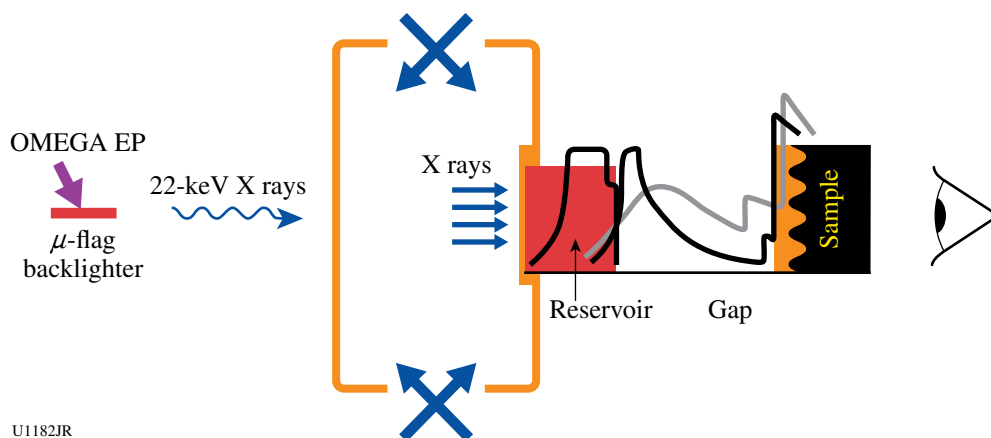
X rays

Reservoir   Gap

Sample

Figure 124.139
ICETaRT experiment configuration for an OMEGA/OMEGA EP joint shot.

U1182JR

pressure, high-strain-rate dynamic conditions existed. Three different types of targets were fabricated, with average grain sizes of 90, 15, and 0.25 μm, as shown in Fig. 124.141(a). The radiography data quality was very high, and useful data were obtained on all shots. The strength is inversely related to the RT growth factor, which is shown as a function of the average grain size in Fig. 124.141(b). Within the error bars of the data, no obvious Hall–Petch effect is observed. The data analysis is still in progress to understand the theoretical and physical implications of these results.

Equation of state of SiO$_2$ aerogel foam. The study of the EOS of low-density foams allows one to achieve states of matter with high temperatures at lower than solid density. These conditions appeal to a range of interest for high-energy-density science. Foams at different densities can be used in EOS experiments to study points along unloading isentropes, which allows one to study the material EOS of the Hugoniot. Foams also play an important role in laboratory-based astrophysical experiments like supercritical radiative shocks or simulate supernovae remnant formation. All of these uses for foams
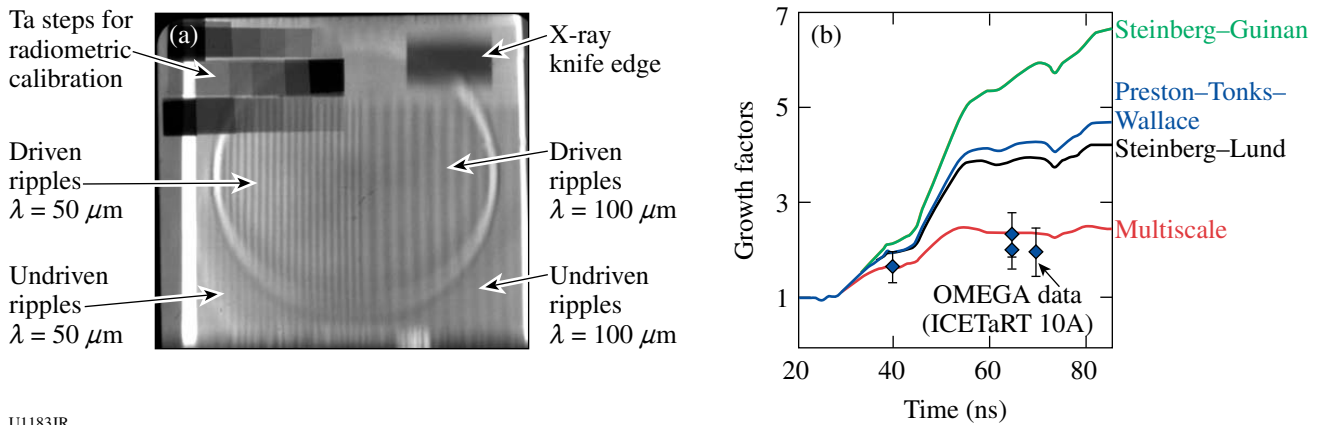
U1183JR

Figure 124.140
(a) Face-on 22-keV x-ray radiograph of a rippled sample target of Ta at 60 ns after the initial laser drive. The driven ripples constitute the center of the image, while the upper portion of the image contains added features (stepped filters and knife-edge resolution block) to aid in the extraction of the growth factor. The ripple amplitudes were derived from transmission contrast between the peak and valley of the ripple regions. (b) Comparison of various model predictions with growth-factor data. The data reach peak pressures between 1.2 and 1.4 Mbar and average strain rates around 2×10^7 s^{-1}.
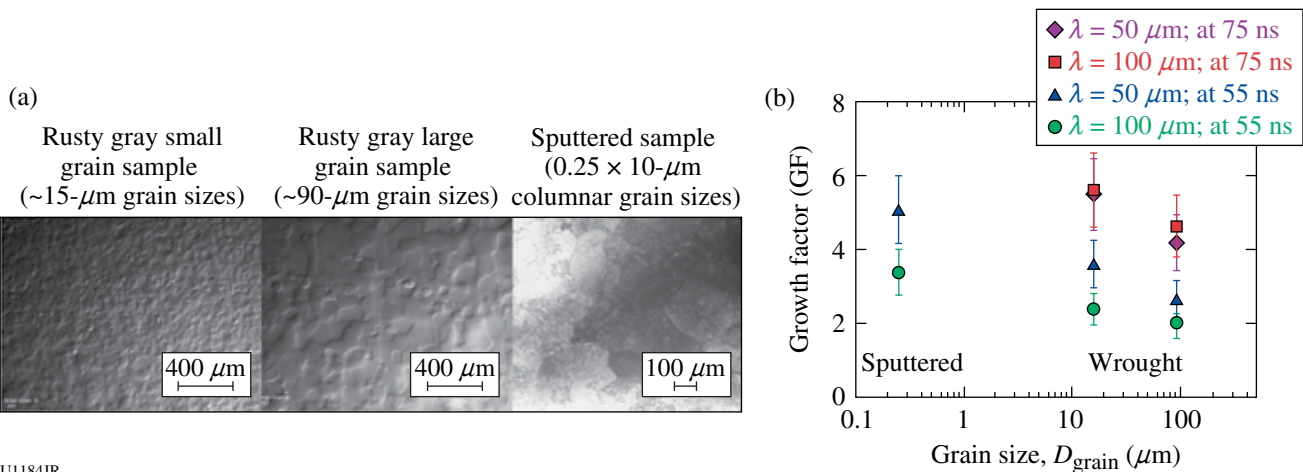
U1184JR

Figure 124.141
(a) SEM and TEM pictures of the different Ta grain-size samples. (b) Growth factor, which is sensitive to material strength, as a function of grain size. No obvious Hall–Petch effect is observed.

require a detailed understanding of the EOS of the foam itself. Unlike other material EOS studies, which vary pressure and temperature, the foam has an adjustable initial density that plays a key role in determining the material's behavior. In these experiments, the foam of interest, in this case 100 mg/cc of SiO_2 aerogel, was placed between two quartz plates, as shown in Fig. 124.142. A decaying shock wave was launched through one of the quartz plates, and the propagation of the reflecting shock front through the quartz and foam was followed by an optical VISAR system. In this system the known Hugoniot of the quartz was used with an impedance-matching model to determine the properties of the foam. Figure 124.143 is a plot of data taken over four shots at a single initial density. The large increase in density at low pressures was caused by the compaction of voids in the material at the higher shock pressures; the compaction of the voids causes heating and the majority of the pressure is due to thermal pressure.

<u>CH-foam shock-breakout experiment.</u> Understanding the behavior of foams in the presence of a strong shock is an ongoing effort at several institutions. A series of experiments were performed to investigate the material properties of a new foam material, dicyclopentadiene ($C_{10}H_{12}$), at a density of 40 mg/cc. The targets were configured as shown in Fig. 124.144, and were driven by 15 beams with a pulse length of 1 ns. Some targets were driven with a plastic (CH) ablator and an Al piston, while others used a Cu-foam piston (density 0.9 g/cc).

The primary diagnostic was VISAR, including the streaked optical pyrometer (SOP), which was used to measure the shock breakout. Data from these shots are shown in Fig. 124.145. The shock in the foam at full drive (5488 J) showed dramatic
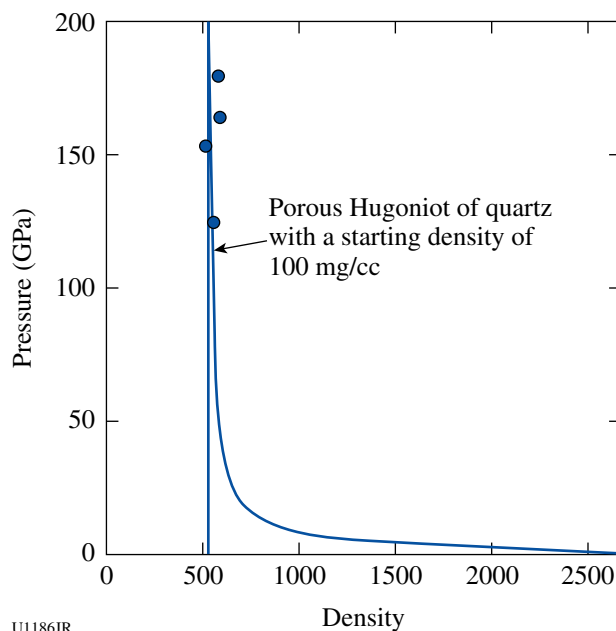
Figure 124.143
Plotting the pressure–density points compared to a model prediction of the shock Hugoniot of 100 mg/cc of SiO_2 aerogel.

evidence of preheat (presumed to be caused by drive x rays preheating the foam), although the shock in the quartz was measurable as may be seen in Fig. 124.145(a). With significantly reduced drive (3057 J), shock breakout from the foam was observed. See Fig. 124.145(b). This experimental series has been put on hold while the mechanical properties of the material for fabricating targets are being evaluated. These were the first targets fabricated from DCPD, and the material appears to have less rigidity than expected.
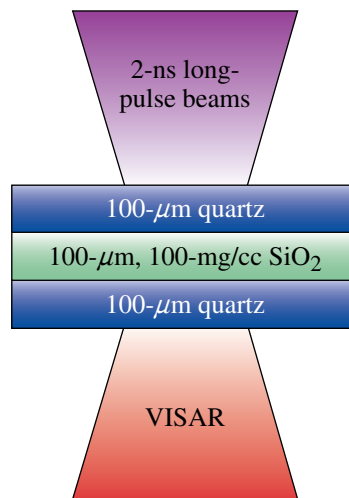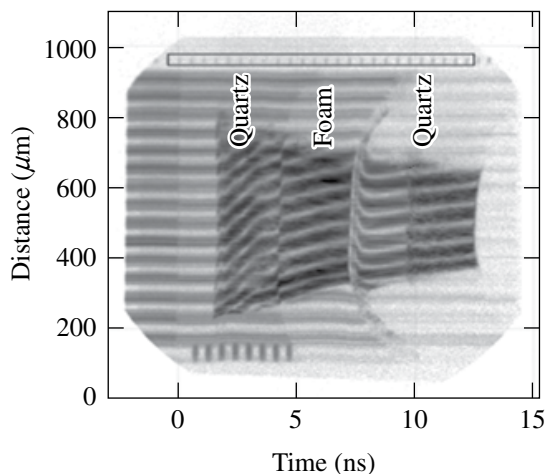

Figure 124.142
Target geometry and example data. The VISAR trace shown follows the shock wave through the quartz and 100 mg/cc of SiO_2 aerogel.
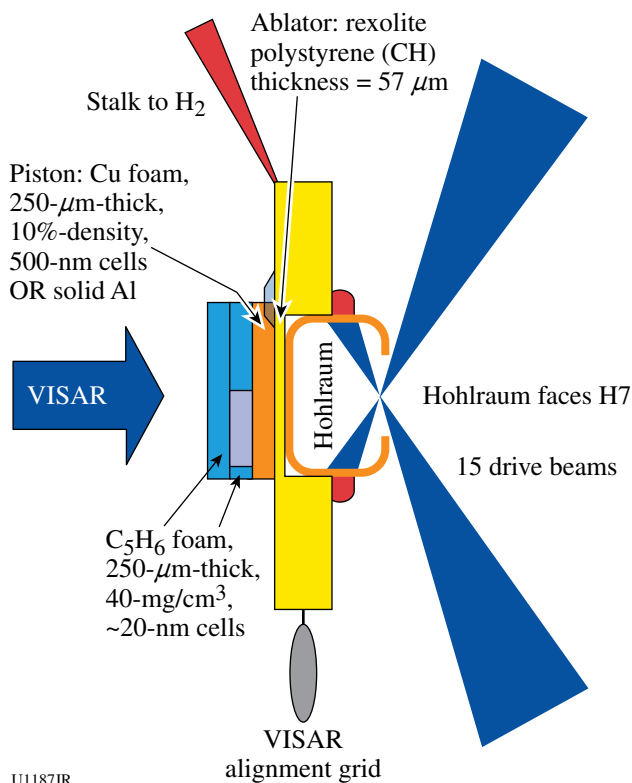
Figure 124.144
Target, laser, and diagnostic configuration for the CH-foam shock-break-out campaign.

<u>CO_2 Hugoniot measurements to 950 GPa.</u> CO_2 EOS, which is found in the core of giant planets, is of wide scientific interest. It is a mixture that challenges models to accurately predict. Prior experimental data were limited to below 100 GPa. Experimental measurement of the CO_2 Hugoniot was extended up to 950 GPa by launching shocks into CO_2 samples precompressed

in diamond anvil cells to ~0.5 GPa (see Fig. 124.146). VISAR and SOP measurements of the CO_2 shock front in comparison to concomitant measurements in quartz were used to infer pressure, density, reflectance, and temperature of shocked CO_2. CO_2-shock reflectance saturated at about 35% above 350 GPa, and the pressure, density, and temperature results are consistent with the theoretical LEOS table.

<u>Melt and resolidification in Sn.</u> This was the first set of experiments that investigated the use of velocimetry for exploring the melt line of Sn. The strategy was to develop a drive to shock-melt the tin and then ramp-compress it across the liquid–
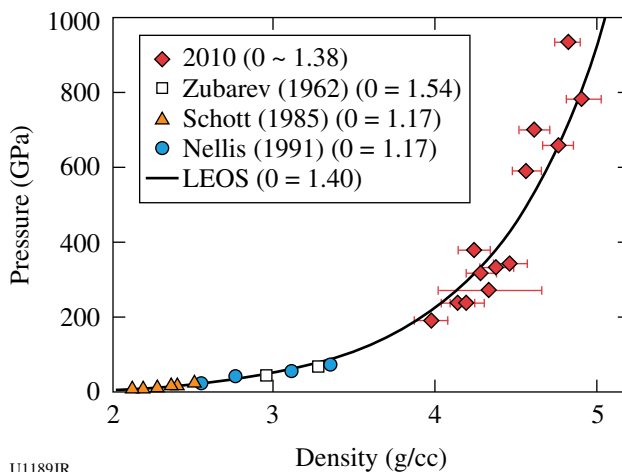
Figure 124.146
Previous experimental measurements of the CO_2 Hugoniot (open data points) reached 80 GPa. In FY10, the OMEGA laser was used to extend the range to 200 to 950 GPa (solid diamonds). The CO_2 shock pressure and density were inferred by shock-velocity measurements impedance matched to a SiO_2 standard, using the Hicks (2005) SiO_2 equation of state.[47]
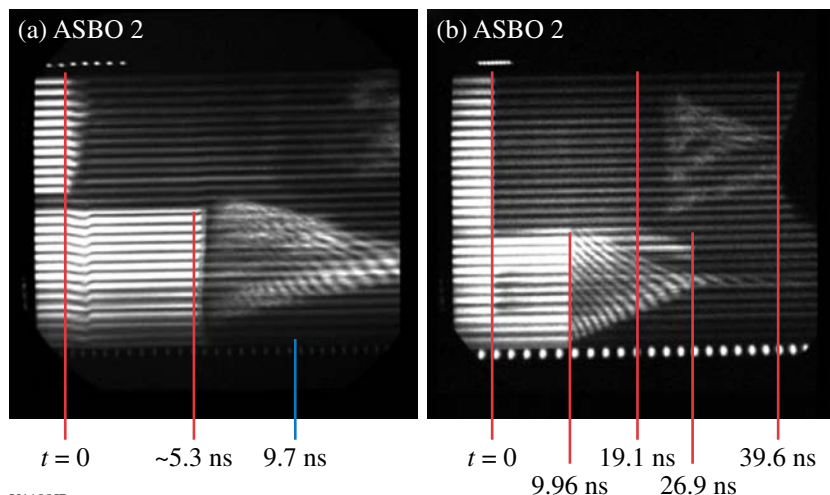
Figure 124.145
(a) VISAR signal from the target shown in Fig. 124.144, driven with 5488 J. No shock breakout is visible in the top of the image, and the reflected signal appears to come only from the back surface of the quartz anvil. (b) VISAR signal from a similar target driven with 3057 J. The shock breaks out of the $C_{10}H_{12}$ at about 19.1 ns and is visible in the quartz anvil before breaking out at 39.6 ns.

solid phase boundary. While analysis of the data is ongoing, a number of important observations were made (Fig. 124.147). It was verified that the sample design was feasible, data were produced across a wide range of shock pressures (20 to 200 GPa), and a reference material (Al) was used on each shot. Initial designs, based on extrapolation of diamond pressure-intensity measurements made at high pressures, proved to overestimate the achieved pressure. It was possible to generate the necessary data by utilizing the calibrant. This data will serve as the basis for future designs. Lastly, an interesting change in the reflectivity of the tin was observed during the apparent release portion of the loading. This remains to be explained.
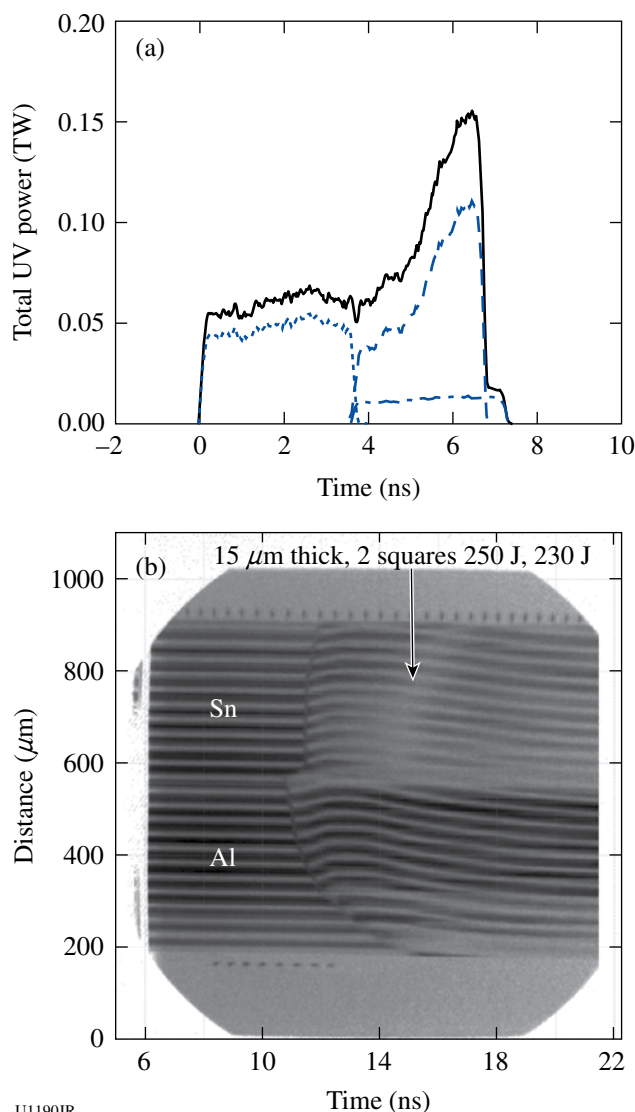
U1190JR

Figure 124.147
(a) Composite shock-ramp pulse shape used to generate first attempt at compression-driven resolidification in Sn. (b) VISAR recording showing late-time reflectivity changes (arrow) that occur only in the Sn.

High-Temperature Plasma Opacity: Opacity experiments in FY10 had three main goals. The first addressed physics questions from the very successful 2009 Ti opacity shots, where the observed Ti continuum opacity did not match code predictions, although spectral absorption lines from charge states consistent with ~120-eV LTE sample temperatures matched the code quite well. A modification in the configuration was made using thinner Ti samples, and new data were successfully taken on a half-day in January. A follow-up full-day experiment is scheduled for FY11.

The second goal was to better characterize the x-ray framing cameras (XRFC's) used on the experiments. NIF data from November 2009 revealed that the gain along with the gain profile of a microchannel-plate detector strip was sensitive to the relative delays between individual strips, as a result of electromagnetic crosstalk in the pulser input lines and the detector strips themselves. This effect produced ~3× differences in gain between strips, ~2× changes in the relative point-to-point gain in a single strip (compared to a synchronized-strip baseline case), and 30% to 50% changes in gain from one edge of a strip to the other (transverse to the pulse-propagation direction). The latter effect would impair the analysis of space-resolved gated absorption spectra if a similar effect occurred on the cameras used for opacity experiments. Data were taken for three framing cameras on OMEGA on 8 July, measuring these effects as a function of interstrip delay and gated detector pulse width. While the XRFC data showed ~2× differences in gain between strips, and significant (50% to 100%) changes in point-to-point relative gain along a strip, no significant gain variation across the strip was measured. Therefore, the performance of the camera was not a factor in the discrepancy in the Ti data.

The third goal was to compare short-pulse–heated opacity measurements with similar long-pulse conditions (Ti, $T \approx 100$ to 150 eV, density ~0.1 to 1.0 g/cm^3). In principle, much higher temperatures are possible with short-pulse–heated materials, but questions exist as to whether LTE conditions can be maintained. In these experiments, the OMEGA EP sidelighter beam was operated at 250- to 800-J, 100-ps pulse width and broad focus to heat an opacity sample at intensities between 10^{15} to 10^{17} W/cm^2. The OMEGA EP backlighter beam was delayed by 100 to 500 ps and then operated at 800 to 1000 J, 10 ps to drive a broadband 3- to 6-keV backlighter. The backlighter x rays probed the hot, expanded opacity sample. A separate line of sight allows one to take space- and energy-resolved sample emission spectra in a different spectral band. The experiment used the two opacity spectrometers that were transferred to OMEGA EP from the 60-beam OMEGA chamber and fielded

with "rotating SPCA" frames and time-integrated image-plate detectors. Shots in February demonstrated an opacity-quality broadband backlighter using a Zn microdot on an Al substrate, with data shown in Fig. 124.148. (Subsequent shots using a CH substrate failed as a result of very high instrument backgrounds but may have reflected a change in the pointing or laser conditions.) Further optimization of the backlighter will take place in FY11. In parallel, space-resolved broadband emission spectra from 10 to 50 Å were obtained from a CH/Ti/CH/Al exploding-foil sample (driven by the OMEGA EP sidelighter at ~10^{16} to 10^{17} W/cm^2). Al-, C-, and O-line features have been identified from a shot at lower intensity, along with a broad

U1191JR

Figure 124.148
Initial Zn microdot broadband backlighter spectra from ~3- to 6-keV photon energy.

continuum (see Fig. 124.149). Bright Ti emission was seen at higher intensity. Ti absorption lines were not observed; FY11 shots will assess whether this is caused by cool Ti plasma conditions or perhaps mistiming of the OMEGA EP backlighter and sidelighter. The source of the O lines is being investigated.

Hydrodynamics

Kelvin–Helmholtz instability experiments. A Kelvin–Helmholtz (KH) growth experiment was performed using a platform successfully developed in earlier OMEGA experiments.[48–50] The main goal of the most recent campaign was to measure turbulent mixing on an interface between CRF foam and I-doped plastic. Figure 124.150 shows a target schematic that consists of a plastic ablator and a shock tube. In the shock tube, the interface between low-density foam and high-density plastic had pre-imposed sinusoidal modulation at a wavelength of 400 μm and an amplitude of 30 μm. The central part of the plastic target contained a layer of I-doped CH to increase a contrast to 5-keV backlighter x rays. The ablator of the target was directly driven with laser light, producing a strong shock that propagated through the target. The shock produced a velocity gradient at the interface between the foam and plastic. This velocity difference between the two materials resulted in the KH growth of the surface modulations. The density of foam was varied from 50 mg/cc to 100 and 200 mg/cm^3. Turbulent mixing between a foam and plastic materials was expected to grow from short-scale surface finish modulations (with rms amplitude of 100 nm) on the interface between the two materials.

Figure 124.151 shows experimental data. The shock travelled from left to right, so the modulations on the left side of
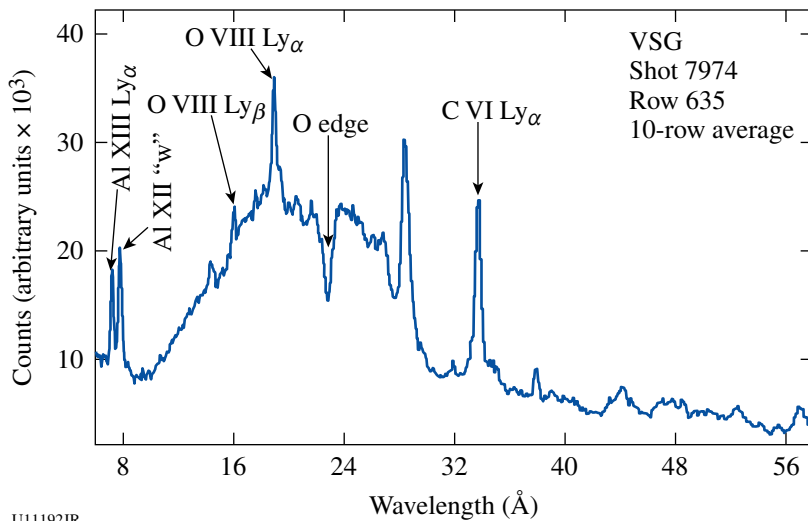

U11192JR
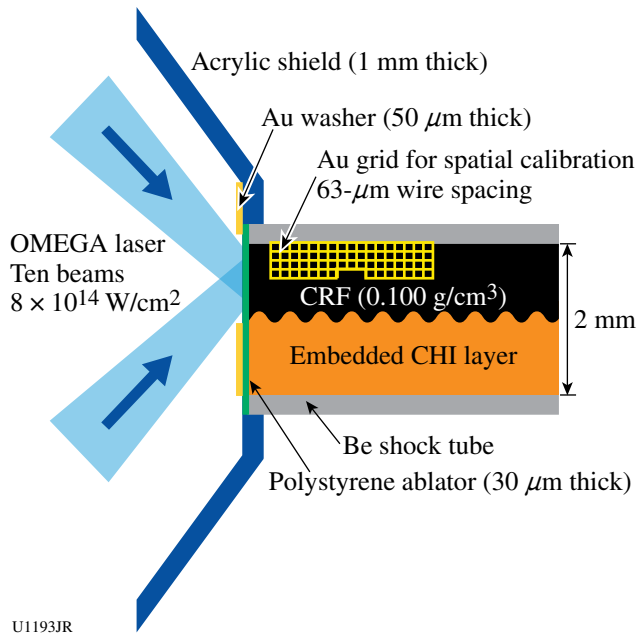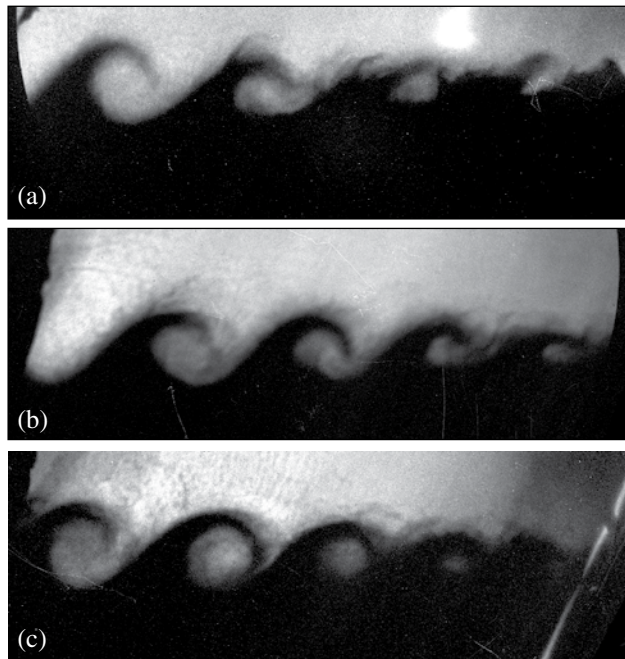
Figure 124.149
X-ray emission spectrum from the interior of the laser-driven CH/Ti/CH/Al foil, with initial line identifications.

Figure 124.150
Experimental configuration. The interface between lower-density CRF foam and higher-density I-doped plastic had a pre-imposed 2-D modulation with 400-μm wavelength. Three densities of CRF foam were used: 50, 100, and 200 mg/cm³.

Figure 124.151
X-ray radiographs of KH growth were taken with (a) 50 mg/cc of CRF foam at 47 ns, (b) 100 mg/cc of CRF foam at 75 ns, and (c) 200 mg/cc of CRF foam at 117 ns. The vortices on the right-hand side of the images experienced more KH growth than those on the left-hand side. Short-scale mix can be seen as "hair-like" structures on top of the vortices from pre-imposed modulations.

the image had more time to grow than the modulations on the right side. The light color in the image corresponded to foam material, while the dark color corresponded to plastic. The initial sinusoidal 400-μm-wavelength modulation developed into the vortices. In addition, the growth of short-scale modulations caused by surface imperfections developed "hair-like" nonuniformities. These nonuniformities represent turbulent mixing of two materials, as expected since the Reynolds number was high in this experiment, Re ~ 1 × 10⁶. The Reynolds numbers in hydrodynamic simulations, used to model the experiments, typically do not exceed ~1 × 10³ because of the finite spatial resolution of spatial grids. Therefore the simulations themselves are not expected to correctly predict evolution of short-scale mixing. These experimental data are used to develop and validate mix models that are based on post-processing of hydrodynamic simulations, currently in progress.

High-Mach-number Cu-foam jet experiments. Some of the most challenging experiments to model for hydrodynamics codes are jet-evolution experiments. Several aspects of hydrodynamics-code predictions can be validated by these experiments, including physics of shocks, material flows, and equation-of-state physics. The current experiment studied evolution of a Cu-foam jet into a low-density plastic foam. Figure 124.152 shows the experimental setup. A high-Mach-number jet was generated in a shock tube, driven by x rays from a hohlraum irradiated by 12 OMEGA drive beams. A point-projection backlighter x-ray source, driven by three beams, generated ~4.3-keV x rays that illuminated the jet at time intervals ranging from 15 to 35 ns after the beginning of
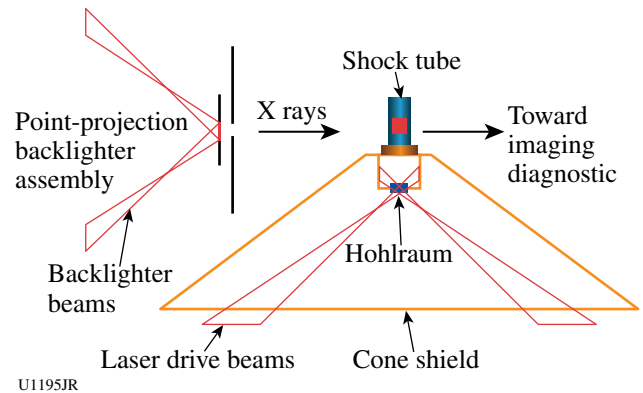
Figure 124.152
Experimental configuration of the high-Mach-number Cu-foam jet campaign. The jet was generated in a shock tube, driven by hohlraum x rays. X rays, generated by a point-projection backlighter, radiographed the jet at various times, from 15 to 35 ns after the beginning of the drive.

the drive. The cone shield prevented x rays generated in the hohlraum from reaching the imaging diagnostic, which would contribute to background on the data.

Figure 124.153 shows an example of a radiograph taken at 30 ns of the jet. In the image, a mushroom-like jet of Cu-foam material (darker color) penetrates the plastic foam (lighter color). The height, width, and position of the jet with respect to the grid (shown on the right side of the image) are some of the measurements used to compare with code predictions. In addition, the shock position and compression of the plastic foam will also be used to test various aspects of hydrodynamics codes. Preliminary simulations of jet evolution and shock propagation are close to experimental data, with much better agreement than in previous campaigns, primarily because of well-fabricated Cu foams.

U1196JR
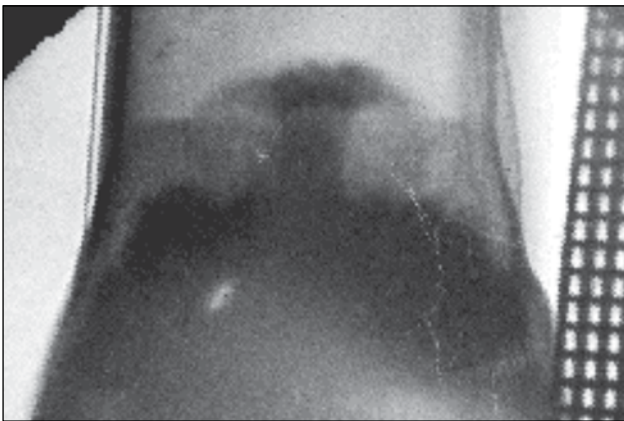
Figure 124.153
X-ray radiograph of a Cu-foam jet driven into a plastic foam with a density of 0.1 g/cc. The image was taken at ~30 ns after the beginning of the drive. The jet structure is clearly visible. The height, width, and position of the jet, as well as the shock position and compression of the plastic foam, will be used to test various aspects of hydrocodes.

X-Ray Source Development and Application: Bright, tunable x-ray sources are necessary for radiography applications, radiation-effects experiments, and use as backlighters for high-energy-density experiments. LLNL's x-ray source development campaign had one full day and two half-days of shots (22 shots total) during which two types of multi-keV x-ray sources were shot. These experiments were performed in collaboration with scientists from CEA (France). Two half-days (XRSD-10A, XRSD-10C) were used to investigate the performance of Ti foil targets confined by cylinders of ultralow-density SiO_2 aerogel material. A photo of one of the targets is shown in Fig. 124.154(a) (with bundled laser beams shown

schematically), and an x-ray image of the Ti K-shell emission (energies > 4.5 keV) from the target in shot 56933 is shown in Fig. 124.154(b). Target yields were studied as a function of the aerogel density, the aerogel volume, the foil thickness, the laser intensity, and the laser pulse length. Data are consistent with CEA predictions of an optimal aerogel density for maximal Ti K-shell radiation production.
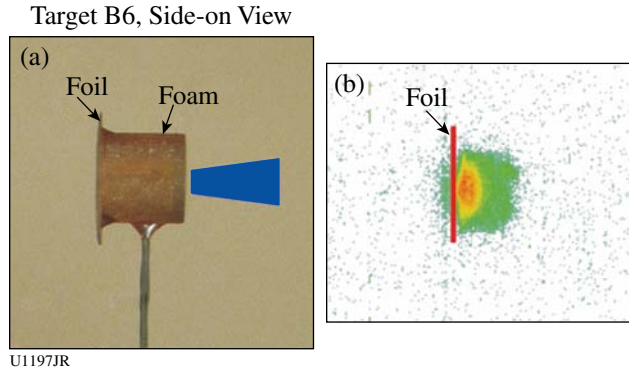
Target B6, Side-on View

U1197JR

Figure 124.154
(a) A hybrid foam-foil target that was shot in the LLNL–CEA x-ray source development experiments. Five or six OMEGA laser beams entered the target's foam cylinder from the left and created x rays from the Ti foil at the right. (b) An x-ray framing camera image from shot 56933 of a hybrid foam-foil target (2 mg/cm^3 of foam, 3-μm-thick foil).

Dedicated investigations of x-ray emission from noble gases were also carried out (XRSD-10B, XRSD-10C). During these experiments, the scaling of x-ray yield from gas-filled Be cans was studied as a function of gas-fill pressure and gas mixture. Pure Ar, Kr, and Xe targets were shot, as were mixed Ar:Xe targets; for all targets, fill pressures ranged from 1.0 to 1.5 atm. Figure 124.155 shows the measured spectra from five Xe-filled targets shot on the two dedicated days. During the XRSD-10B series of shots, the x-ray environments produced by the targets were also applied to investigate changes in the material properties of, and surface interactions on, sets of samples in response to x-ray loading. Samples included radiation-hardened-by-design mirrors and photovoltaic solar cells. An example of one specimen is shown in Fig. 124.155. Changes in reflectivity and surface profiles of the mirrors, and changes in the performance of the solar cells were characterized for exposures of several different fluences and spectral contents, which greatly expands the knowledge of the x-ray survivability of these materials.

Diagnostic Technique Development
Development of VISAR with a target-mounted turning mirror. It is known that measurement of the shock speed inside a quartz (Qz) window is a reliable way to understand the hohl-
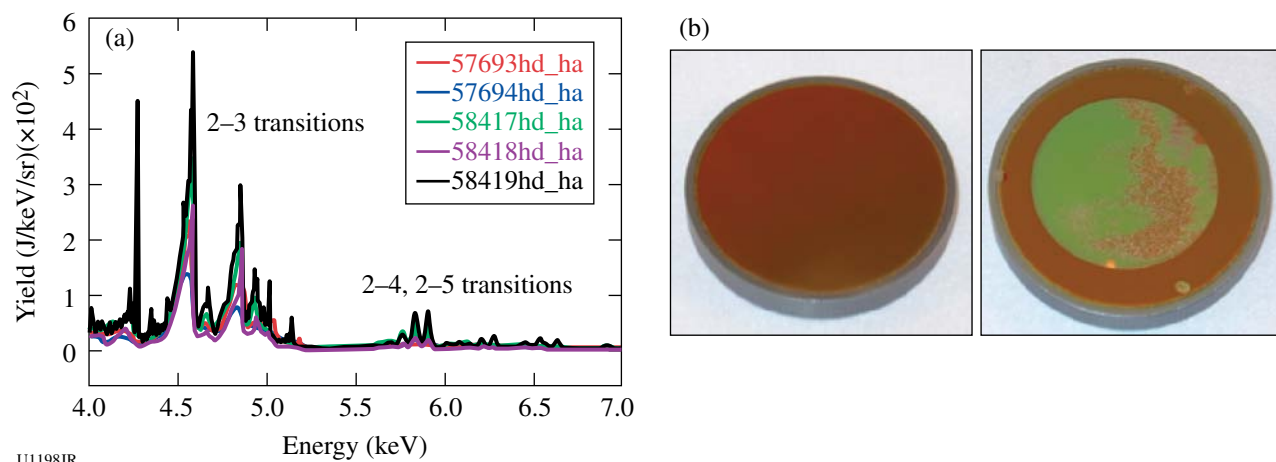
Figure 124.155

(a) The measured spectra from a series of Xe-filled targets shot during the x-ray source development and application campaigns in FY10. The x rays from the targets were used to study the response of radiation-hardened-by-design mirrors and photovoltaic solar cells. (b) Before and after images of a mirror specimen that was exposed to the unfiltered output of an Ar gas target on shot 57692.

raum drives.[51] One of the NIF experiments (Rad-Transport) will apply this technique to characterize the drive inside a half-hohlraum. Because the VISAR is located along the equator on the NIF, characterization of the drive at the end of a half-hohlraum requires the use of a target-mounted turning mirror. A potential failure mode was the loss of reflectivity from the turning as a result of M-band x-ray preheat. An experiment was designed to empirically test the turning mirror's performance under an equivalent heat loading of the NIF radiation-transport experiment. A new configuration was designed that carefully followed constraints from the simulations and experiments, as shown in Fig. 124.156(a). Two types of mirrors were tested: Si and nanodiamond mirrors. The experiments were highly successful—no mirror blanking was observed in Fig. 124.156(b). One example of the VISAR image is shown in Fig. 124.156(c). From this data, the peak shock velocity was measured up to 50 km/s, or ~50-Mbar pressure in quartz. This is the highest-pressure shock measured inside quartz to date. Both mirror types worked well and delivered high-quality meaningful data. From this data, it is expected that the mirrors will survive until the thinnest ablator section burns through and that the NIF experiment will deliver meaningful measurements.

Beryllium x-ray Thomson scattering. The objective of the BeXRTS-10 campaign was to isochorically heat Be utilizing short-pulse–generated hot electrons and to measure the plasma temperature by means of noncollective x-ray Thomson scattering with high time resolution. Two OMEGA EP short-pulse beams were used with the backlighter beam heating a 250-μm Be cube and the sidelighter beam creating a Zn K_α x-ray probe

at 8.6 keV. On this shot day, the sidelighter was delayed by 200 ps with an accuracy of ~25 ps, as observed by an ultrafast x-ray streak camera.

Zinc K_α x rays were scattered off the Be and collected by the Zinc von Hamos (ZVH) spectrometer, which uses a curved, highly efficient HOPG Bragg crystal for energy dispersion and focusing in the nondispersive direction. The spectrometer, specifically developed for the K_α scattering project, had to be rebuilt to meet new safety standards, and the new instrument was successfully fielded on this shot day.

A total of six shots were conducted including two low-energy activation shots. The latter ones were used to measure a high-resolution source spectrum and to record background signal levels. The facility had made a big effort to establish the beam timing, i.e., the delay between the backlighter and the sidelighter beams, on previous shot days. The single-photon–counting (SPC) camera was successfully used to observe the Zn K-shell source spectrum.

Compared to a previous shot campaign, the target size was significantly reduced and lower-Z shields were used in an effort to reduce bremsstrahlung levels. Different shield compositions were also tested. At the end of the shot day, an inelastically scattered Compton signal was successfully recorded from isochorically heated Be [cf. Fig. 124.157(b)], employing 62 J in the backlighter beam and 250 J in the sidelighter beam. These results represent significant progress compared to the previous shot campaign.
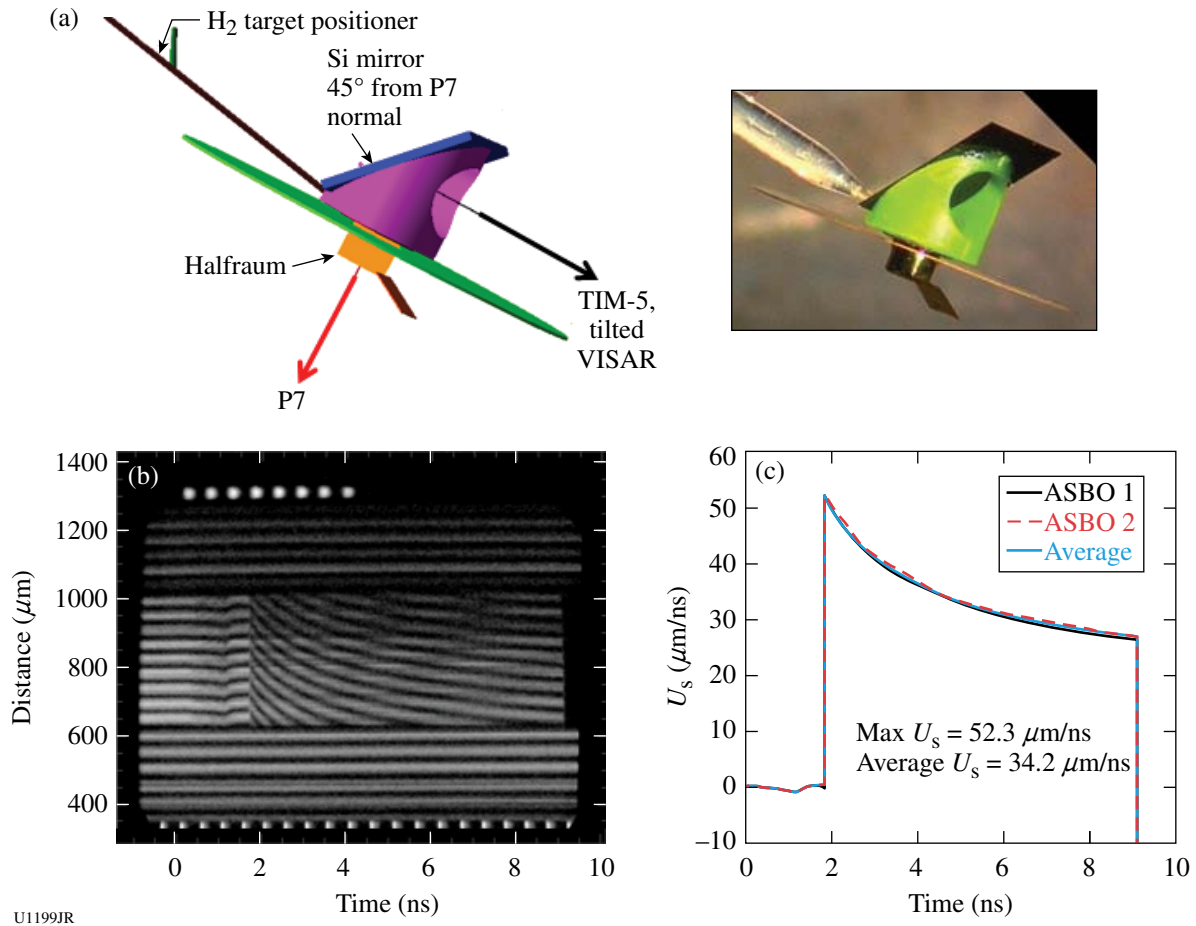
Figure 124.156

(a) VISAR mirror test experimental configuration. (b) An example of VISAR data measuring the shock speed in a SiO_2 window. No blanking is observed. (c) The measured shock speed is 52 μm/ns, corresponding to an ~50-Mbar ablation pressure.
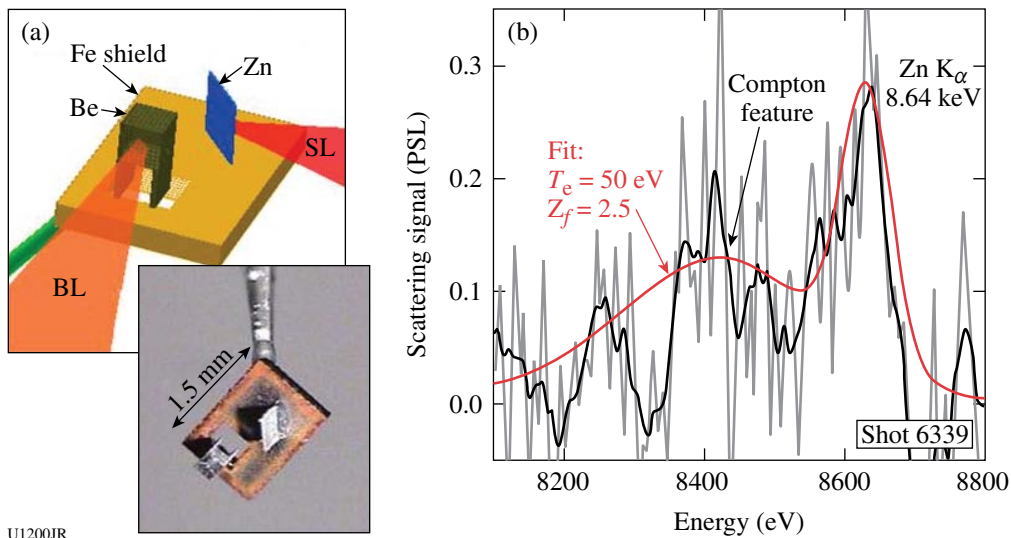
Figure 124.157

(a) Experimental configuration and (b) x-ray Thomson-scattering spectrum from isochorically heated Be, utilizing a Zn K_α source line at 8.6 keV. The experimental data are fitted with $T_e = 50$ eV and ionization of $Z_f = 2.5$.

<u>High-energy–backlighter development.</u> The goal of this experiment was to compare the backlighter conversion efficiencies of high-Z materials driven by short- and long-pulse lasers. Short-pulse–generated x rays are believed to result from hot electrons that collide with K-shell electrons, causing K_α x-ray fluorescence. Long-pulse–generated x rays are believed to be created by thermal heating and ionization of the material. The goal was to perform systematic comparisons at high x-ray energies. The OMEGA EP Laser System is ideal for this type of test since both short- and long-pulse lasers are available to illuminate a target using the same diagnostics. In this set of experiments, three different types of materials were tested: Cu, Ag, and Sm. The initial analysis shows that the long pulse is much more efficient at generating the 8-keV Cu backlighter; whereas the 40-keV Sm x ray is much more efficiently generated with the short-pulse lasers. From these data, it was observed that the conversion efficiencies are approximately the same at ~17 keV, driven by either long- or short-pulse lasers (Fig. 124.158). At 8 keV, the long-pulse laser was more efficient by a factor of 10, whereas at 22 keV, the short-pulse laser was more efficient by a factor of 5.

<u>Broadband x-ray Laue diffraction development.</u> The lattice scattering campaign uses the broadband thermal x-ray emission from a direct-drive–implosion capsule to perform single-shot, *in-situ* white-light x-ray diffraction. This employs the classic Laue diffraction on a subnanosecond time scale to investigate material behavior during shock or ramp compression. This technique will give insight into the material microstructure because lattice defects will cause nonuniform strain in the atomic structure, causing the diffraction spots to broaden and change shape. A directly driven implosion on the OMEGA laser is ideally suited for this technique, providing a short burst (~150 ps) of bright broadband x rays. The laser beams were pointed to five different pointing locations on the capsule to maintain implosion symmetry. Figure 124.159 shows gated framing camera images of the implosion capsule on a previous campaign that had 42 beams for the implosion, while Fig. 124.160 shows the improved symmetry by using the five different targeting locations. In principle, symmetry can be improved even further by adding more locations.

For these experiments the broadband x-ray diffraction (BBXRD) diagnostic was designed and qualified (Fig. 124.161). The diagnostic is designed with a tapered profile so that as many beams as possible can reach an implosion capsule placed 20 mm away from the single-crystal target that sits on the front plate of the BBXRD. The inside of the BBXRD has four trapezoidal image plate detectors on the tapered sides and a square piece on the back to record the transmitted diffraction. Simultaneous VISAR measurements can be made from the rear surface through a hole in the back plate. The diagnostics capability was successfully demonstrated on two campaigns
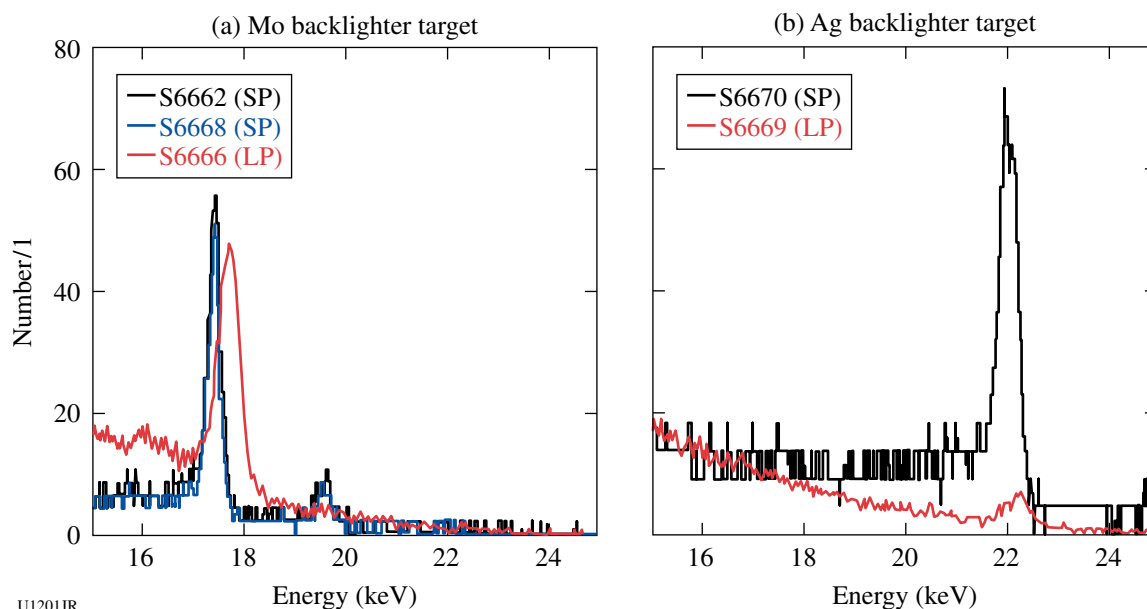

Figure 124.158

Comparison of high-energy backlighter yields driven by the 1-ns, 3ω long-pulse (LP) laser versus the 100-ps, 1ω short-pulse (SP) laser. The data were taken with the single-photon–counting camera. When normalized by the laser energies, we found that the Mo backlighter conversion efficiencies were about the same, whether driven by the short pulse or the long pulse.
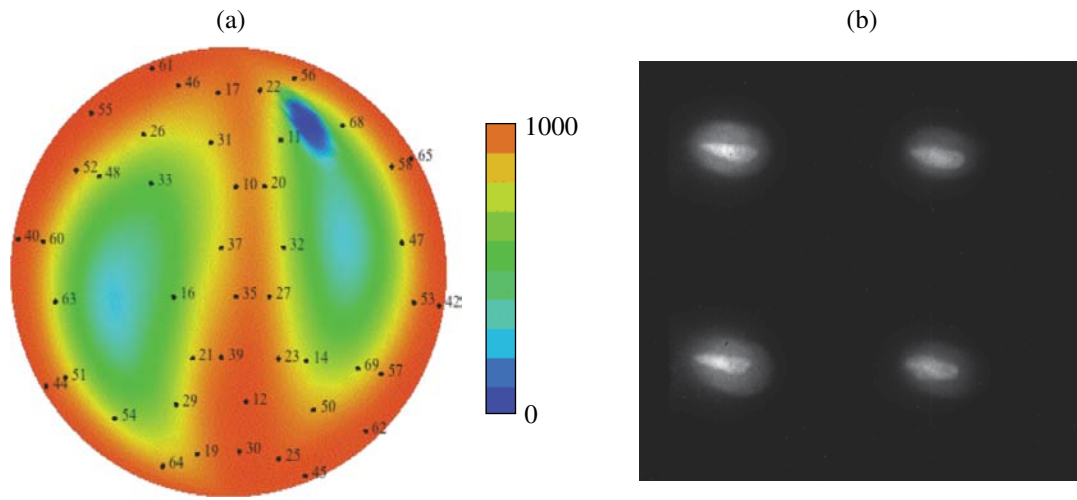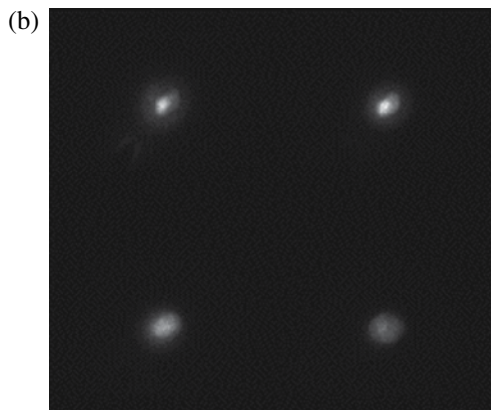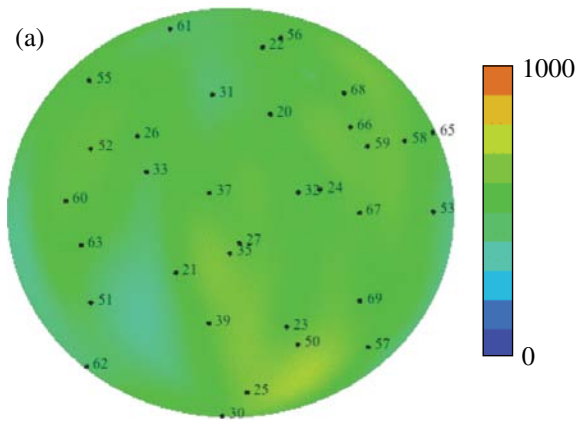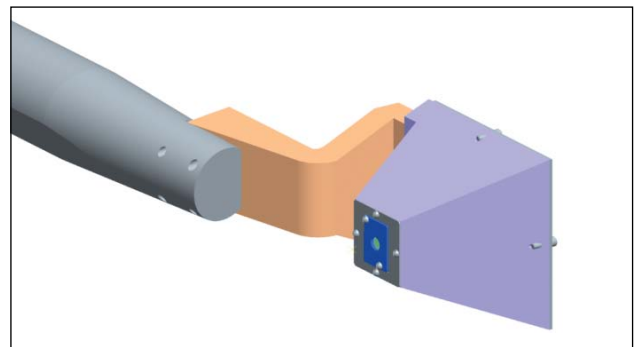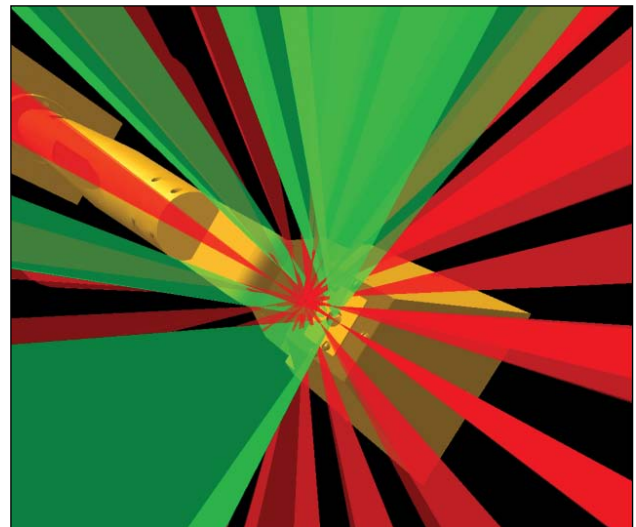
Figure 124.159

(a) The total laser power deposited and (b) gated framing camera images from the implosion capsule using 42 beams pointed to the center of the capsule.

U1203JR

Figure 124.160

(a) The total laser power deposited (TW/cm^2) and (b) gated framing camera images from the implosion capsule using 33 beams pointed to five different targeting locations on the capsule.

U1204JR

Figure 124.161

The BBXRD diagnostic in the VISRAD model showing the location of the implosion capsule and beams and CAD model.

of shock-compressed silicon (shown in Fig. 124.162) and copper. For the silicon images shown, it was estimated that the anisotropy in the compression by the shift in the spots was approximately 8% along the driven direction.

Powder x-ray diffraction development. The objective of this campaign is to demonstrate the use of powder x-ray diffraction

U1205JR

Figure 124.162
The tip of one of the trapezoidal image plates showing diffraction from uncompressed and shock-compressed silicon.

methods in the characterization of dynamically loaded (shocked and ramped) polycrystalline materials, particularly with a view to application on forthcoming NIF experiments. Such x-ray diffraction methods offer insight into processes occurring on the scale of the material lattice, which in turn determine the macroscopic response of the material to dynamic loads (e.g., its strength).

To date, the campaign has demonstrated x-ray diffraction from polycrystalline Ta foils using a quasi-monochromatic Mo backlighter source (see Fig. 124.163). Future campaigns will concentrate on improving the signal-to-noise ratio of the diffraction signal and will then aim to use this signal to characterize tantalum under a variety of shock and ramp-loaded conditions.

Powder x-ray diffraction measurements of solid Fe, Sn, and Ta to 500 GPa. An experimental platform was developed to measure powder x-ray diffraction on solid samples at pressures above Hugoniot melt. Fe, Sn, and Ta samples were sandwiched between a diamond pusher and window and ramp-compressed to high pressure and density using up to six OMEGA beams. VISAR velocity measurements were used to infer the pressure history in the sample, and the 8.37-keV Cu-He$_\alpha$ x-ray source, driven by ten beams, was timed to coincide with the peak pressure. The diffraction signal was collimated through

U1206JR

Figure 124.163
(a) Diffraction signature from polycrystalline Ta foil using a 17.5-keV x-ray source and LLNL broadband x-ray diffraction (BBXRD) diagnostics. Each crystallographic plane (hkl) generates a characteristic cone of x rays; the intersection of these cones with the image plate detectors results in a characteristic ring pattern. (b) Calculated pattern shown overlaid over data.

a 300-μm-diam aperture in a 150-μm-thick Ta substrate and captured on image-plate detectors. Density was inferred from the diffraction data by assuming a crystal structure, then verifying self-consistency with a best fit to density. Maximum diffraction pressures attained on Fe, Ta, and Sn samples were 480, 310, and 220 GPa, respectively, all above Hugoniot melt. Data from iron samples are shown in Fig. 124.164.
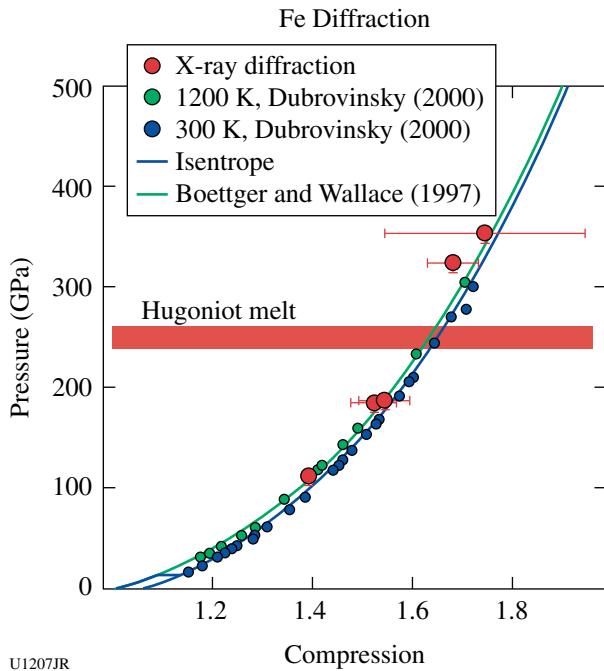

Figure 124.164
In FY10, the OMEGA laser was used to obtain x-ray diffraction measurements of solid Fe (red circles) at pressures above the Hugoniot melt (red band at 250 GPa). The results are consistent with Fe remaining in an HCP structure up to the highest pressures observed (~480 GPa). Diffraction data from diamond anvil cells[52] are also shown, along with a theoretical isentrope from Ref. 53.

ACKNOWLEDGMENT

FY10 LANL OMEGA Experimental Programs
In FY10, Los Alamos National Laboratory (LANL) executed 135 shots on the OMEGA Laser System and 24 shots on the OMEGA EP Laser System. LANL had three instruments qualified for use on OMEGA EP: the NIF5 spectrometer, the target-heating Verdi laser (THVL), and Thomson parabola ion energy (TPIE) diagnostic.

LANL experiments contributed to the National Ignition Campaign (NIC) in the following ways:

- Studies of the equation of state (EOS) of plastic ablators
- New experimental methods for determining the areal density of imploded ICF capsules using 4.44-MeV ^{12}C(n,n') γ rays
- Demonstration of NIF components of the neutron imaging system

High-energy-density (HED) campaigns included

- Measurement of a supersonic radiation wave
- Measurement of capsule yield in the presence of high-Z dopants
- DT reaction product branching ratio measurements
- Energetic-ion generation from hemispherical targets
- Development of x-ray sources for phase-contrast imaging

Collaborations with AWE, LLE, LLNL, NRL, and National Security Technologies (NSTec) remain an important component of LANL's program on OMEGA.

CHaRM: Disagreement between EOS models is found in the prediction of bump evolution, which the CHaRM campaign hopes to resolve. This year a campaign began to measure the ablative Richtmyer–Meshkov (aRM) growth of isolated Gaussian-shaped bumps on plastic ablators. The ablative Richtmyer–Meshkov instability operates at the ablation front and is important because it controls the ablation surface perturbations present at the onset of Rayleigh–Taylor growth, which initiates once the shock has broken out and begins to accelerate the capsule.

General Atomics has sputtered 25-μm FWHM bumps, which are 4 to 8 μm tall, onto 120-μm-thick planar plastic ablators. The ablators are placed over one side of 0.9-scale gold halfraums (see Fig. 124.165), which are driven to 65-eV radiation temperatures corresponding to NIC foot levels. On-axis x-ray radiography using Saran backlighters (2.8 keV) allows one to measure bump areal density at successive times. Experiments this year have been hampered by low contrast from the combination of small areal-density variations from which to measure, as well as unwanted high-energy x rays in the system. An example of a measured low-contrast, 5-μm bump is shown in Fig. 124.166. The center of the bump (and lineout) shows a region of higher transmission, characteristic of a bump with a dip at its peak, which agrees with predictions at this time (4 ns after the start of the laser drive). Higher-contrast experiments are planned for FY11 along with shock-speed measurements to independently measure the drive conditions.

*Gamma Reaction History:* Gamma-ray measurements on fusion implosions were further developed for the NIC using
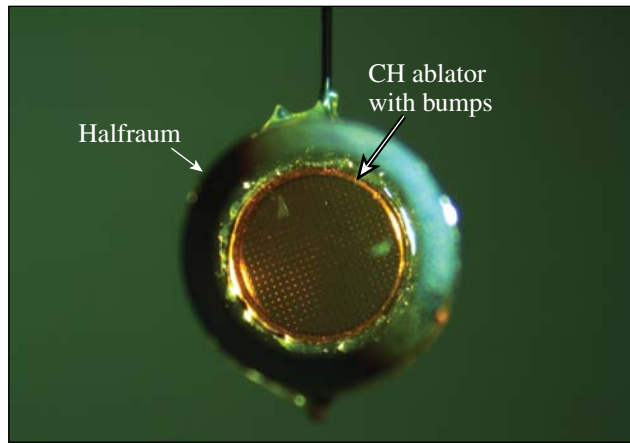
Figure 124.165
An optical image of a CHaRM target showing the perturbed plastic on the end of a 0.9-scale gold halfrum.

the gamma reaction history (GRH) diagnostic in FY10 (see Fig. 124.167). The GRH was first installed on the exterior of the OMEGA target chamber in 2009 (see Fig. 124.168). This instrument is a gas Cherenkov detector (GCD) designed for the NIF and being tested and used for nuclear studies on OMEGA. GCD's convert energetic γ rays to UV/visible Cherenkov photons for collection by fast optical recording systems. System impulse response better than 100-ps FWHM has been made possible by the combination of low-temporal-dispersion GCD's, ultrafast microchannel-plate photomultiplier tubes (PMT's),
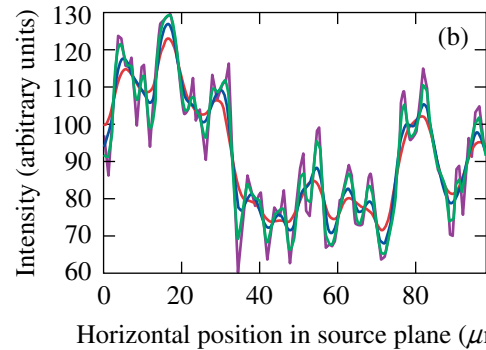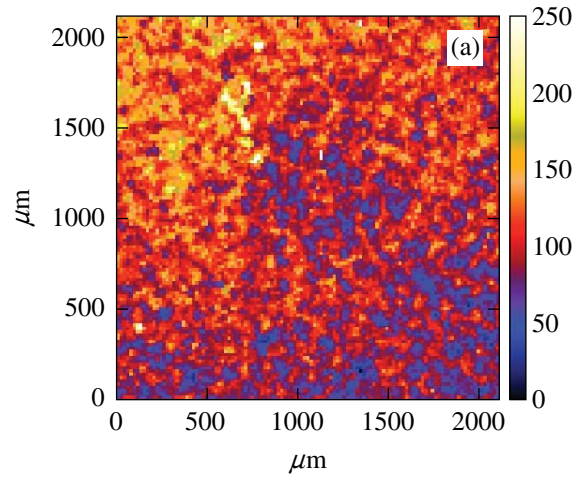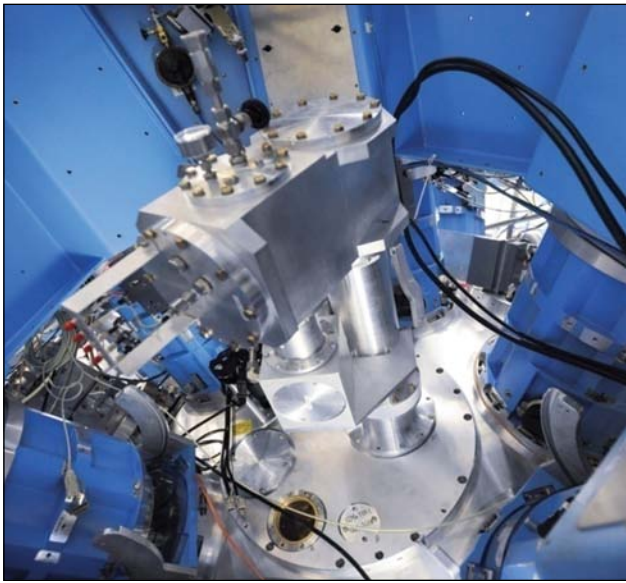

Figure 124.166
Image of the backlighter data obtained from radiography of a perturbed surface. The lineout indicates the presence of a bump.
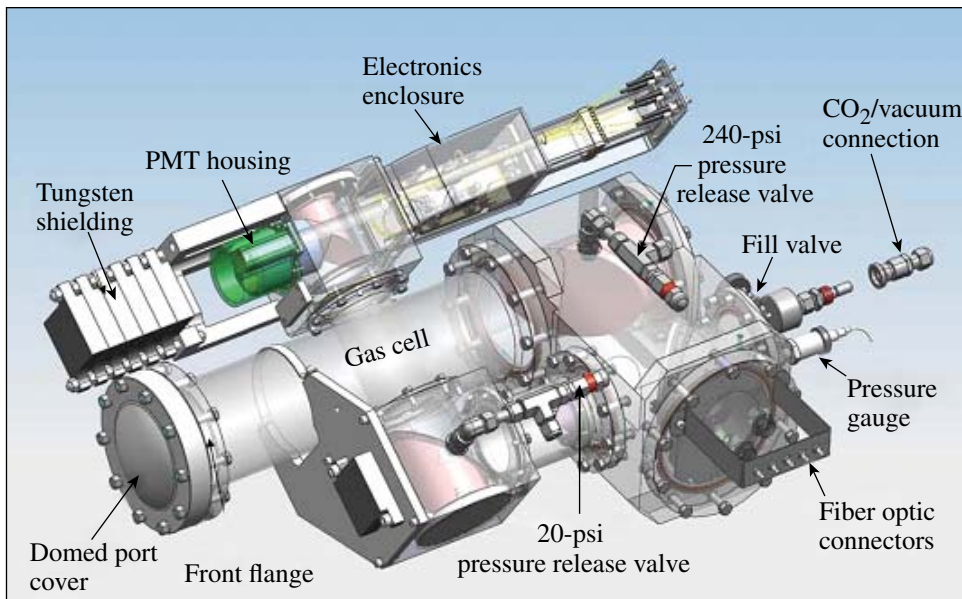
Figure 124.167
Isometric view of the GRH diagnostic. After exiting the target chamber, energetic γ rays interact with a converter plate inside the domed port cover. The resulting relativistic electrons with energy above threshold generate UV/visible Cherenkov radiation inside the pressurized gas cell. A series of off-axis parabolic mirrors concentrate this light down to a 1-cm-diam active area of an ultrafast photomultiplier tube located inside the PMT housing. The electrical signal from the PMT is converted to infrared photons by a Mach–Zehnder modulator inside the electronics enclosure. This optical signal is then converted back to an electrical signal using high-speed photoreceivers connected directly to high-speed digitizers. The PMT is well shielded against direct-radiation effects by the tungsten shielding. Calibration and timing fiducial signals are injected into the optical path through the fiber-optic connectors.

U1211JR

Figure 124.168
Photograph of the GRH attached to the OMEGA target chamber.

and high-bandwidth Mach–Zehnder fiber-optic data links and digitizers, resulting in burnwidth measurement accuracy better than 10 ps.

The GRH was absolutely timed using x rays from Au-ball shots on OMEGA. It has been shown that fusion bang times measured using the GCD-1 and the GRH agree to within 5 ps on average. Error budgets indicate that the GRH will be able

to meet the NIF requirement of measuring bang time to within 30 ps relative to the start of the laser pulse. Figure 124.169 shows raw GRH data placed on the laser time base along with the 1-ns laser pulse. Data with and without pressurized CO_2 demonstrate Cherenkov production and backgrounds, respectively.

Inherent variable energy-thresholding capability allows one to use GCD's as γ-ray spectrometers to explore fusion and other interesting nuclear processes. Recent GRH measurements of 4.44-MeV $^{12}C(n,n')$ γ rays produced as 14.1-MeV DT fusion neutrons pass through plastic capsules are paving the way for a new CH-ablator areal density measurement. This measurement is made possible by the use of SF_6 at high pressure (200 psia) resulting in a 3-MeV Cherenkov threshold.

The NIF GRH system consists of four individual gas cells, all essentially identical to the GRH on OMEGA. Located 6 m from target chamber center, the GRH-6m system began taking data on NIF in September 2010. OMEGA has provided an excellent platform to develop the detector technology and measurement techniques and will continue to provide a test bed for new physics investigations using GRH in the future.

The Neutron-Imaging System: In FY10, LANL successfully tested a major component of the NIF neutron-imaging system using the Omega Laser Facility. In order to record two images (14-MeV primary and 10- to 12-MeV down-scattered), a complex, multi-element lens (Fig. 124.170) must be used to view the front side of the neutron-to-light scintillator. Preliminary
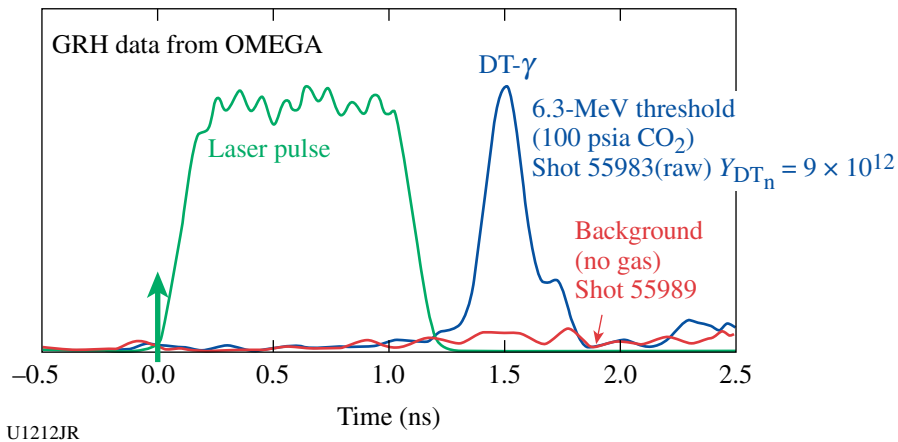

U1212JR

Figure 124.169
Raw GRH data shown on the laser time base along with the 1-ns laser pulse used to drive the fusion implosion. The GRH was pressurized with 100-psia CO_2 for shot 55983, resulting in a 6.3-MeV Cherenkov threshold. DT fusion γ rays at 16.75 MeV produced the signal shown. The small peak riding on the tail of the main peak is a result of ringing in the PMT. This feature is removed, and the main peak is sharpened by deconvolving the instrument response of the system. The GRH, evacuated for shot 55989, provided a background measurement of direct radiation interaction with the PMT and demonstrated gas is necessary to generate a real signal.

data analysis indicates that the lens channel obtains a source plane resolution close to 10 μm and comparable to the fiber-coupled channel.

Flat-field images at prompt gamma time of flight and NIF down-scattered neutron time of flight were collected for important scintillator background and temporal response studies.

NIF-5

Radiation flow. The NIF-5 project obtained invaluable data on OMEGA for the development of a future NIF diagnostic to measure the propagation of a supersonic radiation front in a low-density foam. These data were obtained using two principal diagnostics: the NIF-5 spectrometer with the GXI-T detector and an x-ray backlighter to perform absorption spectroscopy of
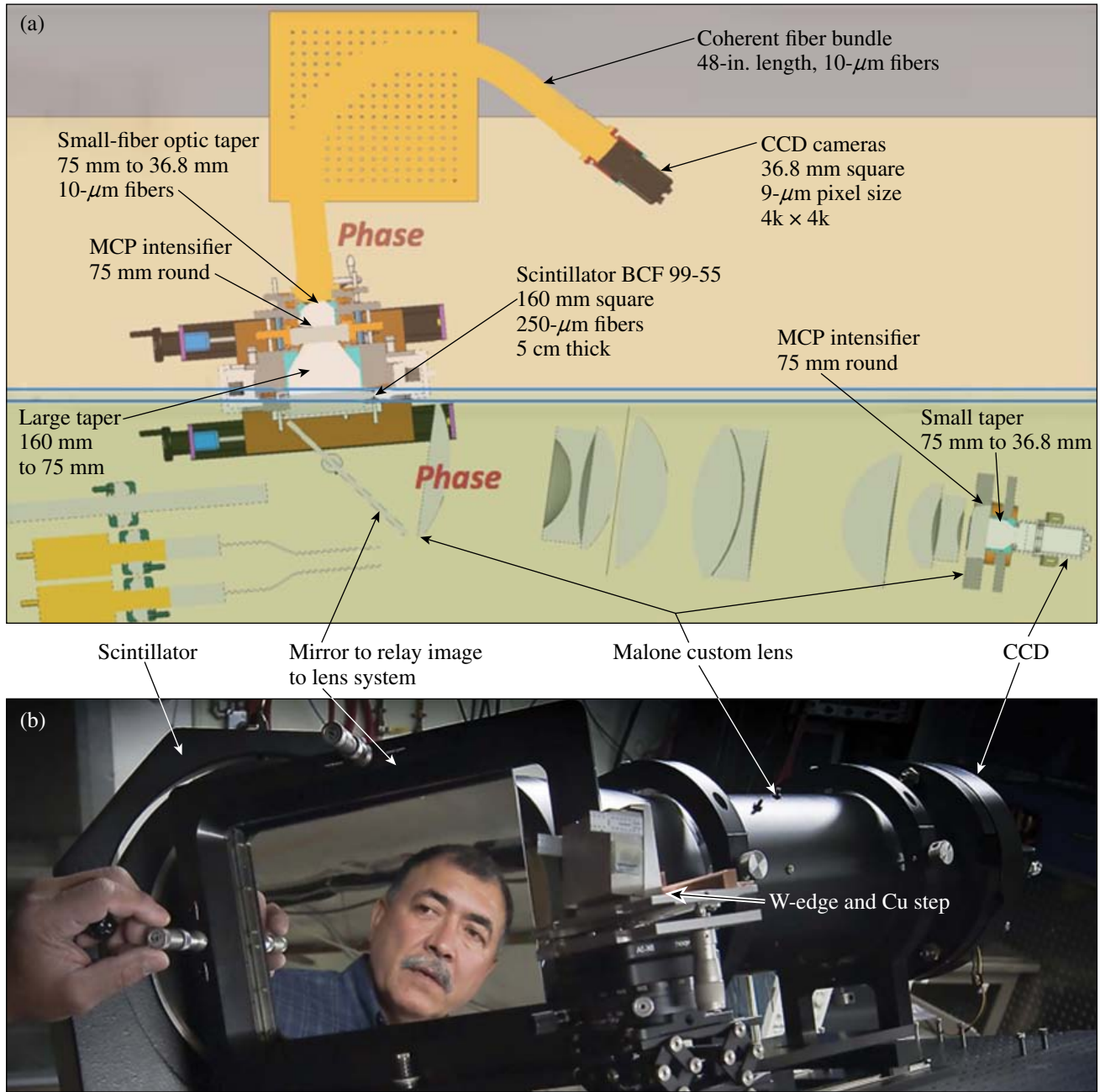
U1213JR

Figure 124.170
(a) A schematic of the neutron imaging system; (b) a photograph of the neutron-imaging system while being aligned.

a tracer foil, and an x-ray framing camera and x-ray backlighter to measure the hydrodynamic expansion of the same foil. Together, these two diagnostics greatly constrain the models in an effort to better validate simulation codes.

The radiation flows from the hohlraum (top left, Fig. 124.171) and into a Be tube filled with a low-density (65-mg/cc) CH foam (bottom left, Fig. 124.171). A thin, square Ti foil (shown in blue but at an angle in the figure) is embedded in the target to diagnose the propagation of the radiation front down the tube. The hydrodynamic expansion of the foil (viewed edge-on) and the shock wave in the tube wall were imaged using an x-ray backlighter. The inset compares our data and a 2-D cylindrical *RAGE* simulation of the shock in the tube wall. The code is able

to qualitatively recreate the data. A more-detailed quantitative analysis is currently underway.

The absorption of CsI x rays by the foil in the orthogonal direction was also measured, providing a measurement of the charge state of the foil as a function of location along the radiation propagation direction. Figure 124.172 shows a schematic of the diagnostic: GXI-T with a Ge (111) crystal spectrometer snout. The absorption spectrum of the tracer was measured (along the detector strips) as a function of distance from the Au can bottom (orthogonal direction). Results are shown Fig. 124.173, along with a simulated Ti absorption spectrum, the latter showing the absorption lines expected given a certain foil temperature. The data show the Ti absorption lines
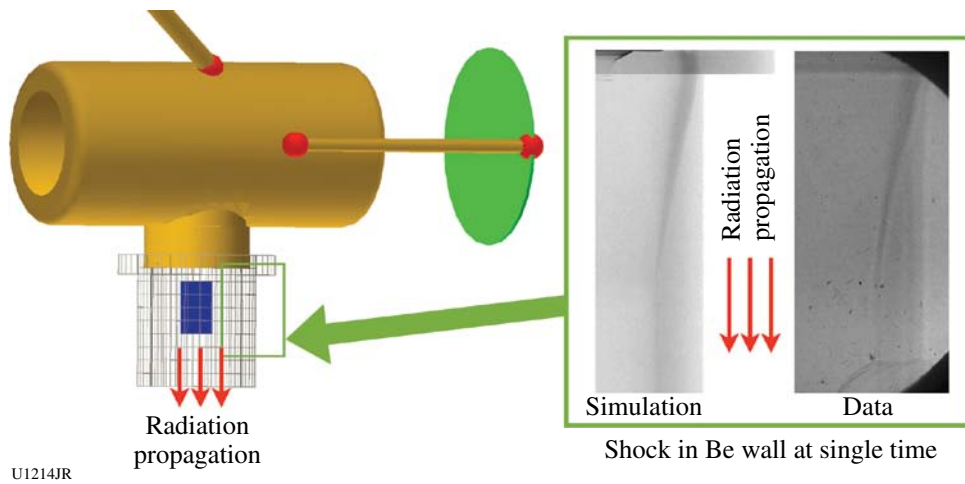

Figure 124.171
Radiation flows from the source, a hohlraum, into a foam cylinder (with an embedded tracer foil, in blue) enclosed in a Be tube (cross-hatched region). Inset: A comparison of simulation and data showing the shock in the tube wall.
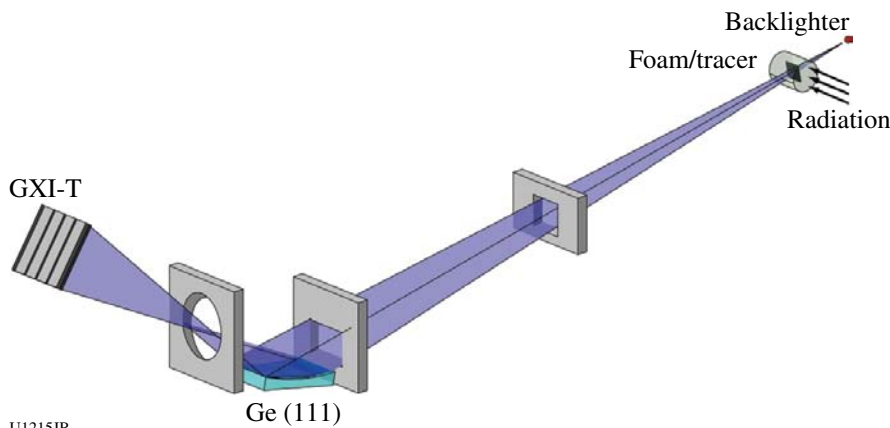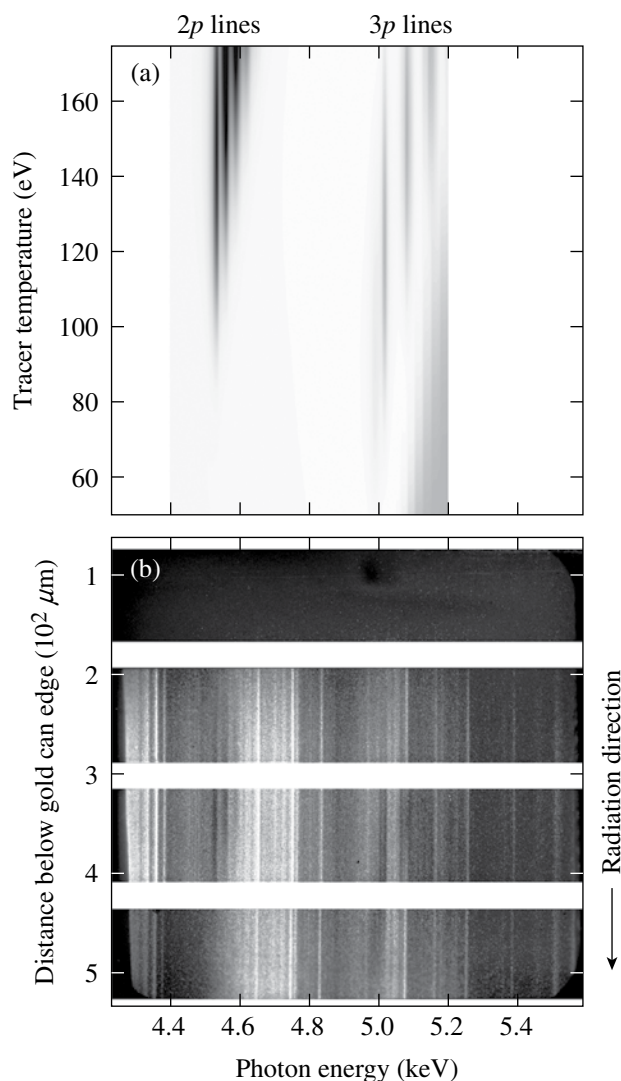

Figure 124.172
Schematic of the diagnostic foam/tracer (target not to scale). A broadband x-ray backlighter illuminates a thin foil embedded in a low-density foam cylinder as a radiation front travels across it. The image of the foil is dispersed along one axis by a curved Ge crystal. The detector is composed of four separately gated strips.
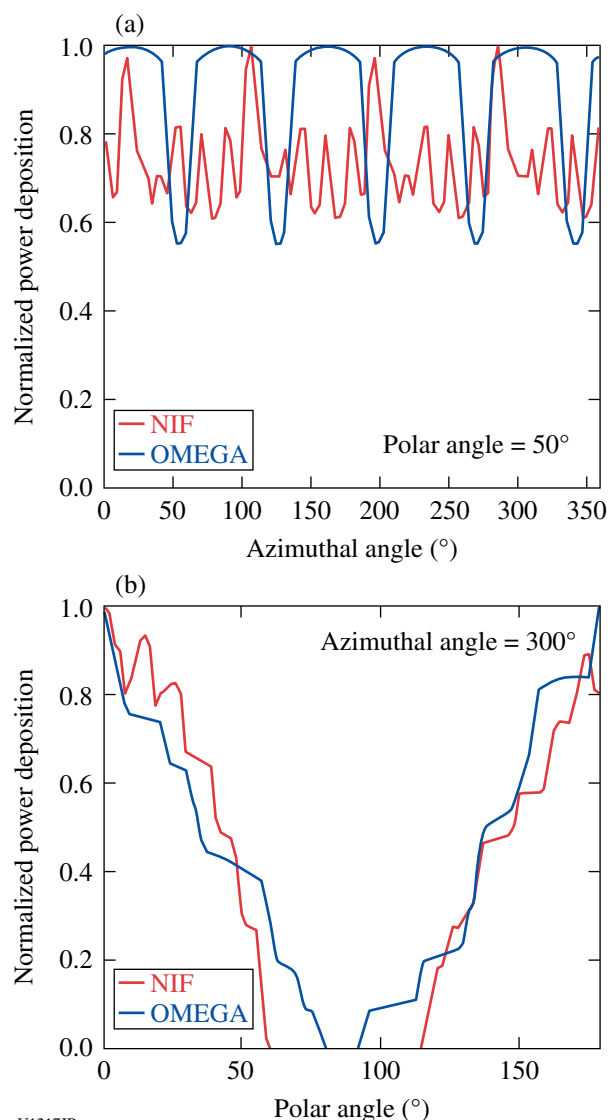
Figure 124.173

(a) Simulated titanium absorption spectrum showing how the absorption lines can be used to determine the temperature of the tracer foil. (b) Data showing the titanium absorption lines overlaid onto our CsI backlighter-emission spectrum.

overlaid on the CsI backlighter emission spectrum. The initial analysis shows an ~200-mm-long radiation front with the tracer temperature ranging from ~130 eV midway down the foil to ~50 eV at the end of the foil.

Short-duration backlighters. The NIF-5 campaign also executed a two-prong investigation into short-pulse quasi-continuum backlighters. This involved experiments on OMEGA EP using short-pulse lasers to irradiate a foil target and OMEGA experiments imploding Kr-fill capsules using a NIF-like irradiation pattern.

On the NIF, capsules must be polar driven because of the laser-beam geometry. Experiments were performed to determine what effect a polar-driven laser drive has on a capsule backlighter. Figure 124.174(a) shows the normalized laser power deposition in the azimuthal direction at the NIF and OMEGA. Although there are differences in the details, the peak-to-trough difference is nearly the same for both. Figure 124.174(b) shows the laser deposition as a function of polar angle for both the NIF and OMEGA configurations. Although there is some slight discrepancy, particularly at the equator, the profiles are very similar.

Figure 124.174

Lineouts of the NIF and OMEGA laser power deposition profiles in the (a) azimuthal and (b) polar directions.
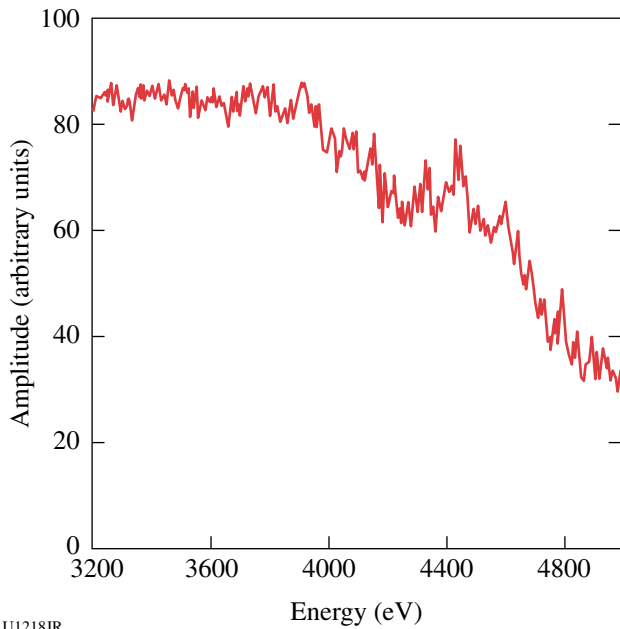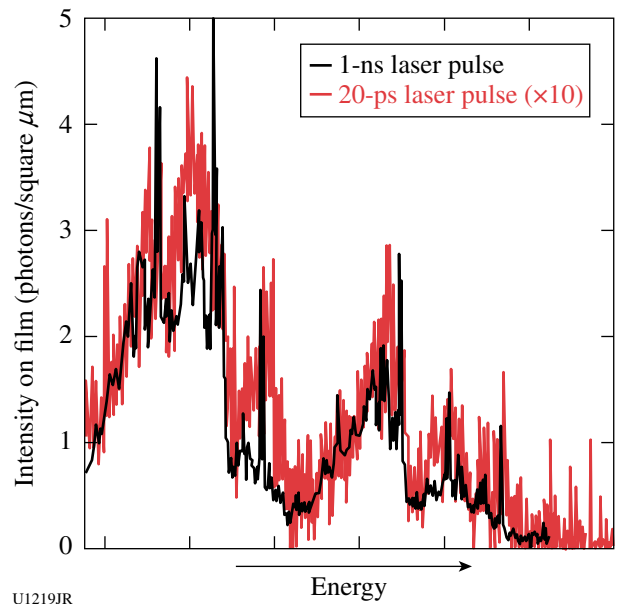
Figure 124.175
Signal amplitude versus photon energy for the bright core of a Kr capsule implosion.

Figure 124.176
A comparison of the L-shell emission from a CsI foil resulting from irradiation from a 1-ns laser (black) and a 20-ps laser (red). The intensity of the 20-ps data has been multiplied by a factor of 10 to fit on the same scale as the 1-ns data.

Figure 124.175 shows the spectrum from a Kr capsule implosion. The spectrum is much more uniform than one would measure for a foil target, such as an L- or M-shell emitter, which is often chosen for spectroscopic measurements.

Experiments conducted on OMEGA EP studied both the K-shell and L-shell spectra of a CsI foil at three different laser pulse lengths (20 ps, 40 ps, and 1 ns). Figure 124.176 shows the L-shell spectrum of a CsI foil generated by a 1-ns and a 20-ps laser pulse. While the 1-ns spectrum has many narrow features, the 20-ps data show a broadening of the spectral lines.

The results of both of these backlighter experiments have provided invaluable data to evaluate their use for future LANL-led NIF experiments.

High-Z: The High-Z campaign had two main objectives: (1) to determine if the yield from plastic capsules would behave similarly to the yield of glass capsules when a high-*Z* dopant was added, and (2) to measure if the Ti x-ray emission from the Ti dopant in the shell was sufficiently high to use the multiframe monochromatic imager (MMI) in future experiments. The MMI diagnostic allows one to measure spatial and temporal profiles of the electron density and temperature in the plasma.

To check the equivalency between plastic and glass capsules, a 900-μm-diam, 13.5-μm-thick plastic-shell target that contained 10 atm of D_2 gas was imploded and doped with varying amounts of Kr gas. The Kr gas-fill levels were designed to cover a range that produced significant degradation in the yield of the glass-shell capsules measured in previous experiments. In addition, some of the capsules contained Ti doped into the inner 1.5 μm of the plastic shell. The implosions were driven using the 60-beam OMEGA laser with full beam smoothing, resulting in a total laser energy of 23 kJ.

These experiments successfully demonstrated the equivalent behavior of the plastic capsules to the glass capsules as the Kr dopant level in the gas was increased. We also obtained Ti emission measurements from the capsule implosions. Based on these results, the second shot day was focused on enhancing the Ti emission from the capsules to improve the feasibility of using the MMI diagnostic.

Some examples of the spectrometer and imaging data are shown in Figs. 124.177 and 124.178. Figure 124.177 shows an image from the Henway time-integrated spectrometer for shot 56577. X-ray H-like and He-like Ti emission lines 2–1 transitions can be seen on channel C and 3–1 transitions on channel A. One can also see an absorption feature on channel C that comes from the colder Ti in the shell near the peak of

the implosion. The different horizontal strips in each image represent different filters that are used to provide a wavelength calibration. Figure 124.178 shows multiple images using the DDMMI spectrometer.

Good neutron data were also obtained from these shots. A comparison of the yield as a function of Kr dopant between the glass and plastic capsules is shown in Figure 124.179. The data indicate that the plastic capsules behave very similarly to the glass capsules with the yield dropping as the Kr concentration is increased, just as it did for the gas capsules. This indicates that the physics important for the observed degradation in yield

do not depend on the capsule material. In the future, we will use whichever type of capsule is appropriate for obtaining a better understanding of this physics.

The goal of additional experiments with these shots was to improve the Ti emission from the capsule implosions so that the DDMMI diagnostic could be used to measure temperature and density profiles in the gas. At present, the data for these shots are still being analyzed, and an evaluation will be made concerning the usefulness of these Ti-doped plastic capsules to enable one to measure the DDMMI of the plasma properties in the gas.
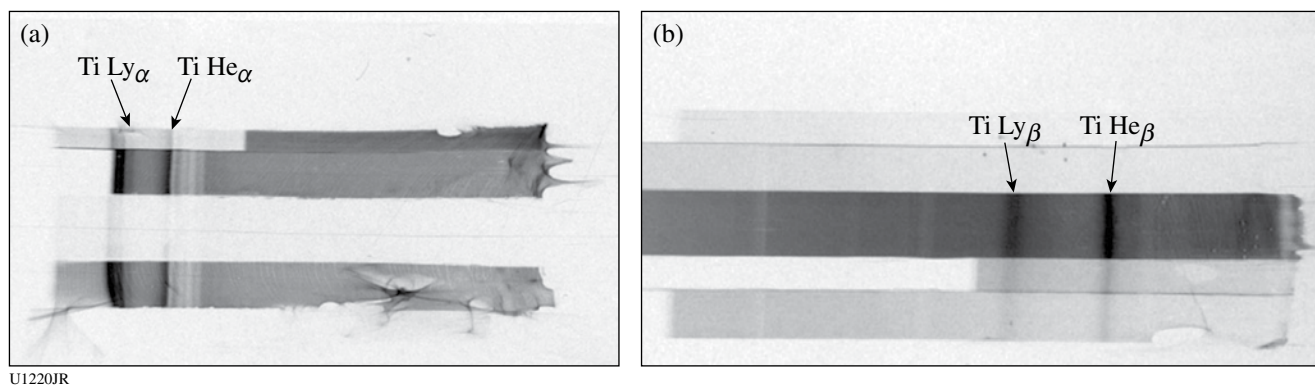

U1220JR

Figure 124.177
(a) Henway data showing the Ti He$_\alpha$ and Ti Ly$_\alpha$ lines; (b) Henway data showing the Ti He$_\beta$ and Ti Ly$_\beta$ lines.
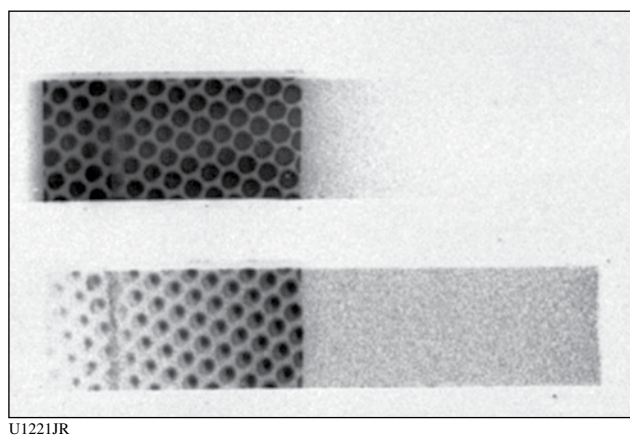

U1221JR

Figure 124.178
Image taken from one of the DDMMI spectrometers for shot 56568. Time goes from top to bottom for these images and the spectrum goes from lower to higher energy, right to left on each strip. The individual circles on these strips represent capsule images at a given photon energy and time. The lines that are just visible in the top strip are the He$_\alpha$ and Ly$_\alpha$ lines of Ti.
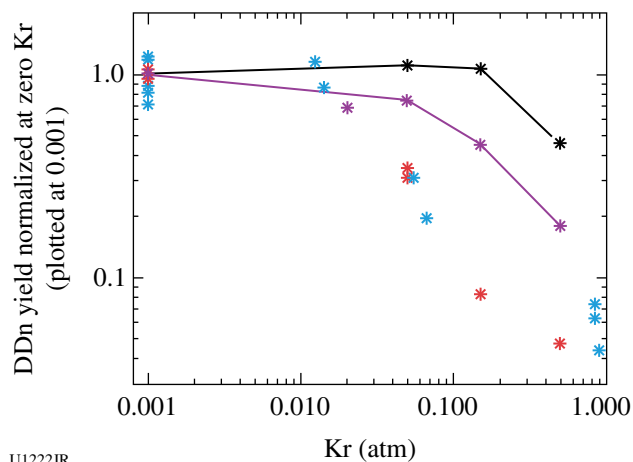

U1222JR

Figure 124.179
Comparison of normalized yields for glass and plastic capsules to simulations. The blue stars are data from glass-capsule implosions, while the red stars are data from the plastic-capsule shots. The purple curve represents calculations that include mix, while the black curve represents calculations without mix. The normalized yield levels for each set of capsules are 1.25×10^{11} for glass and 3.06×10^{11} for plastic, while the normalized simulation levels are 7.43×10^{11} for no mix and 2.85×10^{11} with mix.

DTRat: In addition to alphas and neutrons, the DT fusion reaction produces γ rays from the intermediate ^{5}He nucleus with a small branching ratio (BR) of several 10^{-5} γ/n. The excited ^{5}He can decay to the ground state, emitting a 16.75-MeV (width ~0.5 MeV) γ ray or to the broad first excited state emitting an ~13-MeV (width ~4 MeV) γ ray. Knowledge of the BR between these two states is important to making absolutely calibrated measurements of the overall γ-ray spectrum on the NIF.

An energy-thresholding experiment was carried out for DT ICF implosions on OMEGA using a gas Cherenkov detector. After background subtraction, the fusion γ-ray Cherenkov peak was integrated for four different threshold energies (6.3, 8, 12, and 14 MeV). These integrated signals were then normalized to a specific threshold energy (for example, 12 MeV) and compared to the expected signal trends assuming a single γ-ray line at 16.75 MeV—assuming the two lines at 16.75 MeV and 13 MeV have nearly equal yield contributions (i.e., the "Hale" spectrum). Expected signal trends were calculated using the ACCEPT and Geant4 codes (Fig. 124.180).

In all of the intensity ratio graphs, a clear grouping of the experimental data around the theoretical values of the Hale spectra (double peak) was evident. This indicates that the DT reaction spectra are more like the Hale spectra and its mirror reaction D^{3}He than the previously assumed single-peak spectra. This study does not decisively conclude that the spectra are exactly like the Hale spectra but it confirms that there is a second peak in the spectra that has not been previously considered. This study is significant in that this is the first experimental evidence that clearly points to a double-peak spectra for D–T fusion in an ICF experiment. The refining of the exact spectra will be the subject of further studies.
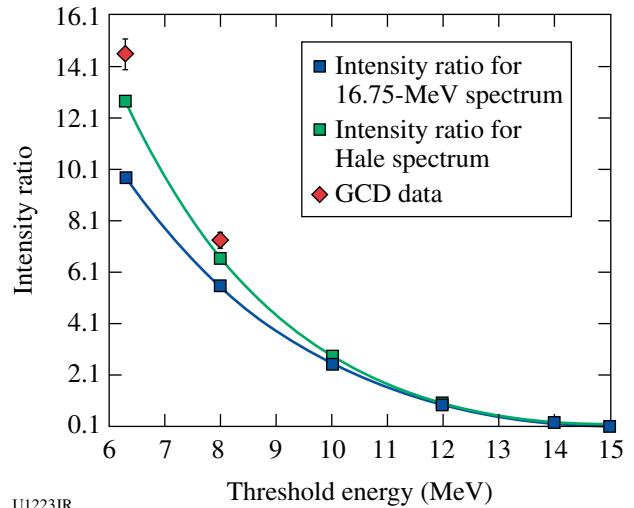
Figure 124.180
Ratio of GCD intensities as a function of threshold energy (MeV) normalized to 12-MeV threshold intensity ratio compared to Geant4 simulations. Red diamonds are experimental data. The green curve is obtained by folding the double-peak spectra[54] with a detector response of the GCD. The blue curve is assumed from a 16.75-MeV single-peak spectrum.

The DTRat campaign also performed experiments to examine the reduction of D–D yield attributable to the presence of ^{3}He. These experiments not only measured the D^{3}He gamma signals but also observed D_2 gammas for the first time. This measurement provides new information to understand the nuclear reactions in an ICF capsule implosion.

OMEGA EP Ions: The LANL target-heating Verdi laser (THVL) was commissioned on OMEGA EP and was used to heat chemical-vapor-deposition (CVD) diamond hemispheres to greater than 1000 °C with the goal of producing nearly pure,
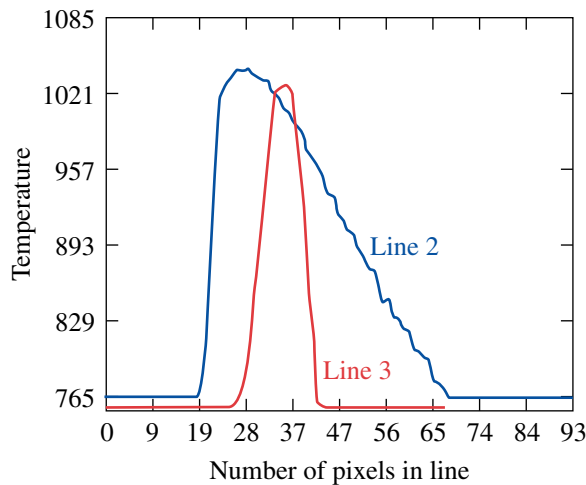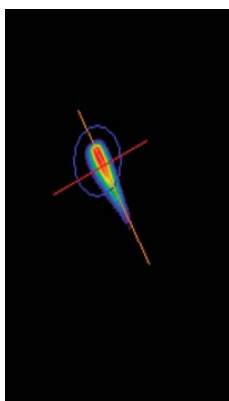

Figure 124.181
Temperature profile of a 500-μm-diam carbon rod heated at the tip by the THVL.

laser-accelerated carbon ion beams. Figure 124.181 shows a 500-μm-diam stand-in alignment target heated by the THVL to over 1000 °C as viewed through the system's pyrometer (left) and the software showing the lineout temperatures (right). Figure 124.182 shows similar data from the pyrometer, this time overlaid on a VisRAD representation of our CVD diamond Hemi target assembly for producing focused ions, showing the hemi heated to over 1000 °C in the center of the assembly.
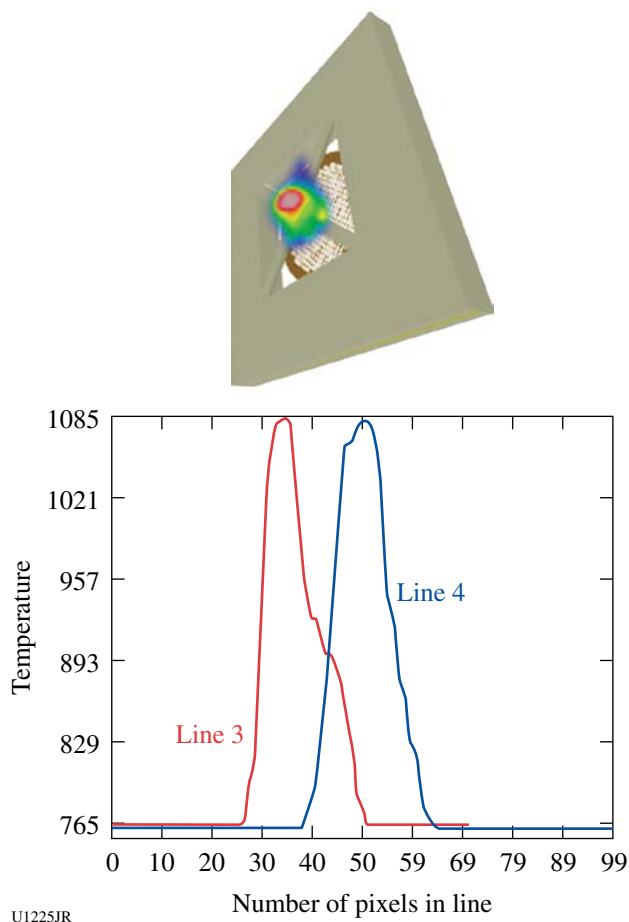

Figure 124.182
Temperature profile of a heated target overlaid with a VisRad image of target.

These heated targets were then shot using the short-pulse OMEGA EP Laser System with a 10-ps pulse at nearly a kilojoule, producing focused ion beams. The accelerated ions were diagnosed with the LANL-TPIE and LLNL-PFPII diagnostics. TPIE included a new cover plate that demonstrated an improved signal-to-noise ratio on the CR-39 solid-state nuclear track detector (SSNTD), and a LiF plate was added to the film-pack configuration to serve as a nuclear activation diagnostic of the carbon ion beam.
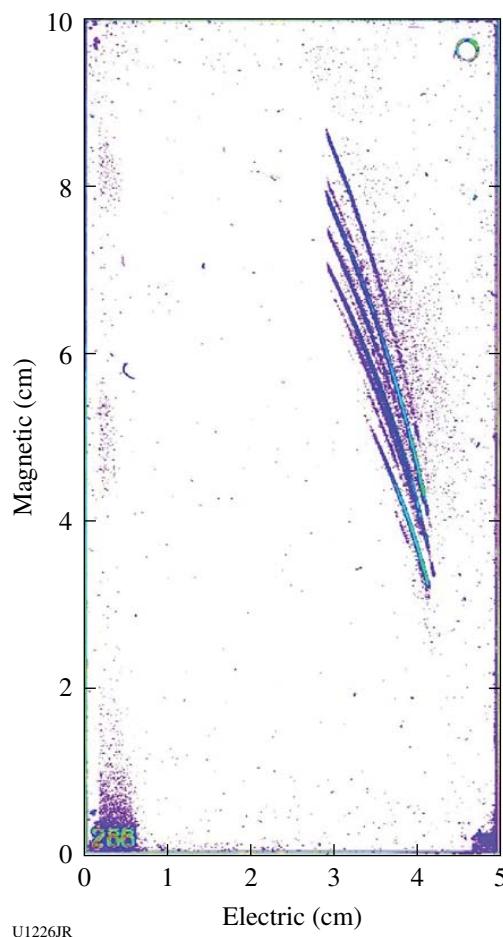

Figure 124.183
CR39 spectra from TPIE. The cutoff energies are for C5+ ~33 MeV (same as for C6+), C4+ ~28 MeV, and C3+ ~14 MeV.

TPIE recorded carbon and oxygen ions and an absence of protons on the SSNTD from the heated targets (Fig. 124.183). Energies of up to 2.75 MeV/nucleon for carbon were observed in large numbers, leading to preliminary conversion efficiencies of a few percent of laser energy into ion energy for each carbon species (depending on assumptions made about the beam size versus the solid angle of TPIE). This means that if all the carbon species could be focused to a 30-μm volume, energy densities of the order of 10^{14} J/m^2 could be achievable.

High-Energy X-Ray Generation (HEX): The high-energy x-ray campaign at LANL has shifted from x-ray production to application of high-energy x rays in phase-contrast imaging. The intent is to generate x rays of sufficient energy that the x-ray absorption is minimal through a Au-walled hohlraum. Given the correct geometric constraints, an interference pattern will be produced in the region of strong phase (or density) gradients. The relationship used to determine the optimal x-ray source to

target distance is $z = (2\lambda u^2)^{-1}$, where z is the propagation distance, λ is the x-ray wavelength, and u is the spatial frequency defined as the inverse of the x-ray source size, in this context. For example, using an x-ray energy of 17.48 keV and an x-ray source size, defined as wire diameter, of 5 μm, the optimal distance from source to target is 17.6 cm.

Experiments this year used K_α x-ray emission from Ag (22-keV) and Cu (8-keV) microfoils to investigate shocks produced in CH targets. As shown in Fig. 124.184, the backlighter beam drove a microfoil ($100 \times 100 \times 5$ μm) from the side using a 20-ps pulse at 1 kJ, and the edge was used to backlight the CH target driven by two 2-ns UV pulses with a total energy of 2 kJ.
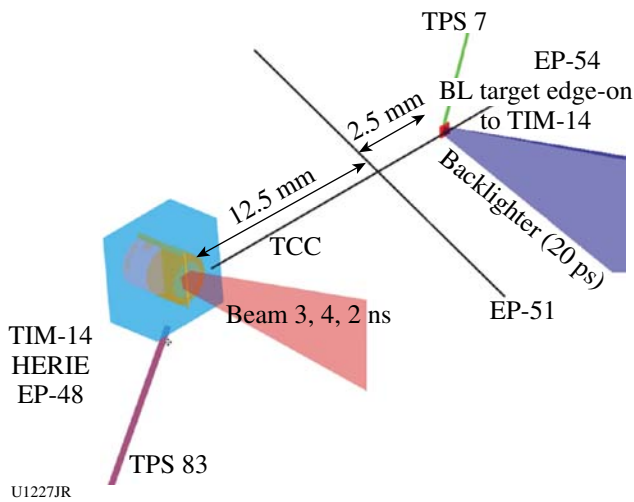

Figure 124.184
Configuration for HEX experiments on OMEGA EP. The primary diagnostic is the HERIE using image plates as the detector. A number of spectrometers were also employed including the TCS, DCS, ZVH, and DCHOPG.

Predicted shock behavior is shown in Fig. 124.185. Data were taken at 4, 6, and 8 ns. Image analysis is still ongoing. Figure 124.186 shows static data taken from gold grids illuminated by Cu emission on the left and Ag emission on the right. Both show high resolution and sufficient signal-to-noise ratio for the intended applications.

FY10 CEA Experiments on the Omega Facility

CEA-led teams conducted 62 shots on OMEGA during FY10. The experiments included ablator preheat characterization, Rayleigh–Taylor (RT) growth measurements, and rugby hohlraum characterization.

Ablator Preheat: Preheat and shock-breakout measurements were obtained in graded dopant targets on OMEGA on 14 June
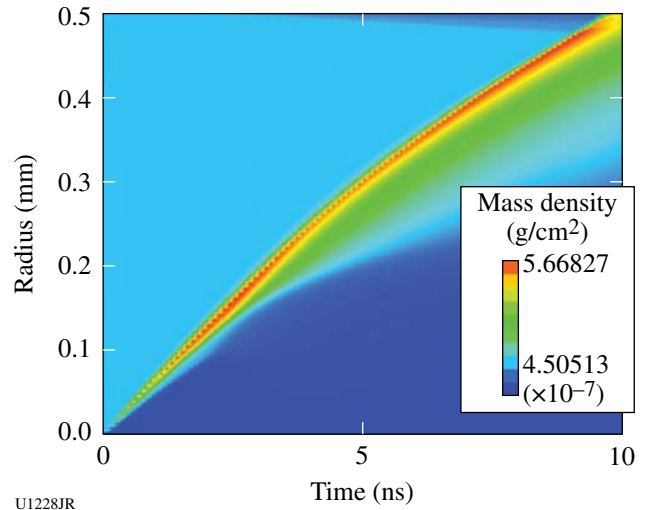

Figure 124.185
One-dimensional hydrodynamics calculation using HELIOS-CR predicting the shock structure as a function of time and position for a CH target driven by 2-kJ, 2-ns UV drive on OMEGA EP.
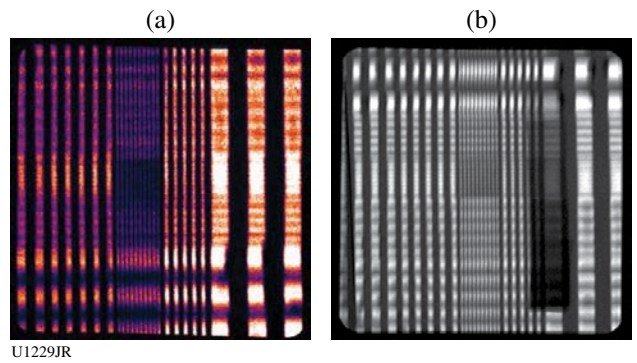

Figure 124.186
Static gold grids illuminated by Cu (left) and Ag (right) backlighters showing sufficient resolution and signal-to-noise ratio.

2010. CEA may use the graded dopant scheme for future ICF capsules. It consists of using several layers of Ge-doped plastic to protect the fuel from hard x rays; moreover, it must ensure hydrodynamic stability at the pusher/fuel interface. To this extent, the Ge-doped layers must be preheated by the M-band radiation so that the density profile across the shell will become nearly constant.

Two-dimensional transpositions of this design were shot on OMEGA. Preheat and shock breakouts were monitored using the ASBO diagnostic (Fig. 124.187). Extensive hohlraum energetics data were obtained using DMX and Dante broadband spectrometers. Detailed M-band radiation was measured using CEA μDMX and Henway spectrometers.

Rayleigh–Taylor Instability Experiments: We measured RT growths in indirectly driven rippled samples as function of Ge on OMEGA on 15 June 2010. These shots were intended to constrain physical models used in CEA hydrodynamic simulations.

These experiments will also provide us with a scaling between the length of RT spikes and corresponding optical-depth variation measured on face-on radiography images. Differentiated behaviors as a function of dopant fraction were found, and as predicted, the highest growth factors were measured on highly doped samples (Fig. 124.188).

Additional data on face-on x-ray source characterization were obtained. For this purpose, a single Sc foil was shot in
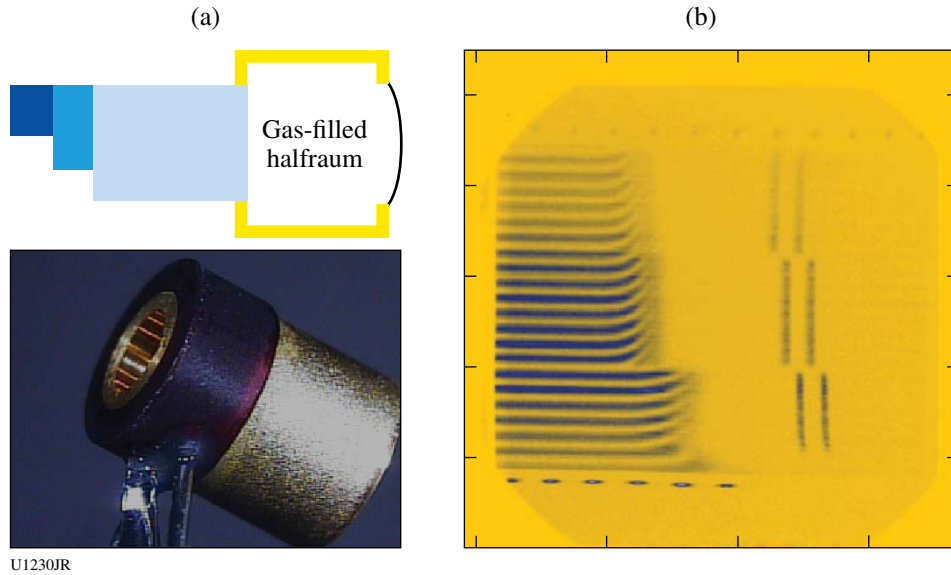

Figure 124.187
(a) Schematic and real views of a target assembly. Samples were planar and comprised different steps of plastic doped with different atomic proportions of Ge. Steps were coated with Ta to be reflective. (b) Example of a VISAR image: fringe movement is due to preheat until the Ta coating stays reflective. Short flashes seen later in time are due to shock breakout.
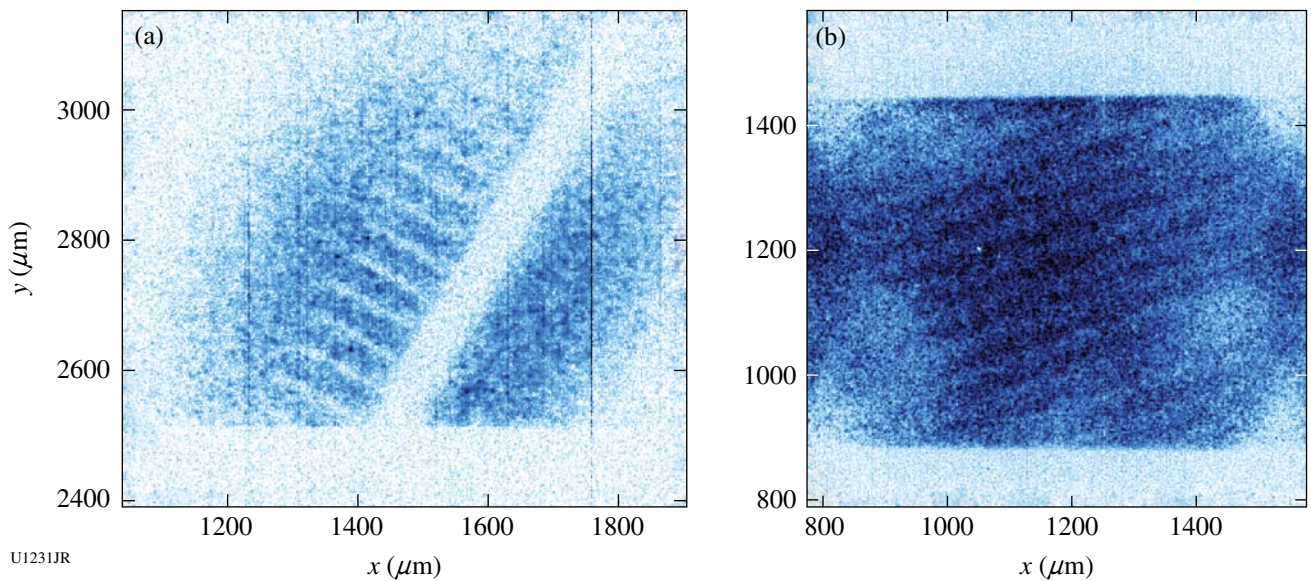

Figure 124.188
(a) Side-on and (b) face-on radiography of a 20% atomic Ge plastic foil. Nonlinear RT growth spikes seen in (a) are approximately 200 μm long.

order to calibrate the radiography source routinely used in RT growth and in an implosion experiment. The influence of a gas-filled hohlraum plasma on the radiography signal was also studied using a Sc x-ray source placed behind a gas-filled hohlraum with no sample mounted on it (Fig. 124.189).

Implosions in Rugby Hohlraums: In the last few years, CEA has conducted extensive experimental investigations of the rugby hohlraum concept on OMEGA. Rugby hohlraums are part of an effort toward advanced, high-efficiency hohlraum designs, which could provide increased margin for ignition on LMJ and NIF and could also be suited for use in an IFE context because of their higher gains.

In 2009, in collaboration with LLNL (H. S. Park, H. F. Robey, and P. A. Amendt) and MIT (C. K. Li, F. H. Séguin, and R. D. Petrasso), a significant enhancement of x-ray drive in rugby hohlraums with respect to classical cylindrical hohlraums in a direct comparison (Fig. 124.190) was demonstrated. The improved capsule design led to the highest yields for indirect drive with noncryogenic deuterium fuel at the time, enabling researchers to use many nuclear diagnostics (neutron imaging, NTD, Fig. 124.191) for the first time in this configuration. These results were published in Physical Review Letters and Science.[55,56] In 2010, the symmetry of implosion (Fig. 124.192) was successfully tuned with a calculated cone-balancing scheme based on the detailed simulations of a 2009

OMEGA experiment, therefore confirming the understanding of rugby hohlraum performance. The work this year was also extended to gas-filled rugby hohlraums with shaped pulses. Measurements have shown a relatively low level of backscatter (~5%), which could be further reduced by the use of polarization smoothing, and performance in good agreement with simulations. Direct comparison of gas-filled rugby and cylindrical hohlraums is planned on OMEGA at the end of 2010.
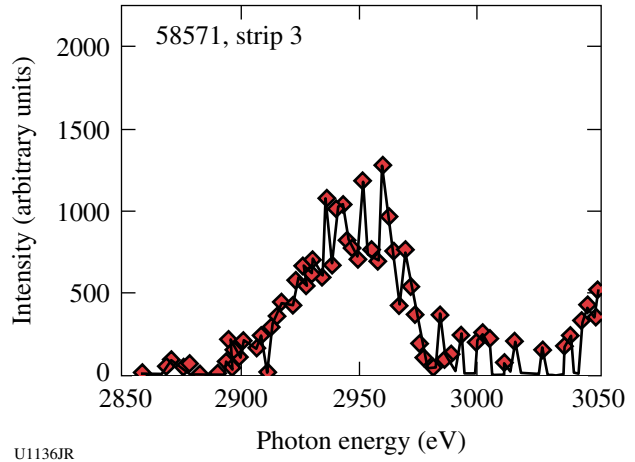

Figure 124.190
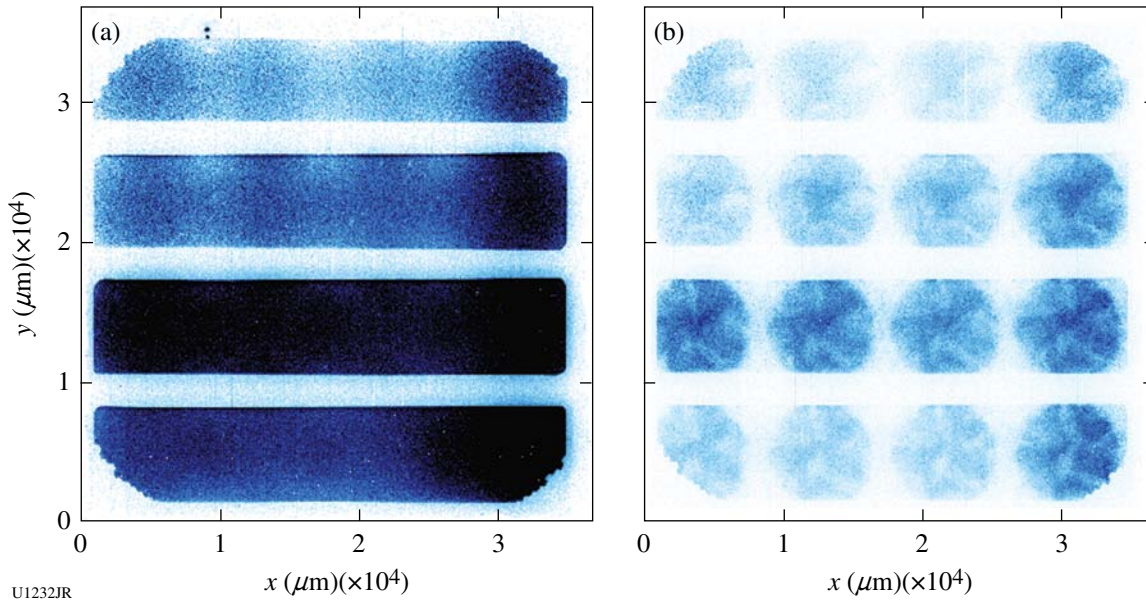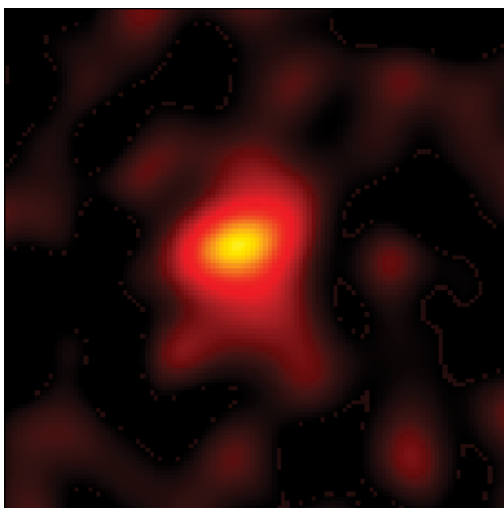Evidence of 18% x-ray–drive enhancement with rugby hohlraums.

Figure 124.189
XRFC images given by (a) a single Sc x-ray source and (b) a Sc source placed behind a gas-filled hohlraum with no sample mounted on it.
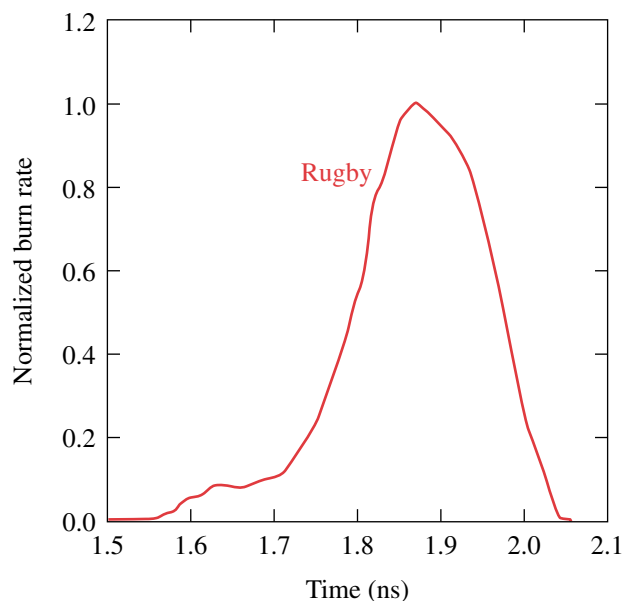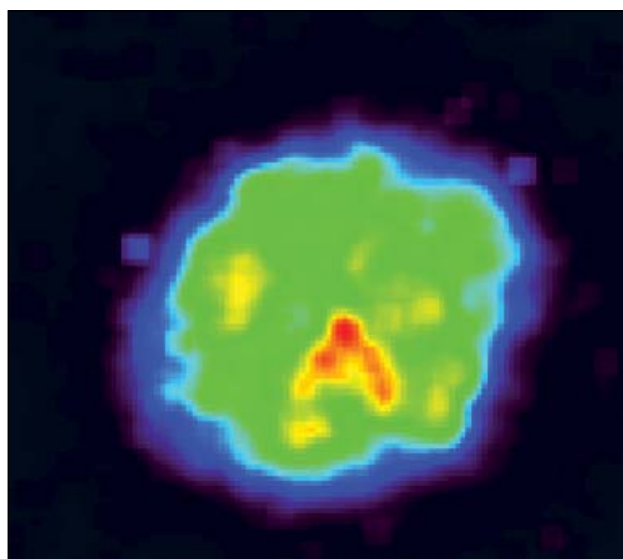
U1234JR

Figure 124.191
Neutron image and reaction history of deuterium-filled indirectly driven capsules.

U1235JR

Figure 124.192
Symmetric implosion obtained with calculated cone balance to compensate evaluated backscatter effects.

FY10 AWE OMEGA Experimental Programs

In FY10, AWE led three shot days on the OMEGA laser. This work encompassed an investigation of asymmetrically driven hohlraums (two days) and a Laue x-ray diffraction study of the dynamics of shocked tantalum crystals (one day).

Asymmetrically Driven Hohlraums: Work by AWE has continued to study the asymmetrically driven implosion of thin glass shells and aerogel-foam witness balls in hohlraum targets, as a sensitive test of radiation hydrodynamic modeling. Asymmetry of radiation drive is achieved by asymmetry of laser-beam energy and timing, by asymmetry of capsule position, and by introducing an annular restriction of diameter (baffle) within the hohlraum.

A 1.6-mm-diam, 2.7-mm-long hohlraum is heated by up to 30 OMEGA beams. X-ray backlighting of a thin-wall glass capsule (600-μm diameter, 3.5-μm wall thickness, 30-μm CH ablator) or silica aerogel sphere (600-μm diameter, 300-mg cm^{-3} density) provides the primary diagnostic of the angular distribution of radiation drive near the center of the hohlraum. The hydrodynamics are diagnosed by x-ray backlighting using an area-backlighting source together with a 16-image pinhole camera and a four-strip gated microchannel-plate (MCP) detector, or by point-projection x-ray backlighting together with a single-strip MCP detector. In the case of point backlighting (new to this campaign in FY10), just one single image is recorded but this is of higher spatial resolution (lower statistical "shot noise") than in the case of multiple images, and this technique has the further advantage of potential sensitivity to refraction (phase-contrast enhancement) at the steep density gradients encountered at ablation and shock fronts within the capsule or foam witness ball.

In previous work[57] using hohlraums with end-to-end asymmetry of laser drive, a polar jet was recorded and was a particularly sensitive diagnostic of the angular distribution of early-time radiation drive. Many features of the hydrodynamics were successfully reproduced by hydrocode modeling, but modeling and experiment differed in one important respect: simulation showed a small "bump" of material at the most strongly driven pole of thin-shell capsules that was not observed in the experiment. Work during FY10 further investigated this feature of the hydrodynamics. The position of the capsule in the hohlraum was offset from hohlraum center (Fig. 124.193) to provide a further modulation of the angular distribution of the early-time drive at the hot pole. The polar bump was observed and demonstrated to be a genuine feature of the hydrodynamics (and not a near-axis artifact arising in the modeling). These
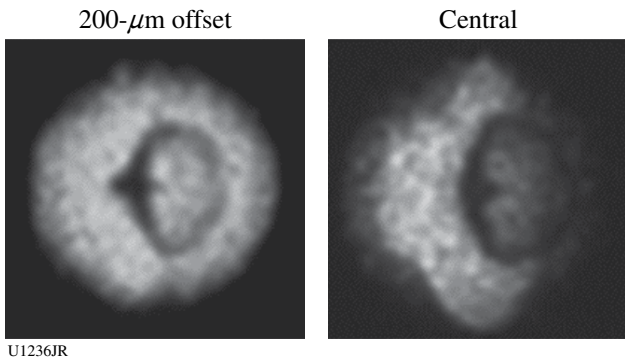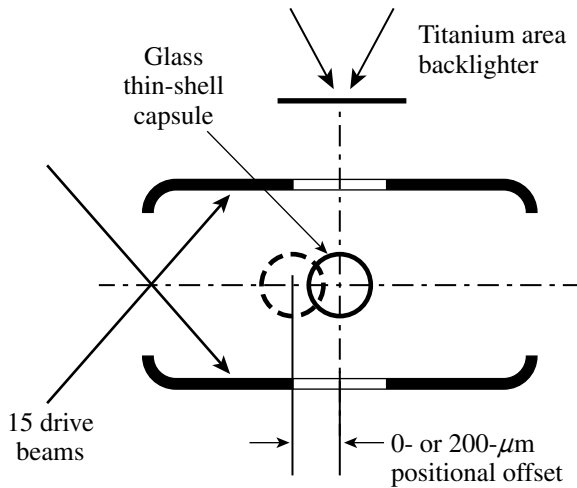
experimental data from OMEGA have been used to improve AWE's hydrocode simulations, and detailed attention to pre-heat, near-axis resolution, and radiation-transport modeling has resulted in very much closer agreement with the experiment (Fig. 124.194).
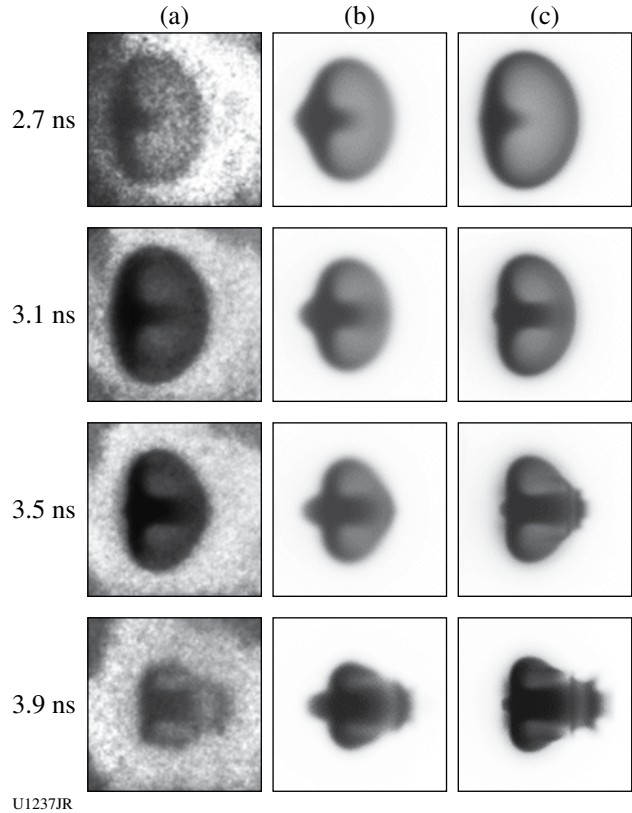

Figure 124.194
Sequence of experimental radiographs (a) of implosion of an asymmetrically driven thin-shell glass capsule compared with simulation before (b) and after (c) improvements to the modeling arising from experiments at OMEGA.

Figure 124.193
Experiment to investigate sensitivity of the polar "bump" to capsule position in an asymmetrically driven hohlraum. The hohlraum is aligned on the P6–P7 axis of the OMEGA target chamber and is driven by 15 beams of the OMEGA laser from one side only. A small displacement of position of the thin-wall glass capsule introduces a further modulation of the angular distribution of asymmetric drive, evident in the radiographs.

The use of internal, washer-shaped baffles (Fig. 124.195) in hohlraum targets provides a means of shielding an experimental assembly at hohlraum center from a direct view of the individual laser "hot spots" at the hohlraum wall (although at the expense of significant loss of symmetry of angular distribution of drive). X-ray backlighting measurements of capsule implosions in such targets have also been made during FY10 to provide a further benchmark test of hohlraum modeling. Figure 124.195 shows a comparison of 10-μm-resolution, point-projection–backlit images of capsule implosion in regular and baffled hohlraums. The improvement of spatial resolution in these images, in comparison with area-backlit images, is readily apparent (compare Figs. 124.193 and 124.195), as is the

Titanium point
backlighter

15 drive
beams

No baffle
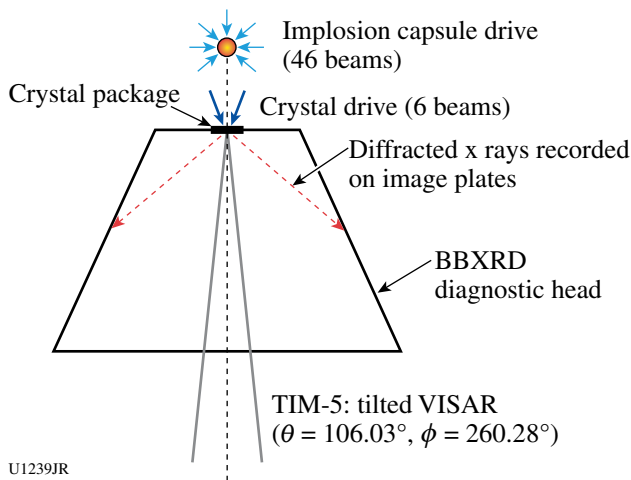
900-μm-diam baffle
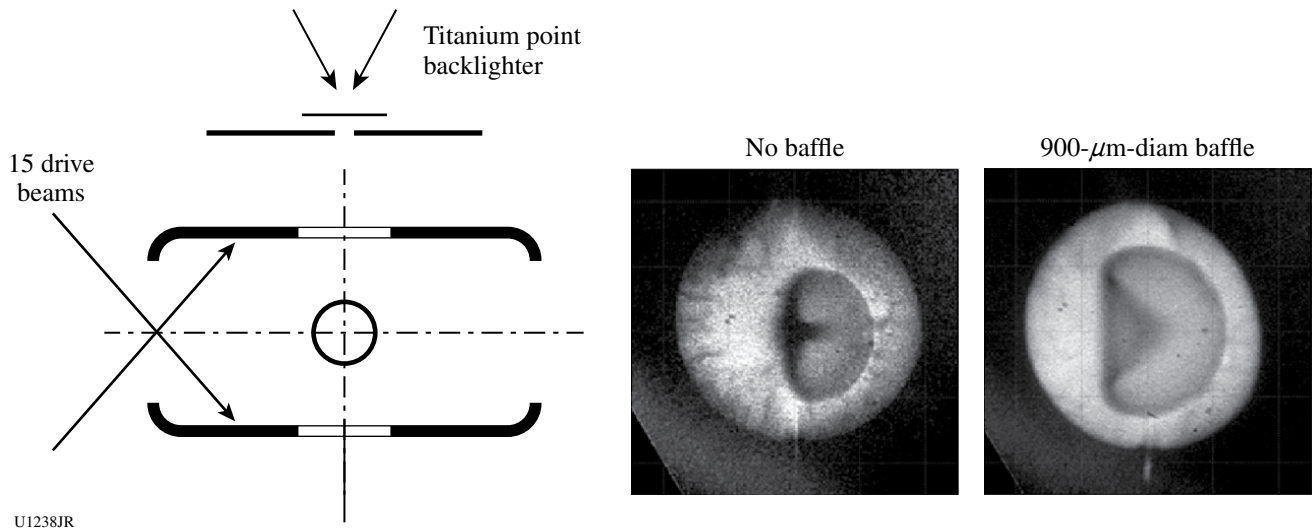
U1238JR

Figure 124.195
Point-backlit images of thin-shell implosions in regular and baffled hohlraums.

possible refraction-enhanced gradient of image intensity near the ablation front at the cold pole of the capsule.

Laue X-Ray Diffraction: The objective of this one-day campaign was to demonstrate the use of broadband x-ray ("white light") Laue diffraction to probe the lattice dynamics of single-crystal tantalum under shock-loaded conditions, in conjunction with the newly commissioned LLNL BBXRD diagnostic (Fig. 124.196). This campaign complements work by

LLE and LLNL, which used the same developmental diffraction technique to investigate the lattice dynamics of shocked copper and silicon samples.

The white-light Laue technique produces a characteristic diffraction pattern (Fig. 124.197), in which each spot can be

Implosion capsule drive
(46 beams)

Crystal package   Crystal drive (6 beams)

Diffracted x rays recorded
on image plates

BBXRD
diagnostic head

TIM-5: tilted VISAR
($\theta = 106.03°$, $\phi = 260.28°$)

U1239JR

Figure 124.196
Sketch of experimental setup showing an implosion capsule backlighter, a Ta crystal package mounted on BBXRD diagnostic, image plate detectors to record the diffraction pattern, and a VISAR diagnostic used to infer the state of the driven sample.

(0 4 2) 17.7 keV

(−2 3 1) 24 keV

(−2 4 2) 21 keV

(−3 3 2) 19.5 keV

(−4 2 2) 21 keV

(−3 2 1) 24 keV

mm

mm
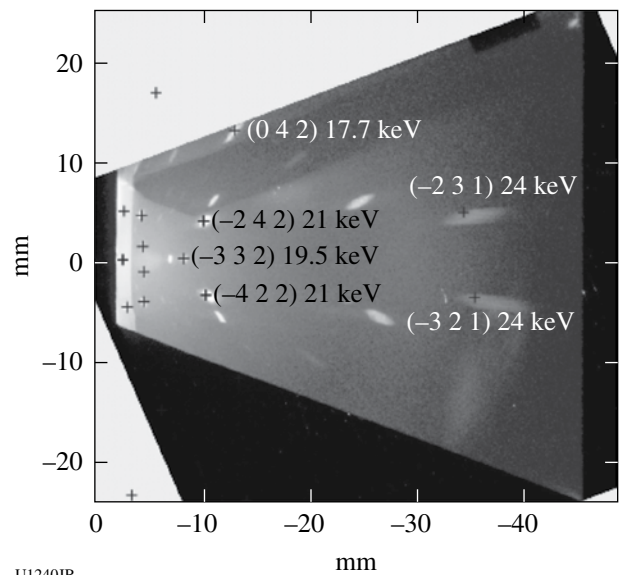
U1240JR

Figure 124.197
Diffraction pattern obtained from 5-μm-thick, single-crystal (100) Ta using an implosion capsule backlighter and LLNL broadband x-ray diffraction (BBXRD) diagnostic. Each crystallographic plane (*hkl*) generates a characteristic diffraction spot, some of which are labeled in the figure.

attributed to a crystallographic plane in the sample lattice. In principle, this pattern offers unique insight into changes in lattice structure generated under loaded conditions (be it ramp or shock loading), such as the formation and growth of defects and 1-D-to-3-D relaxation processes, by examining and interpreting the location and structure of the characteristic diffraction spots.

An implosion capsule backlighter (980-μm outer diameter with a 10-μm-thick CH wall) driven by 46 OMEGA beams (each beam contained 500 J in a 1-ns square pulse and was used with SG4 DPP) was employed to generate a smooth, broadband spectrum of x rays to produce the white-light diffraction pattern (Fig. 124.198). Such backlighters also have the advantage of a short temporal duration of emission, useful for probing lattice dynamics on an ~100-ps time scale.
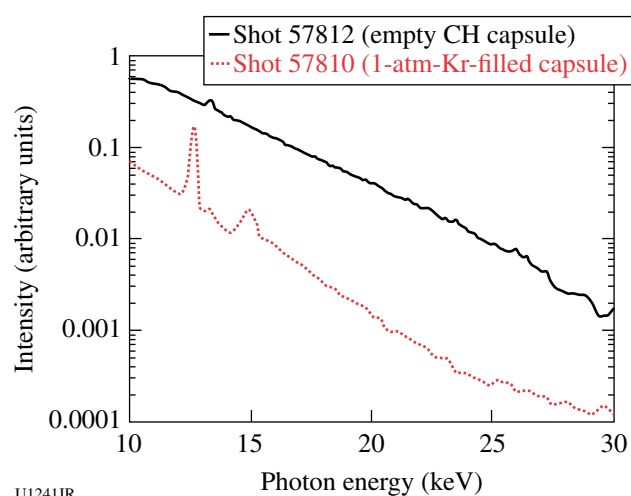
Figure 124.198
Time-integrated spectrum from an implosion capsule backlighter recorded using the double-crystal spectrometer (DCS).

Diffraction data were successfully recorded from both static and driven tantalum samples. Figure 124.197 illustrates the diffraction pattern from a static (i.e., undriven) Ta sample.

Several improvements will be employed in future campaigns. First, one of the most-challenging aspects of this experiment was the production of high-quality crystal samples that were flat and nominally free of crystallographic defects. Modifications will be made to the crystal package design, and improvements will be made to the assembly process in order to address this issue. Second, VISAR measurements indicated that the spatial uniformity of the drive on the crystal package should be improved in order to simplify the interpretation of the data. Changes in beam configuration are being examined to address this point.

REFERENCES

1. S. H. Glenzer *et al.*, Phys. Rev. Lett. **90**, 175002 (2003).

2. H. J. Lee, P. Neumayer, J. Castor, T. Döppner, R. W. Falcone, C. Fortmann, B. A. Hammel, A. L. Kritcher, O. L. Landen, R. W. Lee, D. D. Meyerhofer, D. H. Munro, R. Redmer, S. P. Regan, S. Weber, and S. H. Glenzer, Phys. Rev. Lett. **102**, 115001 (2009).

3. S. H. Glenzer *et al.*, Phys. Rev. Lett. **98**, 065002 (2007); A. L. Kritcher *et al.*, Science **322**, 69 (2008); A. García Saiz *et al.*, Nat. Phys. **4**, 940 (2008).

4. S. H. Glenzer *et al.*, Phys. Plasmas **10**, 2433 (2003); O. L. Landen *et al.*, J. Quant. Spectrosc. Radiat. Transf. **71**, 465 (2001); H. Sawada, S. P. Regan, D. D. Meyerhofer, I. V. Igumenshchev, V. N. Goncharov, T. R. Boehly, R. Epstein, T. C. Sangster, V. A. Smalyuk, B. Yaakobi, G. Gregori, S. H. Glenzer, and O. L. Landen, Phys. Plasmas **14**, 122703 (2007).

5. L. M. Barker and R. E. Hollenbach, J. Appl. Phys. **43**, 4669 (1972).

6. G. W. Collins *et al.*, Science **281**, 1178 (1998); P. M. Celliers, D. K. Bradley, G. W. Collins, D. G. Hicks, T. R. Boehly, and W. J. Armstrong, Rev. Sci. Instrum. **75**, 4916 (2004); P. M. Celliers *et al.*, J. Appl. Phys. **98**, 113529 (2005); D. G. Hicks, T. R. Boehly, P. M. Celliers, J. H. Eggert, S. J. Moon, D. D. Meyerhofer, and G. W. Collins, Phys. Rev. B **79**, 014112 (2009); M. D. Knudson and M. P. Desjarlais, Phys. Rev. Lett. **103**, 225501 (2009).

7. J. Eggert, S. Brygoo, P. Loubeyre, R. S. McWilliams, P. M. Celliers, D. G. Hicks, T. R. Boehly, R. Jeanloz, and G. W. Collins, Phys. Rev. Lett. **100**, 124503 (2008).

8. Ya. B. Zel'dovich and Yu. P. Raĭzer, in *Physics of Shock Waves and High-Temperature Hydrodynamic Phenomena*, edited by W. D. Hayes and R. F. Probstein (Academic Press, New York, 1966), Vol. I, Chap. II, pp. 107–175.

9. R. P. Drake, *High-Energy-Density Physics: Fundamentals, Inertial Fusion, and Experimental Astrophysics*, Shock Wave and High Pressure Phenomena (Springer, Berlin, 2006).

10. J. J. Fortney *et al.*, Phys. Plasmas **16**, 041003 (2009).

11. B. A. Remington, R. P. Drake, and D. D. Ryutov, Rev. Mod. Phys. **78**, 755 (2006).

12. T. Guillot, Science **286**, 72 (1999).

13. W. J. Nellis, M. Ross, and N. C. Holmes, Science **269**, 1249 (1995).

14. W. J. Nellis, S. T. Weir, and A. C. Mitchell, Science **273**, 936 (1996).

15. N. Nettelmann *et al.*, Astrophys. J. **683**, 1217 (20085).

16. B. Militzer *et al.*, Astrophys. J. **688**, L45 (2008).

17. I. de Pater and J. J. Lissauer, *Planetary Sciences*, 5th ed. (Cambridge University Press, Cambridge, England, 2007), p. 544.

18. E. C. Stone and E. D. Miner, Science **246**, 1417 (1417).

19. S. Stanley and J. Bloxham, Nature **428**, 151 (2004).

20. P. Hartigan *et al.*, Astrophys. J. **705**, 1073 (2009).

21. J. M. Foster *et al.*, Phys. Plasmas **17**, 112704 (2010).

22. P. M. Celliers, P. Loubeyre, J. H. Eggert, S. Brygoo, R. S. McWilliams, D. G. Hicks, T. R. Boehly, R. Jeanloz, and G. W. Collins, Phys. Rev. Lett. **104**, 184503 (2010).

23. W. Lorenzen, B. Holst, and R. Redmer, Phys. Rev. Lett. **102**, 115701 (2009).

24. C. K. Li, F. H. Séguin, J. A. Frenje, J. R. Rygg, R. D. Petrasso, R. P. J. Town, P. A. Amendt, S. P. Hatchett, O. L. Landen, A. J. Mackinnon, P. K. Patel, V. Smalyuk, J. P. Knauer, T. C. Sangster, and C. Stoeckl, Rev. Sci. Instrum. **77**, 10E725 (2006).

25. T. R. Boehly, D. L. Brown, R. S. Craxton, R. L. Keck, J. P. Knauer, J. H. Kelly, T. J. Kessler, S. A. Kumpan, S. J. Loucks, S. A. Letzring, F. J. Marshall, R. L. McCrory, S. F. B. Morse, W. Seka, J. M. Soures, and C. P. Verdon, Opt. Commun. **133**, 495 (1997).

26. J. R. Rygg, F. H. Séguin, C. K. Li, J. A. Frenje, M. J.-E. Manuel, R. D. Petrasso, R. Betti, J. A. Delettrez, O. V. Gotchev, J. P. Knauer, D. D. Meyerhofer, F. J. Marshall, C. Stoeckl, and W. Theobald, Science **319**, 1223 (2008).

27. C. K. Li, F. H. Séguin, J. A. Frenje, M. Rosenberg, R. D. Petrasso, P. A. Amendt, J. A. Koch, O. L. Landen, H. S. Park, H. F. Robey, R. P. J. Town, A. Casner, F. Philippe, R. Betti, J. P. Knauer, D. D. Meyerhofer, C. A. Back, J. D. Kilkenny, and A. Nikroo, Science **327**, 1231 (2010).

28. C. K. Li, F. H. Séguin, J. A. Frenje, J. R. Rygg, R. D. Petrasso, R. P. J. Town, P. A. Amendt, S. P. Hatchett, O. L. Landen, A. J. Mackinnon, P. K. Patel, V. A. Smalyuk, T. C. Sangster, and J. P. Knauer, Phys. Rev. Lett. **97**, 135003 (2006).

29. C. K. Li, F. H. Séguin, J. A. Frenje, J. R. Rygg, R. D. Petrasso, R. P. J. Town, P. A. Amendt, S. P. Hatchett, O. L. Landen, A. J. Mackinnon, P. K. Patel, M. Tabak, J. P. Knauer, T. C. Sangster, and V. A. Smalyuk, Phys. Rev. Lett. **99**, 015001 (2007).

30. C. K. Li, F. H. Séguin, J. A. Frenje, J. R. Rygg, R. D. Petrasso, R. P. J. Town, O. L. Landen, J. P. Knauer, and V. A. Smalyuk, Phys. Rev. Lett. **99**, 055001 (2007).

31. C. K. Li, F. H. Séguin, J. R. Rygg, J. A. Frenje, M. Manuel, R. D. Petrasso, R. Betti, J. Delettrez, J. P. Knauer, F. Marshall, D. D. Meyerhofer, D. Shvarts, V. A. Smalyuk, C. Stoeckl, O. L. Landen, R. P. J. Town, C. A. Back, and J. D. Kilkenny, Phys. Rev. Lett. **100**, 225001 (2008).

32. C. K. Li, F. H. Séguin, J. A. Frenje, R. D. Petrasso, P. A. Amendt, R. P. J. Town, O. L. Landen, J. R. Rygg, R. Betti, J. P. Knauer, D. D. Meyerhofer, J. M. Soures, C. A. Back, J. D. Kilkenny, and A. Nikroo, Phys. Rev. Lett. **102**, 205001 (2009).

33. R. D. Petrasso, C. K. Li, F. H. Séguin, J. R. Rygg, J. A. Frenje, R. Betti, J. P. Knauer, D. D. Meyerhofer, P. A. Amendt, D. H. Froula, O. L. Landen, P. K. Patel, J. S. Ross, and R. P. J. Town, Phys. Rev. Lett. **103**, 085001 (2009).

34. O. V. Gotchev, P. Y. Chang, J. P. Knauer, D. D. Meyerhofer, O. Polomarov, J. Frenje, C. K. Li, M. J.-E. Manuel, R. D. Petrasso, J. R. Rygg, F. H. Séguin, and R. Betti, Phys. Rev. Lett. **103**, 215004 (2009).

35. G. Li, R. Yan, C. Ren, T.-L. Wang, J. Tonge, and W. B. Mori, Phys. Rev. Lett. **100**, 125002 (2008).

36. H. Chen, S. C. Wilks, D. D. Meyerhofer, J. Bonlie, C. D. Chen, S. N. Chen, C. Courtois, L. Elberson, G. Gregori, W. Kruer, O. Landoas, J. Mithen, J. Myatt, C. D. Murphy, P. Nilson, D. Price, M. Schneider, R. Shepherd, C. Stoeckl, M. Tabak, R. Tommasini, and P. Beiersdorfer, Phys. Rev. Lett. **105**, 015003 (2010).

37. S. H. Glenzer *et al.*, Phys. Rev. Lett. **88**, 235002 (2002).

38. University of Washington, Department of Physics, FEFF Project, 2004, http://leonardo.phys.washington.edu/feff/ (24 June 2004).

39. W. Theobald, A. A. Solodov, C. Stoeckl, K. S. Anderson, R. Betti, T. R. Boehly, R. S. Craxton, J. A. Delettrez, C. Dorrer, J. A. Frenje, V. Yu. Glebov, H. Habara, K. A. Tanaka, J. P. Knauer, R. Lauck, F. J. Marshall, K. L. Marshall, D. D. Meyerhofer, P. M. Nilson, P. K. Patel, T. C. Sangster, W. Seka, N. Sinenian, T. Ma, F. N. Beg, and R. B. Stephens, Bull. Am. Phys. Soc. **55**, 291 (2010).

40. J. A. Halbleib *et al.*, IEEE Trans. Nucl. Sci. **39**, 1025 (1992).

41. N. Izumi, C. Hagmann, G. Stone, D. Hey, S. Glenn, A. Conder, A. Teruya, C. Sorce, R. Tommasini, W. Stoeffl, P. Springer, O. L. Landen, H. W. Herrmann, G. A. Kyrala, R. Bahukutumbi, V. Y. Glebov, T. C. Sangster, M. Eckart, A. J. Mackinnon, J. A. Koch, D. K. Bradley, and P. Bell, Rev. Sci. Instrum. **81**, 10E515 (2010).

42. T. Döppner, C. Fortmann, P. F. Davis, A. L. Kritcher, O. L. Landen, H. J. Lee, R. Redmer, S. P. Regan, and S. H. Glenzer, J. Phys., Conf. Ser. **244**, 032044 (2010).

43. H.-S. Park *et al.*, Phys. Rev. Lett. **104**, 135504 (2010); H.-S. Park *et al.*, Phys. Plasmas **17**, 056314 (2010).

44. N. R. Barton, private communication (2010).

45. D. L. Preston, D. L. Tonks, and D. C. Wallace, J. Appl. Phys. **93**, 211 (2003).

46. M. A. Meyers, A. Mishra, and D. J. Benson, Prog. Mater. Sci. **51**, 427 (2006).

47. D. G. Hicks, T. R. Boehly, P. M. Celliers, J. H. Eggert, E. Vianello, D. D. Meyerhofer, and G. W. Collins, Phys. Plasmas **12**, 082702 (2005).

48. O. A. Hurricane, High Energy Density Phys. **4**, 97 (2008).

49. E. C. Harding *et al.*, Phys. Rev. Lett. **103**, 045005 (2009).

50. O. A. Hurricane *et al.*, Phys. Plasmas **16**, 056305 (2009).

51. R. E. Olson *et al.*, Rev. Sci. Instrum. **77**, 10E523 (2006).

52. L. S. Dubrovinsky *et al.*, Phys. Rev. Lett. **84**, 1720 (2000).

53. J. C. Boettger and D. C. Wallace, Phys. Rev. B **55**, 2840 (1997).

54. G. M. Hale and D. C. Dodder, in *Nuclear Cross Sections for Technology*, edited by J. L. Fowler, C. H. Johnson, and C. D. Bowman, Natl. Bur. Stand. (U.S.), Spec. Publ. 594 (U.S. Government Printing Office, Washington, DC, 1980), pp. 650–658.

55. F. Philippe, A. Casner, T. Caillaud, O. Landoas, M. C. Monteil, S. Liberatore, H. S. Park, P. Amendt, H. Robey, C. Sorce, C. K. Li, F. Seguin, M. Rosenberg, R. Petrasso, V. Glebov, and C. Stoeckl, Phys. Rev. Lett. **104**, 035004 (2010).

56. C. K. Li, F. H. Séguin, J. A. Frenje, M. Rosenberg, R. D. Petrasso, P. A. Amendt, J. A. Koch, O. L. Landen, H. S. Park, H. F. Robey, R. P. J. Town, A. Casner, F. Philippe, R. Betti, J. P. Knauer, D. D. Meyerhofer, C. A. Back, J. D. Kilkenny, and A. Nikroo, Science **327**, 1231 (2010).

57. K. Vaughn *et al.*, Phys. Plasmas **17**, 056316 (2010).